Computational modelling of structural, dynamical and electronic properties of multicomponent silicate glasses

Konstantinos Konstantinou

A dissertation submitted for the degree of

Doctor of Philosophy

Department of Physics & Astronomy

University College London

March 2017

Declaration

I, Konstantinos Konstantinou, confirm that the work presented in this thesis is my own. Where information has been derived from other sources, I confirm that this has been indicated in the thesis.

Konstantinos Konstantinou
March 2017

Abstract

Amorphous silica doped with alkali, alkaline-earth and boron ions is an important class of materials used in many technological applications. Computer simulations are able to provide atomic pictures of the glass structures and detailed insight into compositional–atomic structure relationships. In this thesis several glasses of current interest for nuclear waste immobilisation and microelectronics are studied, using classical and *ab initio* methods.

A method to calculate the glass transition temperature in alkali borosilicate glasses, with pre-defined molar composition, was implemented and validated through the comparison with the available experimental data. The addition of alkali and boron oxides to pure SiO_2 glass resulted in a vast decrease in the glass transition temperature. A systematic study of the density, atomic and electronic structure for lithium sodium borosilicate glasses with varying SiO_2 / B_2O_3 ratio and fixed molar composition of the alkali oxides is reported. *Ab initio* molecular dynamics simulations were performed in order to model the local atomic structure of molybdenum in nuclear waste glasses. Analysis of the structural motifs and the environment of the molybdenum atoms provided direct insight into the solubility of Mo in the glass structures. The results significantly extend the understanding of how the chemical nature and molar composition of the glass host affect the bonding in Mo-containing nuclear glasses and demonstrate that tailoring the glass composition to specific heavy metal constituents can facilitate incorporation of heavy metals at high concentrations.

A series of mixed alkali/alkaline-earth silicate glasses was investigated in order to understand the impact of the nature of the cations on the mobility of the alkaline-earth ions within the glass network. The size of the alkaline-earth cation was found to affect the short-range order and the short-time dynamical behaviour. An asymmetrical linear behaviour in the activation energy for diffusion with increasing cation size difference was observed. The electronic properties of excited states in sodium silicate glass were investigated with *ab initio* modelling. The existence of two different configurations for the excited state are predicted, which correspond to two discrete ranges of luminescence energies. The different short-range ordering of Na cations corresponds to a structural precursor responsible for the calculated values of the luminescence energy.

Publications

The work presented in this thesis has led to the following publications:

3. Konstantinos Konstantinou, Dorothy M. Duffy, and Alexander L. Shluger. Structure and luminescence of intrinsic localized states in sodium silicate glasses, Phys. Rev. B **94**, 174202-174208 (2016).

2. Konstantinos Konstantinou, Peter V. Sushko, and Dorothy M. Duffy. Modelling the local atomic structure of molybdenum in nuclear waste glasses with *ab initio* molecular dynamics simulations, Phys. Chem. Chem. Phys. **18**, 26125-26132 (2016).

1. Konstantinos Konstantinou, Peter V. Sushko, and Dorothy M. Duffy. Structure and ionic diffusion of alkaline-earth ions in mixed cation glasses $A_2O{-}2MO{-}4SiO_2$ with molecular dynamics simulations, J. Non-Cryst. Solids **422**, 57-63 (2015).

Acknowledgements

I would like to express a few "thank you" towards several directions.

Dorothy Duffy: She was my first supervisor and I could not ask for a better advisor. She managed, with her way, to make me work efficiently, develop and establish my scientific knowledge related to my research, while she was always available for me to discuss and help. I think that certain people match with certain supervisors and I strongly believe that for my way of thinking Dorothy was a very good fit.

Peter Sushko: He was the person who brought me to UCL, giving me the opportunity to get involved with a branch of science that I was fascinated, but I did not have any prior experience. I would like to thank him first of all for the fact that he trusted me, and then for all of his support during the first year of my PhD and the rest collaboration we had on the specific topics.

Alex Shluger: He became my second supervisor when Peter left for PNNL. Alex has in depth knowledge of physics and I feel lucky that I worked with him, as he managed to teach me not only science, but also how to think and approach certain problems.

Alex Côté: He helped me a lot with his expertise to understand and implement molecular dynamics simulations. Besides that, he is the only Greek friend that I have in London and this makes him somewhat more special. He was a great support during these years and I will miss the discussions accompanied with coffee that we had at UCL together.

IHI Corporation: I would like to thank the experimental collaborators in Japan for their financial support.

A9 office: I met very nice people who made this office an enjoyable place to work. Georg, Steve, Kugan, Andrew, Callum, Jack, Giulia and Francesco. A special thanks goes to Martin, who was the heart of this office.

Friends: Yasmine, Gabriella, Georg, Kane, Tassem. I met a lot of people at UCL during the past 3 years and I had some good time with many of them. However, these five people are the most important and they will probably be my friends forever.

Emilie: One of the most important people not only in London but in my life in general. A thank you is not enough, as the gratitude that I owe to Emilie cannot be expressed. A steady and constant companion throughout my PhD almost from day one and her care, love and support were invaluable during the last three years.

Parents: Because of their unconditional love during all of my life, as they just love me for who I am.

Contents

List of Figures

List of Tables

1 Introduction

1.1 Structure of the glass

The silicate glasses are amorphous solids which do not exhibit long-range order. The short- and medium-range order of their structure have been characterised in detail by advanced experimental techniques, such as X-ray absorption fine structure (XAFS),[1–3] nuclear magnetic resonance spectroscopy (NMR)[4–6] and neutron diffraction,[7–10] combined with molecular dynamics simulations.[5,11–19]

The structural properties of amorphous SiO_2 glass are well described by the continuous random network model (CRN) proposed by Zachariasen.[20] According to this model, silicon atoms in vitreous SiO_2 are invariably coordinated by 4 oxygen atoms, forming well defined SiO_4 tetrahedra, as shown in figure 1.1. These tetrahedra form a polymerised network, where each tetrahedron shares an oxygen atom with four other SiO_4 units, and the oxygen atoms shared by two tetrahedra are labelled as bridging oxygens (BO). It is also assumed that there is a random distribution of inter-tetrahedral angles in the glass network and this is the origin of the lack of long-range order observed in amorphous silica.

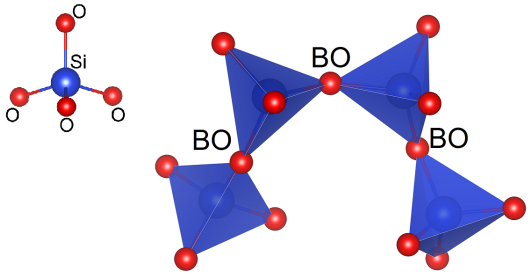

Figure 1.1: Tetrahedral coordination geometry for silicon atoms, formation of SiO_4 tetrahedra within the glass network, and corner sharing connection through bridging oxygen atoms. Blue ball is Si and red ball is O.

According to Zachariasen, specific rules determine which type of systems can form CRN oxide glasses,[20] and they are:

- No oxygen atom may be linked to more than two cations.
- The cation coordination number must be small: 3 or 4.

- Oxygen polyhedra share corners, not edges or faces.

- For three dimensional networks at least three corners must be shared.

In general, all the above rules should be satisfied for glass formation to occur, while these rules have been found to be quite good, not only for predicting glass formation but also for describing the structure of the main glass forming oxides: SiO_2, GeO_2 , B_2O_3 and P_2O_5.[21,22] It is noted that Si, Ge, B and P are usually referred to as network formers of the glass network.

However, the majority of technologically significant glasses contain additional oxides, as impurities in the pure glass. Amorphous SiO_2 and/or B_2O_3, doped with alkali and alkaline-earth oxides,[23] is used for various applications and they form the basis for a wide range of commercially available glass products. Silicate and borosilicate glasses modified with these cations are used as window glasses, solid electrolytes and for nuclear waste disposal.

The modified continuous random network (MCRN) model is able to describe the structural properties of these glasses successfully.[20] The random network of the SiO_4 tetrahedra is significantly modified by the addition of impurities, which usually are alkali and alkaline-earth ions. The modifier cations break the bonds between the Si and O atoms and they are linked predominantly to the SiO_4 tetrahedra with weak and non-directional bonds to oxygen atoms, which are referred to as non-bridging oxygen (NBO), as can be seen, for example, in figure 1.2(a) for a sodium silicate glass. The cation modifiers tend to cluster within the glass structure at low concentrations (see figure 1.2(b)), while, conversely, they form channels at high concentrations. These channels can percolate through the bulk and create primary diffusion pathways, which play a key role in the transport properties of the glass.

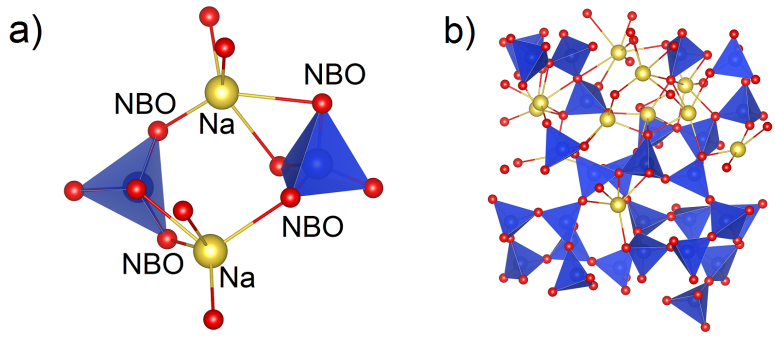

Figure 1.2: Results from a molecular dynamics simulation of a $Na_2O{-}3SiO_2$ glass composition. (a) The addition of Na_2O leads to the creation of non-bridging oxygen atoms within the glass structure, bonded to one Si and one Na; (b) The Na cations have a heterogeneous distribution and they form clusters inside the glass. Blue ball is Si, yellow ball is Na and red ball is O.

1.2 Ion migration

Solids with high ionic conductivity presently attract considerable scientific interest because of their potential applications as solid electrolytes[24,25] in electrochemical devices such as batteries[26,27], chemical sensors[28,29] and "smart windows".[30] The remarkable property of super ionic solids is the selective ionic mobility in an otherwise nearly frozen material.[31,32] The mobility of the ions plays a critical role in the physical properties of many silicate glasses. For instance, in alkali silicate glasses, the resistance of the glass to dissolution, i.e. the chemical durability, depends on the rate of transport of alkali ions to the surface of the glass.[33] The mobility, in turn, depends on the atomic structure of the glass, which defines the possible pathways available for migration. It is noted that, in contrast with crystalline materials, the identification of these pathways in an amorphous structure is not a straightforward task, as its disordered nature makes it complicated to interpret macroscopic transport measurements in terms of microscopic mechanisms, simply because of the difficulties involved in unravelling the atomic scale structure of the glass.[34]

It is generally appreciated that the ions diffuse within the glass structure by a hopping process, and the mechanisms of migration can be viewed as "jump and reside" mechanisms.[35–37] The ions jump between well-defined sites, which correspond to sites that the coordination geometry of the local environment around the ions is of similar character. The work of Park and Cormack was the first modelling study to describe the jumps of alkali ions from one site to another in a mixed lithium potassium silicate glass.[38] They examined in detail the migration of the two alkali cations, in order to identify the jump processes involved, and they revealed that the alkali ions have a larger probability of jumping into sites that were previously occupied by the same type of alkali ion, than into other type of sites, highlighting their preference of jumping into sites with similar local environments. In addition, they found that the alkali ions diffuse through the alkali rich regions, which are possible for the network modifying cations within the glass structure. Recently, Cormack *et al.* studied the migration of sodium cations in silicate glasses and they identified jumps of Na ions in empty positions within the glass structure, revealing a vacancy-like mechanism for the cation migration.[39]

It has been observed that if some of the alkali component in an alkali containing glass is replaced by a different alkali species, then the ionic diffusivity of both alkali ions decreases in the mixed alkali composition, compared to the corresponding single-alkali glasses.[40–42] A notable feature of the mixed alkali effect is its non-linear behaviour, as the change in diffusion coefficients, or related properties such as ionic conductivity, is highly non-linear and can be several order of magnitude.[43] It is noted that the mixed alkali effect is an excellent example of a compositionally dependent phenomenon, since the transport properties of the alkali ions (or other mobile ions, which can have the role of the cation modifier) are ultimately governed by the structure of the glass, and the challenge for a computer simulation is to reproduce, qualitatively, these compositional dependences.[44]

During the few past decades, the mixed alkali effect in alkali silicate glasses has been thoroughly explored via experimental work and molecular dynamics simulations.[40,41,45–53] Several phenomenological and physical models have been proposed to describe the effect, such as the strong[54,55] and the weak[56–60] electrolyte models, the diffusion controlled relaxation model[61,62] and the jump diffusion model.[63] Recently, the introduction of the dynamic structural model[64–67] has helped to demonstrate a more coherent picture.[40,52,68–70] This model is based on an energy landscape approach, in which the unoccupied cationic sites initially are associated with a relatively high potential energy, and as the previously unoccupied sites become occupied the surrounding atoms in the glass network are ordered. In addition, X-ray absorption,[71,72] NMR[73,74] and infra-red spectroscopic[75,76] measurements, together with data from neutron and X-ray scattering,[77] revealed that the mixed alkali effect has a structural origin associated with a cationic potential energy mismatch effect. It is also noted that the dynamical structural model has been supported by results from both Monte Carlo modelling[77] and molecular dynamics simulations.[19,36,66]

1.3 Nuclear waste glasses

In the current conditions of cost-effective and environmentally-friendly energy production, the use of nuclear energy has been suggested as an alternative approach to carbon based methods, for a quite long time.[78,79] However, the applicability of nuclear energy on a large scale has been constrained by the obstacle that creates the necessity to immobilise the large stockpiles of high level nuclear waste that have been produced over the previous 50 years,[80,81] by commercial energy generation and nuclear weapons development.[82,83] The high level nuclear waste is a by-product of the chemical separation of re-usable "unburnt" uranium and plutonium from spent nuclear fuel, which leaves behind waste fission products and minor actinides,[84] and its composition varies slightly between different reactor types, fuel cells and operating conditions. The storage of high level nuclear waste in a liquid form has been considered, during the previous years, as an adequate short-term solution,[85] nevertheless, the mobile nature of the liquid requires a high degree of maintenance.

The conversion of a waste into a waste form is called immobilisation. Several types of matrix materials and techniques are available for the immobilisation of nuclear waste,[86] and the ultimate goal for all of them is to generate a waste form that is stable, can be efficiently treated and is suitable for long-term geological disposal.[85] However, the choice of waste form to use for nuclear waste immobilisation is a difficult decision, and it is noted that durability is not the sole criterion.[87] In any immobilisation method, where radioactive materials are used, the process and operational conditions can become complicated, particularly if operated remotely and equipment maintenance is required. Therefore, priority is given to reliable, simple, rugged technologies and equipment which may have advantages over complex or sensitive devices.[87] In addition, the choice of the immobilisation technology depends on the physical and chemical nature of the waste,

and also the acceptance criteria for the long term-storage and disposal facility to which the waste will be consigned.

A series of regulatory, process and product requirements has led to the investigation and adoption of a variety of matrices and technologies for nuclear waste immobilisation. In most countries high level nuclear waste has been incorporated into alkali borosilicate or phosphate vitreous waste forms for many years and vitrification is an established technology.

Amorphous silica was used originally as the base-glass for high level waste due to its high chemical durability. However, the high temperatures (typically ≈ 1800 K) required to produce a pure SiO_2 glass led to the direction of using different glass compositions. Network formers, other than Si, are added to the glass configuration, and particularly, the inclusion of boron oxide can bring the melting temperature down to ≈ 1300 K, without significantly affecting the glass network. Further additions of sodium and lithium oxides are able to reduce further the glass transition temperature and improve the solubility of the waste into the glass network.[87–89] Hence, an alkali borosilicate glass waste form is one of the preferred choices for the storage of high level nuclear waste, because of its high chemical durability and the adaptability towards different techniques. Moreover, a further benefit of using borosilicate glasses is that they are particularly resistant to the effects of radiation when in storage and importantly remain thermally stable at the temperatures produced by radiogenic processes ($\approx 500°C$).[90] It is noted that other glass compositions have been also investigated and tested as candidates[91–94] for nuclear waste immobilisation, such as phosphate glasses, as well as a variety of other solid materials including ceramics and glass-ceramics.[85,95–102] The exact compositions of nuclear waste glasses are tailored for easy preparation and melting, avoidance of phase separation and uncontrolled crystallisation, and acceptable chemical durability.

Vitrification is a technology that has been used for high level nuclear waste immobilisation for more than 40 years in France, Germany, Belgium, Russia, UK, Japan and USA. The vitrification involves melting of waste materials with glass-forming additives, so that the waste contaminants are incorporated into the macro- and micro-structure of the final vitreous product.[87] The chemical process of vitrification is dissolution, where the base-glass is effectively a solvent into which the high level waste dissolves and contributes to the structure of the glass. This technique is most suitable for aqueous radioactive wastes and it has a number of attractive technological advantages:[87]

- Simple production technology adapted from the glass production industry.
- Great capability of the glass to immobilise various elements.
- High chemical durability of glasses in natural wasters.
- Large tolerance of the glass to radiation damage.
- Small volume of the resulting waste form.

Consequently, the high chemical resistance of the glass allows it to remain stable in corrosive environments for thousands and even millions of years, while the excellent durability of the vitrified radioactive waste ensures a high degree of environment protection. Waste vitrification, along with the high waste volume reduction, enables the utilisation of simplest and cheapest disposal facilities and, thus, despite of high initial investment and operational costs, accounting for transportation and disposal expenses, the overall cost of vitrified radioactive waste can be lower than non-vitrified options.

The vitrification technology comprises several stages, starting with evaporation of excess water from liquid radioactive waste, followed by batch preparation, calcination, glass melting, and ending with vitrified waste blocks and potentially small amounts of secondary waste. There are two different procedures available for vitrification; in the one-stage process both waste calcination and melting occurs in the melter, while in a two-stage process the waste is calcined prior to melting.[87] Thin film evaporators are typically used and the remaining salt concentrate is mixed with the necessary additives, and is directed to one or another process apparatus. In both cases two streams come from the melter, the glass melt, which contains most of the radioactivity, and the off gas flow, which contains off gases and aerosols. The vitrification can be performed efficiently at temperatures below 1500 K, because of the volatility of the fission products. It is noted that the hazardous waste constituents are immobilised by direct incorporation into the glass structure, as they are dissolved in the glass melt, some such as Si and B being included into the glass network on cooling, while others such as Li, Na, K, Ca and Mg are confined as modifiers.

One of the technological problems arising during vitrification of heavy metal constituents is segregation of crystalline and/or poly-crystalline phases, which usually have much higher melting temperature than that of the host glass, and hence they can be considered as solid inclusions in the glass melt. In addition, if they reach macroscopic size they can form deposits at the walls of the crucible and obstruct the flow of the glass melt, leading to a disruption of the vitrification process, and hence of the operation facilities.

Molybdenum is an element that is found in high concentrations in high level nuclear waste and it is known to have low solubility in borosilicate glasses.[103] For instance, MoO_3 present in excess of 1 wt % results in the phase separation of complex molten salts during vitrification, and the formation of the so-called yellow (due to its colour) phase. This phase is associated with formation of crystalline particles, phase-separated from the rest of the molten glass. Yellow phase creates a number of technical and scientific challenges. In particular, (i) yellow phase concentrates at the bottom of the melter and sticks the nozzle of effluent molten glass, which accelerates corrosion of the melter; (ii) yellow phase also contains a wide range of fission products and is highly water soluble, which could lead to increased leaching of radioactive nuclei from the vitrified wastes.[104] The yellow phase formation during melt cooling must be controlled throughout the preparation of radioactive nuclear glassy waste forms, and the challenge on the scientific side is to identify atomic-scale processes that lead to the formation of

molybdate crystals and also find approaches to suppressing these processes.

1.4 Localised states and defects

An extensive use of powerful laser radiation in many industrial and research applications such as optical communications,[105] data storage,[106] photolithography[107] and laser processing[108] of different materials gives rise to the problem of stability of optical materials under intensive optical illumination. The main components of the majority of optical devices are still silicate glasses,[109] and therefore their durability is of high importance for the above applications. The problem of interaction between optical radiation and matter is associated with different thermal effects and different types of photoionisation, while the interaction with light is considered in the frame of elementary excitation of different electronic states in the material under study.[110] Excitons, electrons and holes are representatives of elementary electronic excitations in crystals and glasses. Excitation of electrons from the valence band or ground states of impurities or defects creates mobile electrons in the conduction band, and hence, electron and hole migration, followed by trapping or recombination, is the basis for the most part of photo-induced processes.[111]

The electronic properties of amorphous materials are determined by the short- and medium-range order of their structure. In the wide-gap insulating glasses some basic properties of electronic states, such as the intrinsic absorption spectrum, are determined specifically by the short-range order. The study of many different disordered systems allow the introduction of a classification of the electronic states as delocalised and localised states, separated by a mobility threshold.[112] The motion of the delocalised electronic excitations is defined by the medium range-order structure. However, the lack of long-range order in glasses accounts for the poor transport of absorbed energy and the disorder structure of glass should lead to localisation of elementary excitations. Hence, below the mobility threshold, the localised electron states, which manifest themselves on the intrinsic absorption threshold, i.e. in the range of the bottom of the conduction band in glasses, can play a significant role in many properties of an amorphous material under irradiation.[113]

A theoretical approach, started with Mott's work at 60's, is available to describe the optical properties and photo-stimulated phenomena in glasses. Mott and Davis defined the localised states in amorphous materials as traps with an overlapping of the wavefunctions and they have summarised them based on experimental data from chalcogenides.[112] The electronic and geometric structures of the localised states are related to structural motifs of the glass host, and the luminescence method is the experimental tool can be used in order to make observations of these states in a short-range order.[114,115] Localised states were discovered in silica glasses and alkali silicate glasses,[116] as well as in germanate[117] and phosphate glasses,[118] by the study of luminescence, absorption and photoelectron emission. In contrast to crystals, localised electron states in disordered systems are not considered to be related to point defects, but correspond to

energy states of the host atoms.[119]

In order to describe the absorption spectra of Na−doped SiO_2 glass, Mott and Davis[112,120] proposed a model based on Siegel's data,[121] which assumes that a complex of non-bridging oxygen and sodium ions produces donor levels in the SiO_2 band gap, 2.5 eV above the valence band. An excitation of sodium silicate glass by photons whose energy lies in the fundamental absorption region leads to the creation of self-trapped excitons.[112] Trukhin *et al.* concluded that an ensemble of structurally non-equivalent luminescence centres are responsible for the long-wavelength intrinsic absorption tail of sodium silicate glasses and the polarised luminescence, for the case that the excitation takes place with polarised light.[122,123] Hence, because of this property, these local anisotropic luminescence centres were attributed to localised states of the host material, and they were designated as L-centres in sodium silicate glasses.

As mentioned above, the glass does not have a long-range order in its vitreous network, and this makes the notion of an extended network defect, like a dislocation for instance, worthless. On the contrary, in the short-range order of the amorphous structure, the concept of point defects is employed, which corresponds to the removal of an atom from its ideal position. The most popular and extensively studied defect trap in oxide glasses is the E′-centre, which is associated with an oxygen vacancy defect in the glass network, and can be described as an unpaired electron trapped in a dangling orbital of an atom (Si, Ge, B, P or Al) bonded to three oxygen atoms. The E indicates that the oxygen vacancy is an electron trapping site, while the number of primes corresponds to the number of electrons trapped at this site. It is noted that many types of E′-centre can be formed and have been observed in quartz and silicate glasses.

The alkali electron centre is a quite well known electron trap that can be detected in silicate glasses. As described in 1.1, alkali cations act as network modifiers in silicate glasses, and their addition leads to the creation of non-bridging oxygen atoms with the alkali cations charge compensating. Each alkali cation introduces and compensates for one non-bridging oxygen,[124] and this results in the formation of electrical dipoles within the glass structure, composed of a negatively charged non-bridging oxygen and a positively charged alkali ion, A^+.[125] The extra electron of the non-bridging oxygen can be excited during irradiation and captured on the A^+ to form A^0 (alkali electron centre - E′) leaving the non-bridging oxygen in a metastable state,[125–127] which, in effect, neutralises the dipole. One possibility, after electron trapping on single alkali cations, is that the electron traps may aggregate to form larger complexes, as due to the loss of the dipole, these electron traps are able to migrate within the glass structure and form clusters with other alkali modifiers.[126–128] It is noted that even though the other alkali cations brought into the clusters have not necessarily trapped an electron of their own, in general, the trapped electrons become spin-paired in large conglomerations.[128,129]

One of the most important defects responsible for the optical and electronic properties in alkali silicate glasses is the non-bridging oxygen hole centre, NBOHC, which has been studied extensively by electron paramagnetic resonance (EPR).[130–140] Irradiation of alkali silicate glasses results in the formation of metastable spin centres, and EPR

signals revealed that, in most cases, there are two induced absorption bands attributed to hole centres, OHC_1 and OHC_2, in higher and lower energy respectively.

The OHC_1 is a $3O{-}Si{-}O^-$ radical formed by charge compensation at the non-bridging oxygen atom. There are two contradictory views about the exact way that OHC_1 is formed and the degree to which it involves alkali cations. One suggests that, following the hole trapping, the compensator alkali cation moves away from the site of the trapped hole, leaving uncompensated the Q^3 unit,[130] whereas the other assumes that the alkali cation does not leave the trapping site and it is located in the direct neighbourhood of the hole centre, remaining strongly coupled to the NBO atom.[137] The OHC_2 centre is less characterised than the OHC_1. Cases[133] and Griscom[130] suggested that the spin is shared between two NBO $2p$ orbitals lying in the NBO$-$Si$-$NBO plane, with the alkali cations being out of this plane. Upon thermal activation, an alkali ion migrates into the plane and the unpaired electron localises on a single NBO atom.[130] Hence, the OHC_2 can be visualised as a hole trapped on the Q^2 species with one of the compensating alkali cations missing.

Recently, Shkrob *et al.*[141] demonstrated, using pulsed EPR and ENDOR (electron nuclear double magnetic resonance), that the OHC_1 is a $3O{-}Si{-}O^-$ radical coupled to a nearby alkali ion, but the cation does not leave the trapping site, supporting in that way the representation proposed by Kordas *et al.*[137] It seems that the NBO$-$alkali bond elongates rather dissociates, and such a picture naturally accounts for the formation of L-centres upon electron tunnelling to OHC_1. In the OHC_2 centre the alkali cation is not coupled as strongly as in OHC_1, and it is proposed that the OHC_2 centre is a hole trapped on a tetrahedral $2O{-}Si{-}O_2^{2-}$ unit or a planar $O{-}Si{-}O_2^-$ unit.

1.5 Scope of this thesis

In this work a range of multicomponent silicate glasses that pose a number of scientific and technological challenges is investigated using classical and *ab initio* simulations. The calculations presented in this thesis provide atomistic models related to immobilisation of nuclear waste glasses, ion migration in mixed cation silicate glasses and optical properties of alkali silicate glasses.

The methods used to model the glass compositions studied in this thesis are described in chapter 2. The principle of classical molecular dynamics is presented, together with the algorithms implemented to solve numerically the equations of motion. The discussion about classical interatomic potentials, and the background theory related to statistical mechanics will give the opportunity to underline the key features related to a molecular dynamics simulation. In the second part of this chapter the density functional theory approach is presented, as it is the method used for the quantum mechanical calculations carried out in this thesis. All the important aspects necessary to provide an overview of the method are described; Hohenberg-Kohn theorems, the Kohn-Sham scheme, exchange-correlation functionals, basis sets and pseudoptentials. A quantum mechanical representation of molecular dynamics, the *ab initio* Born-Oppenheimer mo-

lecular dynamics approach, is presented afterwards, and in the final part of this chapter, all the specific details and techniques used to generate and characterise the simulated glasses are discussed. In addition, a short description of the several calculated properties for the modelled systems is provided.

Mixed alkali borosilicate glasses show a complex composition−structure relationship, which has an effect on many of their properties. In chapter 3 the relation between the chemical composition and the glass transition temperature is examined with molecular dynamics simulations, and this kind of effort will help to the industrial collaborator in Japan (IHI) with rational design of new glasses. The modelled glass systems are relevant to the experimental compositions from IHI, and this study is focused on the implementation and validation of a suitable method to calculate the glass transition temperature and compare the modelling results to the experimental data. In addition, the structure and the electronic properties of a series of lithium sodium borosilicate glasses, with pre-defined concentrations of the oxides, are investigated using *ab initio* molecular dynamics simulations and ground-state density functional theory calculations.

Molecular dynamics is one of the theoretical approaches to understand the mechanisms of yellow phase formation in high level nuclear waste glasses. However, describing the nature of chemical bonding of molybdenum in nuclear glasses and predicting accurately its solubility limits is a difficult task because of the complex chemical composition of the glass host. In chapter 4 the first computational approach based on *ab initio* molecular dynamics simulations to model the local atomic structure of molybdenum in mixed alkali and mixed alkali alkaline-earth borosilicate glasses is presented, in order to investigate the dependence of the solubility of the molybdenum on the chemical nature and molar composition of the glass host. The results significantly extend the understanding of bonding in Mo-containing nuclear waste glasses and evaluate the yellow phase formation within the glass structures. This work contributes towards the effort to design glasses, in which the crystallisation of alkali and/or alkaline-earth molybdates during the vitrification process is suppressed.

Experimental research has revealed that in mixed alkali alkaline-earth silicate glasses different mixed cation effects, than that of the mixed alkali effect, occur in the ionic diffusivity of the alkaline-earth cations. In chapter 5 the first molecular dynamics simulations of mixed cation silicate glasses of the composition $A_2O{-}2MO{-}4SiO_2$, with A = Li, Na, K and M = Ca, Sr, Ba are presented, in order to investigate the effect of the nature of the cations on the mobility of the alkaline-earth ions within the glass network. A detailed structural analysis is performed to analyse the local environments around the different alkaline-earth cations. The results from the modelling of the transport properties of the alkaline-earth ions are in a qualitative agreement with the experimental observations, and provide an atomic scale representation of the processes that result in the enhancement or suppression of their ionic diffusion.

Sodium silicate glasses are among the most widely used materials in contemporary optics. However, their electronic structure and the mechanisms of electronic processes are still poorly understood. In chapter 6 the first *ab initio* calculations of the electronic

and geometric structures of localised states in sodium silicate glass are presented. The atomistic and electronic structures of the ground and excited states are calculated, together with the electronic properties of the individual electron and hole traps. The predicted excitation and luminescence transition energies are in good agreement with experimental data, and the calculations provide a detailed atomistic picture of localised states in these important glasses.

A final synopsis is given in chapter 7, in order to summarise the calculated results presented in this thesis and their impact on the relevant study in each chapter. In addition, further potential calculations related to the glasses and their properties modelled in this thesis are suggested for future computational studies.

2 Methods

2.1 Computer simulations

Computational studies have become very popular during the last two decades because of the increasing power of computers and the development of efficient numerical algorithms. The computer simulations are *in silico* experiments, which act as a bridge between real experiments and theories, and also they are able to connect the microscopic to macroscopic behaviour of the system.[34,142,143] They are an established tool to study complex systems, relatively simple and inexpensive, where everything can be measured, in principle, and gain insight into the properties of materials. A computer simulation can investigate a system on a level of detail which is not possible in real experiments or analytical theories. From one side, simulations can provide essential information in the atomistic level, useful to rationalise and tailor specific experimental processes or propose new experiments. From the other side, a simulation can solve a problem, through a numerical method, and gives the opportunity to validate and/or improve an already existed theoretical model. In addition, through a simulation it is feasible to calculate particularly important macroscopic properties under conditions which are not accessible experimentally, or which would require very expensive experiments.

In their early days computer simulations were mainly used to address questions related to statistical physics (by using hard and soft spheres).[34] Later on, when machines became more accessible and more powerful, simulations became a tool to study the properties of real materials. The two main practises of conducting computational studies on materials are classical approaches and *ab initio* methods. In the first case, the most common approach is the classical molecular dynamics, where the interactions between the particles that constitute the material are described by an interatomic potential. The parameters of the potential are tuned in that way such that certain macroscopic properties of the simulated system match with experimental or *ab initio* data of the material. In the second case, the *ab initio* methods evolved from the idea of density functional theory and are based on quantum mechanics. In the *ab initio* formalism the interaction potential does not rely on a fixed functional form, but the electronic degrees of freedom of each atom are used instead to compute the force that acts on each atom of the system. Thus, *a priori* the only input needed for these calculations are the species of the particles.[144]

In this thesis, classical and *ab initio* methods, either separately or in combination, are used in order to simulate the systems under study. The choice of the method is based on the particular properties of the systems to be calculated, the availability of an accurate classical potential able to reproduce the glass structure and also the available computational resources.

2.2 Classical Molecular Dynamics

2.2.1 Set up the problem: equations of motion

Classical molecular dynamics (MD) is a computational method for the modelling of materials, which includes the effects of both temperature and time.[34,145] It has been used with some considerable success to probe the structure and the dynamics of a vast range of modelled systems. The application of MD to the study of a system may provide an atomic scale picture of the structure, an understanding of composition-atomic structure relationships and an insight into the atomic migration mechanisms active in materials. The principle of the MD is simple; the evolution of an ensemble of atoms, which is started from any initial point, is followed as a function of time to sample the generated trajectory in phase space.[44]

Hence, the aim of the MD is to determine the trajectory of the particles.[145,146] The equations of motion can be represented in Langrangian, Hamiltonian or Newtonian form, which are all equivalent. Using the last one, the positions and velocities of each of the atoms are determined from classical mechanics, through Newton's second law:

$$m_i \frac{d^2\vec{r}_i}{dt^2} = \vec{F}_i \tag{2.1}$$

where m_i is the mass and $\vec{r}_i$ is the position of an atom i, while $\vec{F}_i$ is the force acting on this atom. For a set of N interacting particles moving in a conservative field the forces acting on a particle can be determined through the potential energy function V and hence the equations of motion can be written as:

$$m_i \frac{d^2\vec{r}_i}{dt^2} = -\nabla_{\vec{r}_i} V(\{\vec{r}_i\}) \tag{2.2}$$

where $\{\vec{r}_i\} = (\vec{r}_1, \vec{r}_2, ..., \vec{r}_N)$ is the complete set of $3N$ particle coordinates.

This approach leads to a set of $3N$ coupled second-order ordinary differential equations needs to be solved to obtain the trajectories of the atoms. In principle, all physical properties of the collection of N particles can be calculated from the knowledge of its phase space trajectory. The integration demands both the force and the first derivative to be continuous which implies that the potential energy function and its first and second order derivatives should be also continuous.[147] Moreover, the specification of $6N$ integration constants is required, $3N$ for the positions and $3N$ for the velocities of the particles, which correspond to the initial conditions of the system at $t = 0$, $\{\vec{r}_i(0), \dot{\vec{r}}_i(0)\}_{i=1,2,...,N}$. The initial positions $\{\vec{r}_i(0)\}$ can be determined from available

crystallographic and structure data from the literature, usually obtained from diffraction patterns, while the initial velocities $\{\dot{\vec{r}}_i(0)\}$ can be random or may be chosen to satisfy the Maxwell-Boltzmann distribution corresponding to a desired temperature. Another approach is to start with zero velocities for the particles which then are rescaled until the temperature reaches the target temperature and preserves this value.

2.2.2 Solve the problem: integration schemes

The potential energy of an atom is dependent on the interactions with the other atoms in the system and since each particle interacts with all the others a $N-1$ body problem asks for solution, which means that the equations 2.2 cannot be solved analytically. The set of the coupled 2^{nd} order differential equations can be approximately solved instead by using a numerical method for the integration.

Treating time as a discrete quantity $t = k\Delta t$ and by given knowledge of the initial conditions the set of the $3N$ equations of motions can be solved to yield positions and velocities at later times $t + \Delta t$, $\{\vec{r}_i(t + k\Delta t), \dot{\vec{r}}_i(t + k\Delta t)\}_{k=1,2,\ldots,L}$. Following this approach, a discrete trajectory in the phase space is generated over consecutive time intervals Δt called timestep. The choice of the value of the timestep is a crucial decision for the success of the numerical integration scheme. A large value of Δt leads to less integration steps over a certain amount of simulation time, and therefore, less computational cost. However, the larger the Δt, the poorer the sampling of the trajectory in the phase space and thus a less accurate solution for the equation of motions to approximate the correct classical trajectory. In principle the smaller the timestep the more exact the solution to equations of motion becomes. The goal is an operational balance between accuracy of the results and computational expense.

An efficient numerical algorithm, called integrator, is needed to propagate the solution and hence the trajectory step-by-step. A good and well behaved integrator has to be simple and fast enough, and also be able to provide stable trajectories by using relatively large Δt. In addition, the temporal evolution must be reversible and the mechanical energy has to be conserved. The integrator needs to compute the forces not too frequently and the phase space volume needs to be preserved according to Liouville theorem. Different numerical algorithms are available to integrate the equations of motion all based on Taylor expansion in t to obtain positions and velocities at a later time $t + \Delta t$.

A simple numerical integration scheme is the Verlet algorithm.[148,149] This integrator has many advantages including great stability and time-reversibility. To derive the Verlet algorithm the Taylor expansion of the position vector at time t for two different timesteps $\pm\Delta t$ needs to be considered:

$$\vec{r}_i(t + \Delta t) = \vec{r}_i(t) + \frac{d\vec{r}_i(t)}{dt}\Delta t + \frac{1}{2}\frac{d^2\vec{r}_i(t)}{dt^2}\Delta t^2 + \frac{1}{6}\frac{d^3\vec{r}_i(t)}{dt^3}\Delta t^3 + O(\Delta t^4) \tag{2.3}$$

$$\vec{r}_i(t-\Delta t) = \vec{r}_i(t) - \frac{d\vec{r}_i(t)}{dt}\Delta t + \frac{1}{2}\frac{d^2\vec{r}_i(t)}{dt^2}\Delta t^2 - \frac{1}{6}\frac{d^3\vec{r}_i(t)}{dt^3}\Delta t^3 + O(\Delta t^4) \tag{2.4}$$

The sum of the two expansions above results in the following recursive expression of the Verlet algorithm:

$$\vec{r}_i(t+\Delta t) = 2\vec{r}_i(t) - \vec{r}_i(t-\Delta t) + \vec{a}_i(t)\Delta t^2 + O(\Delta t^4) \tag{2.5}$$

The acceleration $\vec{a}_i(t)$ is calculated by the corresponding force, which in turn is determined from the position $\vec{r}_i(t)$ trough the equation 2.2. Consequently, this integration scheme stores the positions and forces only, and the errors in this algorithm are of 4^{th} order, which are very small in comparison with the intermolecular distances.[147] The disadvantage of the Verlet integrator is mainly the absence of a velocity term, which makes the estimation of the velocities of the particles not a straightforward task, since the position vector at $t + \Delta t$ needs to be determined first and then the two Taylor expansions from equations 2.3 and 2.4 needs to be subtracted. Thus, the velocities are computed indirectly through finite differences as:

$$\vec{u}_i(t) = \frac{\vec{r}_i(t+\Delta t) - \vec{r}_i(t-\Delta t)}{2\Delta t} + O(\Delta t^2) \tag{2.6}$$

The obstacle is that to calculate the positions at $t + \Delta t$, the knowledge of the positions not only at time t but also at the previous step $t - \Delta t$ is needed and thus the Verlet scheme it is not a self-starting algorithm. It is highlighted also that the errors in the calculation of the velocities are of 2^{nd} order, which makes these calculations much less accurate than those of the positions.

The velocity Verlet integration algorithm,[150] which is an extension of the original Verlet algorithm, improves the efficiency of the scheme by overcoming the need of the Verlet integrator to store previous simulation frame data in order to calculate velocities. The position and velocity of each atom are calculated as:

$$\vec{r}_i(t+\Delta t) = \vec{r}_i(t) + \vec{u}_i(t)\Delta t + \frac{1}{2}\vec{a}_i(t)\Delta t^2 + O(\Delta t^4) \tag{2.7}$$

$$\vec{u}_i(t+\Delta t) = \vec{u}_i(t) + \frac{1}{2}[\vec{a}_i(t) + \vec{a}_i(t+\Delta t)]\Delta t + O(\Delta t^3) \tag{2.8}$$

In this scheme the velocities are calculated directly from the second equation. This algorithm can be viewed as predictor-corrector, where with knowledge of the positions and velocities of atoms at a specific time, it is possible to calculate their positions and velocities at some time in the future. The state of the system in the future can be calculated by simply repeating this procedure until the desired time is reached. It is noted that the velocity Verlet algorithm is one of the most widely used in materials modelling studies, as it fulfils all the requirements of a good integrator, provides numerical accuracy and its implementation is an easy task.

2.2.3 Empirical interatomic potential

In classical MD simulation of complex systems, the accuracy and the quality of the calculated results are dependent on the quality of the description of the forces acting on the atoms in the modelled system, and thus depend on the potential model that defines the rules governing interactions within the system.[147] The intermolecular force fields are conservative, and hence the forces can be calculated through the potential energy function, which determines the types of the different interactions between atoms and describes the manner the potential energy of a system containing N atoms depend on the atomic coordinates $\{\vec{r}_i\}_{i=1,2,...,N}$. The many-body expansion of the total potential energy of a system of N atoms can be expressed as follow:

$$V_{tot}(\{\vec{r}_i\}) = \sum_i V_1(\vec{r}_i) + \sum_i \sum_{j>i} V_2(\vec{r}_i, \vec{r}_j) + \sum_i \sum_{j>i} \sum_{k>j} V_3(\vec{r}_i, \vec{r}_j, \vec{r}_k) + ... \tag{2.9}$$

where the notation indicates a summation over all distinct pairs between i and j without counting any pair twice and $\{\vec{r}_i\} = (\vec{r}_1, \vec{r}_2, ..., \vec{r}_N)$ represents the complete set of $3N$ particle coordinates. The first term, $V_1(\vec{r}_i) = V_i$, is the single-particle energy, which is normally zero, except for the case that an external force field is acting on the particles, the second term, $V_2(\vec{r}_i, \vec{r}_j) = V_{ij}$, are the two-body interactions or pairwise potential, in which the interaction of a pair of atoms depends solely on the distance between the atoms and the third term, $V_3(\vec{r}_i, \vec{r}_j, \vec{r}_k) = V_{ijk}$, are the three-body interactions that describe the alteration of pairwise interactions due to the presence of a third atom. Usually for the modelling of oxide glasses only the two-body interactions are considered and higher order terms are neglected.

Therefore, an accurate pairwise potential is a critical input to the equation 2.2 in order to obtain an accurate trajectory of the particles in the phase space. A classical Born interpretation of the system is adopted, in which atoms are treated as interacting point particles, and electrons not explicitly taken into account. The two-body interactions are described through a force field, which is defined by a set of specific parameters and (most often) analytical functions, depending on the mutual positions of the particles. Hence, the total potential energy of the system can be represented as the sum of the pairwise contributions to the energy and reads as:

$$V_{tot} = \sum_i \sum_{j>i} V_{ij}(r) \tag{2.10}$$

where $r = |\vec{r}_i - \vec{r}_j|$ is the pair separation and the interaction of each pair of atoms depends merely on this distance. The potential energy of a pair of interacting species can be decomposed to short- and long-range contributions:

$$V_{ij}(r) = V_{long}(r_{ij}) + V_{short}(r_{ij}) \tag{2.11}$$

The long-range or Coulombic term arises due to the electrostatic repulsion/attraction between the ions and its computation requires specific methods, such as the Ewald summation[151] for example. The short-range term defines the Van der Waals interaction between two ions. The short-range contribution is predominant at small interatomic distances and, hence, determines the behaviour of the atoms. The short-range interaction has no power beyond a cut off distance, which needs to be determined in the calculation and its value is chosen so to be consistent with energy conservation and computational efficiency. In case that two particles approach to close to each other, the electron cloud may overlap giving rise to a repulsive force, which originates from the Pauli exclusion principle. Consequently, the addition of the Pauli repulsive potential energy needs to be considered in the total expression of the potential model in order to give a better description of the resulting forces.

An interatomic potential model is usually parametrised by fitting structural and, sometimes, elastic and vibrational properties from experimental data or quantum mechanical calculations, corresponding to specific conditions of temperature and pressure.[147] The pairwise potential usually describes adequately the expressions of the potential energy surface around the minimum, i.e. the equilibrium separations, and it is rather specific to the modelled system, which means that it shows small transferability under compositional changes and/or variations of the physical conditions. Nevertheless, classical MD simulations with the usage of an accurate interatomic potential are computationally inexpensive and give the opportunity to model large sized systems and sample trajectories for long timescales.

2.2.4 Periodic boundary conditions

In practice, physical system sizes, of the order of 10^{23} atoms, are computationally out of reach and MD simulations can model only small samples of the "real" material. Hence, in an MD simulation a sample of the macroscopic system is placed in a finite box with specific geometry called simulation cell. The specifications of the simulation cell, in terms of shape, size and total number of atoms, are related to the molar composition and density of the modelled system.[152] Several challenges are raised related to the ability of this "small" system to describe sufficiently the properties of a macroscopic sample. For instance, a volume element in a material is constrained by the surrounding bulk, and at a surface these constraints break down and sometimes quite extensive atomic relaxation can occur. In a macroscopic system, only a small percentage of the atoms are at the surface and therefore contribute little to bulk properties. However, this is not the case for the small number of atoms constituting the simulation cell, in which, due to the surface area to volume ratio, a few atoms are located on the simulation box surface and, thus, have different environment than those in the bulk. Consequently, the atoms placed on the surface experience different forces than the atoms in the bulk, which may affect the properties of the modelled system and hence can hinder attempts to obtain bulk properties from such a system.

In an MD simulation, to avoid the contributions from surface effects and also to overcome the obstacle of the finite size of the simulation cell, periodic boundary conditions (PBC) are implemented to reproduce the infinite bulk around the MD sample by replication of the simulation cell in the x, y and z directions. Since the simulation cell together with the total number of atoms are replicated in all space directions the motion of the atoms in the basic simulation box is correlated with their motion in the respective images. An atom leaving the basic simulation box at one side, it re-enters the box through the opposite side with the same velocity, while any atom crossing a periodic boundary is wrapped around to appear at the other side of the simulation cell. Consequently, within this framework there are no walls at the boundaries and no surface molecules, while also the total number of atoms in the simulation cell is maintained constant. PBC are applied in molecular dynamics to simulate bulk glasses, liquids, crystals or mixtures, and the simulation cell may take various shapes according to the characteristics of the modelled system. It is noted that this introduces periodicity to glasses that would not be present in a real material. A cubic simulation box with periodic boundary conditions creating an isotropic medium is adopted for all the computationally generated glasses that reported in this thesis.

The choice of the boundary is arbitrary and influences the short- and long-range interactions between the atoms in the modelled system. The imposed artificial periodicity should be bear in mind when considering properties influenced by long-range correlations. For the short-range interactions, in case that the potential range is not too long, the minimum image convention approach can be applied.[34] Then, the short-range interactions are calculated by assuming that the potential energy of each atom is dominated by its interaction with the nearest atoms or nearest periodic images of its neighbours. It is noted that the atoms interact only when they are separated by a distance smaller than a specific cut off distance at which the potential is truncated. This cut off distance is determined so to be smaller than or equal to half the simulation box length in order to ensure consistency with the minimum image convention.

2.2.5 Statistical ensembles

The output properties of the numerical integration of the equations of motion 2.2 are the positions and velocities of the atoms which consist the modelled system. However, a macroscopic property, such as the temperature of the simulation, as well as any other bulk property of the system needs to be reconciled with the atomic quantities probed by the simulation. The statistical mechanics provides the bridge between the atomic scale and macroscopic properties and the central idea is the concept of the thermodynamical ensemble.

A thermodynamical ensemble represents all the different ways in which the positions and the velocities of all the atoms in a system can arrange themselves. Each of these states has one or more extensive quantities in common, which are the independent thermodynamic variables of the system, from which all other quantities can be obtained.

Bulk properties are extracted from an ensemble by considering the ensemble average, which essentially means that the macroscopic property of interest is obtained by taking average of the observable value over all the states in the ensemble, where the average is weighted in favour of more probable low energy states. The micro-states are distributed over the phase space with a specific probability density and the average value $\langle A \rangle$ of a macroscopic property A can be calculated as follow:

$$\langle A \rangle = \int A(\Omega) f(\Omega) d\Omega \tag{2.12}$$

where $f(\Omega)$ is the probability density of a micro-state Ω. The probability density of every ensemble is unique, i.e. $f(\Omega) = f_{ensemble}(\Omega)$ and therefore:

$$\langle A \rangle \equiv \langle A \rangle_{ensemble} = \int A(\Omega) f_{ensemble}(\Omega) d\Omega \tag{2.13}$$

where $\langle A \rangle_{ensemble}$ is the ensemble average taken over large number of replicas of the modelled system.

Consequently, this implies that the system should be allowed to evolve in time as long as possible so that it will eventually pass through all possible states. However, in most cases, it is possible to sample only a finite number of these states. In effect during the equilibration state of an MD simulation, each timestep represents a member of the ensemble and as the simulation evolves it provides a way of sampling the more thermodynamically favourable members of the phase space. This leads to the ergodic hypothesis,[153] which denotes that the time average over the states of a single structure is equal to the ensemble average over many structures, $\langle A \rangle_{time} = \langle A \rangle_{ensemble}$. Thus, MD simulations are able to generate enough information to satisfy the ergodic hypothesis, and get reliable knowledge regarding to structural, dynamical and thermodynamical properties in order to study the physical system. Therefore, a sufficient amount of the trajectory in the phase space is required and hence needs to be sampled over relatively long timescales.

The macroscopic properties that remain constant during the simulation often characterise an ensemble. For instance, the total energy E of the modelled system remains constant in the integration of the equations of motion 2.2 for a system of N particles in a cell of fixed volume V. In other words, the state of the system at each MD timestep is a member of an ensemble where the number of the atoms (N), volume (V) of the simulation cell and the total energy (E) are extensive variables.[154] This corresponds to the microcanonical ensemble, NVE, which is the "natural" ensemble in an MD simulation, i.e. a computational method to propagate a system, along a path of constant energy in the phase space and, therefore, it is able to reproduce correctly the true dynamics of the simulation. In practice, the NVE ensemble is used in MD simulations for equilibration runs, until an average temperature of the system is reached, and for production runs, to collect the part of the trajectory which will be analysed in order to calculate the relevant properties of the modelled system.

The thermal processes that give rise to the modelled system during the MD simulation are described through the temperature, which is a macroscopic measurable property mainly due to the kinetic energies of the atoms. The temperature T of a system with N atoms is proportional to its kinetic energy:

$$\langle E_{kin} \rangle = \left\langle \sum_{i=1}^{N} \frac{\vec{p}_i^2}{2m_i} \right\rangle = \frac{3}{2} N k_B T \tag{2.14}$$

where m_i is the mass and $\vec{p}_i$ is the momentum vector of an atom i, and k_B is the Boltzmann's constant. However, the number of the atoms in the system is small with respect to the Avogadro number and also considerable localised fluctuations in the atomic motion take place, which make the control of the temperature a challenging task. In fact these fluctuations are mandatory for the system to explore the configurational space and proceed along its thermodynamical trajectory.[155]

In order to control the temperature in the MD simulations a thermostat is used, which fixes the temperature *a priori* at a specific value, acts as a source of thermal energy and supplies or removes heat from the system whenever is necessary.[34,142] This is the idea of the canonical ensemble, which must allow fluctuations of the temperature during the simulation, whilst making sure that the time averaged temperature remains constant. The canonical ensemble corresponds to a collection of all systems with thermodynamic state characterised by a fixed number of atoms N in a fixed volume V at fixed temperature T, i.e. NVT. The micro-states of this ensemble may take only discrete values of energy and the probability of finding the system in a particular microscopic state j with energy level E_j is given by the Maxwell-Boltzmann distribution.

There are several approaches to perform MD simulations with the NVT ensemble. One approach is the velocity rescaling method, in which the velocities of the particles are rescaled at each timestep (or after a preset number of steps) so that the kinetic energy gives the desired target temperature. The velocities are rescaled by a factor λ to keep the instantaneous temperature $T(t)$ during the simulation close to the requested, target, value T_{req}:

$$\begin{aligned} \vec{u}_i &\rightarrow \lambda \vec{u}_i \\ \lambda &= \sqrt{\frac{T_{req}}{T(t)}} \end{aligned} \tag{2.15}$$

In the limit that the velocities are rescaled at every timestep, the kinetic energy will remain constant in time with zero fluctuations. The statistical mechanics of the canonical ensemble though implies that the ensemble must allow temperature fluctuations during the simulation. In other words, the velocity rescaling approach does not capture the correct energy deviations which occur during the propagation of the modelled system in time. Berendsen suggested a different rescaling approach,[156] in which a timescale is assigned for the updating of the velocities of the particles, rather than assuming that they are completely scaled to the target temperature at each timestep. Underlying this

approach is the assumption that the system is weakly coupled to an external heat bath with a specific coupling time constant τ, which corresponds to the timescale of the heat transfer, i.e. the timescale on which the target temperature is reached. Hence, in the Berendsen thermostat the rescaling factor of the velocities of the particles reads as:

$$\lambda = \sqrt{1 + \frac{\Delta t}{\tau}\left(\frac{T_{req}}{T(t)} - 1\right)} \tag{2.16}$$

where Δt is the timestep of the MD simulation. It is noted that, in principle, the Berendsen thermostat does not generate any known ensemble and becomes equal to the rescaling described above when $\tau \rightarrow \Delta t$. Typical values of the relaxation constant are τ = 0.1 - 0.4 ps for a timestep Δt = 1 fs.

An alternative approach of maintaining a system at constant temperature was devised by Nosé,[157,158] in which a reformulation of the equations of motion taking place. In this method the system is again considered to be coupled with an external heat bath at temperature equal to the desired temperature, and a supplementary variable is introduced, which mimics the thermal bath and has the effect to renormalise the time. Consequently, an extra degree of freedom is added to the Hamiltonian of the system, which results in extra kinetic and potential energy for the extended system. The implication of this result is that a microcanonical simulation in the extended system returns a canonical ensemble for the original system, which means that the equations of motion, which are drawn from this modified Hamiltonian, do not represent a microcanonical ensemble or a subset of it, since a canonical distribution of the positions and the velocities of the atoms is obtained. In case that a high energy state is experienced, energy is transferred from the atoms to the heat bath over a set period of time, as the system is gradually driven back in to thermodynamic equilibrium. The time period over which this occurs is known as the thermostat's relaxation time.

The Nosé-Hoover thermostat (originally proposed by Nosé and developed independently by Hoover[159]) uses the friction coefficient ξ to describe the modified equations of motion and control the fluctuations of the temperature. Then, the time evolution of the positions and the velocities of the atoms is governed by the following equations:

$$\frac{d\vec{p}_i}{dt} = \vec{F}_i - \xi\vec{p}_i \tag{2.17}$$

$$\frac{d\xi(t)}{dt} = \frac{1}{Q}\left(\sum_{i=1}^{N}\frac{p_i^2}{2m_i} - gk_BT\right) = \frac{gk_B}{Q}[T(t) - T_{req}] \tag{2.18}$$

where $g = 3N + 1$ is the number of degrees of freedom and Q is the effective "mass" of the thermostat associated with the additional variable which is introduced to the modelled system. The parameter Q is important for regulating the rate of exchange of the system energy with the imaginary heat bath and hence it is related to the relaxation time of the thermostat. It is noted that in equation 2.17 the velocity update of an atom resembles Newton's equation with an additional force that is proportional to the

velocity of the atom, and corresponds to the friction term. The Nosé-Hoover thermostat rigorously generates the canonical ensemble thermodynamics and can approximate the true dynamics of the system because the time evolution of the atoms is deterministic, and does not involve stochastic changes. However, it is noted that this thermostat can at times exhibit pathological behaviour for specific modelled systems.

Often it is desirable to maintain a simulated system at both constant temperature and pressure. In such cases the MD simulation is performed with the isobaric-isothermal ensemble, which is characterised by a fixed number of atoms N, a fixed pressure P and a fixed temperature T, i.e. NPT. This ensemble is used to study structural modifications due to pressure or a phase transition and, in principle, it is the most realistic and the closest to experimental procedures. In a thermodynamic sense, the volume becomes a dynamical variable and systems at constant pressure are able to exchange volume with their surroundings (e.g., by mimic the action of a piston on the box). The cell volume therefore is allowed to change and, consequently, simulated systems at constant pressure involve volume fluctuations. There are two families of NPT ensembles; the isotropic, in which the volume changes but the shape of the simulation box is imposed to remain the same, and the anisotropic, in which not only the volume but also the cell vectors of the simulation box are allowed to change. For MD simulations in the NPT ensemble the thermostat is combined with a barostat to control the pressure of the system and keep it close to a desired value. A number of different barostat techniques exist for maintaining a target pressure by way of adjusting the simulation volume and many of these are counterparts to thermostats that are described above.

In the Berendsen barostat the pressure, likewise the temperature in the thermostat, is weakly coupled to a "pressure bath" and the volume of the system is rescaled at periodic intervals to keep the instantaneous pressure $P(t)$ during the MD simulation close to a requested value P_{req}. The Berendsen barostat controls directly the pressure of the modelled system via the expression:

$$\frac{dP(t)}{dt} = \frac{1}{\tau_p}(P - P_{bath}) \tag{2.19}$$

where τ_p is the barostat coupling time constant with a role similar to the thermostat relaxation constant. In the isotropic implementation of the barostat, at each MD timestep the cell volume of the system is rescaled by a factor η and the coordinates, and cell vectors, by $\eta^{1/3}$ where:

$$\eta = 1 - \beta\frac{\Delta t}{\tau_p}[P(t) - P_{req}] \tag{2.20}$$

where β is the isothermal compressibility of the system.

The Hoover barostat is an extended ensemble barostat, in which, similarly with the case of the Nosé-Hoover thermostat, the system is coupled to an imaginary "pressure bath", using an extended Hamiltonian where new degrees of freedom are introduced. It is noted that this approach was pioneered by Andersen[155] and is often termed the

Andersen barostat. When the Nosé-Hoover thermostat and barostat are used for the NPT ensemble in an MD simulation the equations of motion are expressed as follows:

$$\frac{d\vec{p}_i}{dt} = \vec{F}_i - (\xi + \chi)\vec{p}_i \tag{2.21}$$

where ξ is the thermostat friction coefficient and χ is the equivalent friction coefficient for the barostat. The Hoover barostat controls the volume fluctuations of the modelled system by using the respective friction coefficient as:

$$\frac{dV(t)}{dt} = [3\chi(t)]V(t) \tag{2.22}$$

$$\frac{d\chi(t)}{dt} = \frac{1}{\tau_p^2 k_B T}[P(t) - P_{req}] \tag{2.23}$$

where τ_p is the barostat's relaxation time.

2.3 *Ab initio* methods

An *ab initio* approach requires no parameters except for the fundamental properties of the material being studied and the forces on the atoms are obtained from their electronic degrees of freedom. The ultimate goal of this approach is to solve the time-independent non-relativistic Shrödinger equation and calculate the total energy for a particular configuration of atoms.

$$\hat{H}\Psi_k(\{\vec{r}_i\};\{\vec{R}_I\}) = E_k\Psi_k(\{\vec{r}_i\};\{\vec{R}_I\}) \tag{2.24}$$

where for a system consisting of n electrons and N nuclei the complex many-body wave-function depends on all the atomic and electronic positions $\Psi_k(\vec{r}_1, \vec{r}_2, ..., \vec{r}_n; \vec{R}_1, \vec{R}_2, ...\vec{R}_N)$ and the Hamiltonian of the system consists of a sum of five terms:

$$\begin{aligned}\hat{H} = & -\frac{1}{2}\sum_i^n \nabla_i^2 - \frac{1}{2M_I}\sum_I^N \nabla_I^2 + \sum_{i=1}^n\sum_{j>i}^n \frac{1}{|\vec{r}_i - \vec{r}_j|} \\ & - \sum_{i=1}^n\sum_{I=1}^N \frac{Z_I}{|\vec{r}_i - \vec{R}_I|} + \sum_{I=1}^N\sum_{J>I}^N \frac{Z_I Z_J}{|\vec{R}_I - \vec{R}_J|}\end{aligned} \tag{2.25}$$

Here, I and J run over the N nuclei, while i and j denote the n electrons in the system, Z is the charge and M is the mass of the respective nuclei. It is noted that the Hamiltonian operator is written in atomic units, which means that the charge and mass of an electron as well as the Planck's constant are fixed to unity ($e^2 = m = \hbar = 1$), and the Laplacian ∇^2 is given by $\nabla^2 = \frac{\partial^2}{\partial x^2} + \frac{\partial^2}{\partial y^2} + \frac{\partial^2}{\partial z^2}$. In the equation 2.25 the first two terms describe the total kinetic energy of the n electrons ($\hat{T}_{elec}$) and the N nuclei ($\hat{T}_{nuc}$) respectively. The third and fifth term represent the repulsive potential energies due to electron-electron ($\hat{V}_{elec-elec}$) and nucleus-nucleus ($\hat{V}_{nuc-nuc}$) interaction respectively, while the fourth term corresponds to the attractive electrostatic interaction between

the electrons and the nuclei ($\hat{V}_{elec-nuc}$).

The many-body wavefunction $\Psi_k(\{\vec{r}_i\};\{\vec{R}_I\})$ is a non-trivial and unknown coupling between all the particles of the system and it is too hard to deal with directly. In order to reduce the difficulty of this task approximations needs to be considered. The Born-Oppenheimer (or adiabatic) approximation treats quantum mechanically only the electronic degrees of freedom and not the ones of the nuclei.[160] Nuclei are heavier than the light electrons and, therefore, the nuclei move much slower than the electrons (by $\approx 10^3$ - 10^5 times). Hence, it can be assumed that the nuclei are clamped at fixed positions at some particular time t and the electrons are moving in the field of fixed nuclei.[161] Thus, the kinetic energy of the nuclei is zero and their potential energy is merely a constant. Consequently, the electronic Hamiltonian of the system can be rewritten in a reduced expression:

$$\hat{H}_{elec} = \hat{T}_{elec} + \hat{V}_{elec-elec} + \hat{V}_{elec-nuc} \tag{2.26}$$

The degrees of freedom of the electrons are basically decoupled from the ones of the nuclei, therefore, the electronic wavefunction Ψ_k depends parametrically on the nuclear coordinates $\{\vec{R}_I\}$ and the time-independent Schrödinger equation can be solved for the electronic system in an external potential created by the nuclei:

$$\hat{H}_{elec}\Psi_k(\{\vec{r}_i\}) = E_{elec}\Psi_k(\{\vec{r}_i\}) \tag{2.27}$$

The total energy of the system is then the sum of the E_{elec} and the constant nuclear repulsive potential energy:

$$E_{tot} = \langle\Psi_k|\hat{H}_{elec}|\Psi_k\rangle + V_{nuc-nuc} \tag{2.28}$$

The solution of equation 2.27 gives a set of eigenfunctions for the wavefunction and eigenvalues for the total energy. In order to reduce further the computational complexity only the ground state solution, Ψ_0, can be considered, which corresponds to the state with the lowest energy. For a system of n electrons and any given external potential V_{ext}, for the electron-nuclei interaction, the variational principle defines a procedure to determine the ground state wavefunction Ψ_0, the ground state energy E_0, and any other properties of interest. In other words, the ground state energy is a functional of the number of electrons and the external potential: $E_0 = E[n, V_{ext}]$.[160]

The analytical solution to equation 2.27 is obtainable only for a few very small systems (H atom, He atom and H_2^+). An exact solution for the homogeneous electron gas also exists.[162] However, the number of electrons in a real material is of the order of 10^{23} which makes the solution of the equation 2.27 a formidable task and essentially impossible to solve analytically. The main complication is that the many-body wavefunction Ψ_k depends on the $3 \times n$ spatial coordinates of the electrons $\{\vec{r}_i\}$, n being the number of electrons.

Therefore, different approaches and further approximations need to be considered in order to overcome this difficulty and obtain a numerical solution to the problem.

2.4 Density Functional Theory

Density functional theory (DFT) is an approach that exploits certain ground state properties of a many-electrons system in an external field, thus in materials modelling the Coulomb field of the nuclei. The conventional approaches use the wavefunction Ψ_k as the central quantity, as it contains the full information of the system. The prime feature of DFT is that it aims to resolve the ground state electronic density of the system $\rho_0(\vec{r})$ in order to replace the many-body wavefunction $\Psi_0(\{\vec{r}_i\})$ and, therefore, reduce the dimensionality of the problem to 3 degrees of freedom rather than $3N$ with N being the total number of electrons in the system. In that case, the electronic density is defined as the integral:

$$\rho_0(\vec{r}) = N \int \cdots \int \Psi_0^*(\vec{r_1}, \vec{r_2}, ..., \vec{r_N}) \Psi_0(\vec{r_1}, \vec{r_2}, ..., \vec{r_N}) d\vec{r}_2 ... d\vec{r}_n \tag{2.29}$$

and determines the probability of finding any of the N electrons within volume element $d\vec{r}$.

Following up the Thomas-Fermi model, in 1927, which assumes that the ground state of the system depends on the electronic density $\rho(\vec{r})$ for which the energy is minimised under the constraint of $N = \int \rho(\vec{r}) d\vec{r}$, the current formalism of DFT was rigorously established by Hohenberg, Kohn and Sham around 50 years ago.[163–165]

2.4.1 Hohenberg-Kohn theorems

The first Hohenberg-Kohn theorem[163] states that the external potential $V_{ext}(\vec{r})$ (which corresponds to the $V_{elec-nuc}$) is, to within an additive constant, a unique functional of the electronic density $\rho(\vec{r})$. If this statement is true, it demonstrates that the electronic density uniquely determines the Hamiltonian operator 2.27. This follows as the Hamiltonian is specified by the external potential and the total number of electrons, which can be computed from the density simply by integration over all space. Therefore, in principle, the electronic wavefunction $\Psi_k(\{\vec{r}_i\})$ is a unique functional of the electronic density $\Psi_k[\rho(\vec{r})]$ and, thus, all the ground state properties of the system can be obtained from its density. Consequently, the energy can be written as a functional of the electronic density $\rho(\vec{r})$ with one-to-one correspondence:

$$\begin{aligned} E[\rho(\vec{r})] &= \langle \Psi_k[\rho(\vec{r})] | \hat{H}_{elec} | \Psi_k[\rho(\vec{r})] \rangle \\ &= T_{elec}[\rho(\vec{r})] + V_{elec-elec}[\rho(\vec{r})] + V_{elec-nuc}[\rho(\vec{r})] \\ &= F[\rho(\vec{r})] + \int V_{ext}(\vec{r}) \rho(\vec{r}) d\vec{r} \end{aligned} \tag{2.30}$$

where the functional $F[\rho(\vec{r})]$ contains the functional for the kinetic energy of the electrons $T_{elec}[\rho(\vec{r})]$ and that for the potential energy due to electron-electron interaction

$V_{elec-elec}[\rho(\vec{r})]$. In addition, the interaction between the electrons and the nuclei, i.e. the external potential, is written explicitly in terms of $\rho(\vec{r})$.

However, a confirmation that a certain electronic density is the desirable ground state density $\rho_0(\vec{r})$ is needed. The second Hohenberg-Kohn theorem[163] states that the functional $F[\rho(\vec{r})]$ that delivers the ground state energy of the system, delivers the lowest energy if and only if the input density is the true ground state density.

$$E_0 = E[\rho_0(\vec{r})] \leq E[\rho(\vec{r})] \tag{2.31}$$

In other words, this means that for any trial density $\rho(\vec{r})$, which is associated with some external potential $V_{ext}(\vec{r})$, the energy obtained from the functional $F[\rho(\vec{r})]$ in the equation 2.30 represents an upper bound to the true ground state energy. The E_0 results from the minimisation of the functional $F[\rho(\vec{r})]$ at the exact ground state density $\rho_0(\vec{r})$.

Hence, the functional $F[\rho(\vec{r})]$ is the holy grail of DFT. If it was known the exact solution of the Schrödinger equation would be obtainable and, since it is a universal functional completely independent of the system under study, it applies equally efficient not only to small systems (the H atom) but also to massive molecules such as, for instance, DNA. In equation 2.30, which represents the energy functional, even though the interaction with the external potential is trivial, the explicit form of the $F[\rho(\vec{r})]$ functional (for both of its terms), unfortunately, lies completely in the dark and this corresponds to a major challenge.[160,166]

2.4.2 The Kohn-Sham scheme

To solve this problem, Kohn and Sham proposed, in 1965, the so-called single-particle approach to approximate the functionals for the electron kinetic energy and electron-electron interaction.[164] They introduced a fictitious system of N non-interacting electrons with the same density as the interacting, real, system, which can be described by a Slater determinant of N $\{\phi_i(\vec{r})\}$ single-particle orbitals. The electronic density and the kinetic energy can then be obtained from the one-particle Kohn-Sham orbitals:

$$\rho_{KS}(\vec{r}) = \sum_{i=1}^{N} |\phi_i(\vec{r})|^2 = \rho(\vec{r}) \tag{2.32}$$

$$T_{KS}[\rho(\vec{r})] = -\frac{1}{2}\sum_{i=1}^{N} \langle \phi_i | \nabla^2 | \phi_i \rangle \tag{2.33}$$

The suffix emphasises that T_{KS} is not equal to the true kinetic energy ($T_{elec-elec}[\rho(\vec{r})]$) but is that of the reference system of non-interacting electrons, which reproduce the true ground state density.

In addition, a significant component of the electron-electron interaction corresponds to the classical Coulomb interaction (or Hartree energy) and can be extracted from the respective term of the functional $F[\rho(\vec{r})]$:

$$\begin{aligned} V_{elec-elec}[\rho(\vec{r})] &= \frac{1}{2}\int\int \frac{\rho(\vec{r})\rho(\vec{r\prime})}{|\vec{r}-\vec{r\prime}|}d\vec{r}d\vec{r\prime} + E_{qm}[\rho(\vec{r})] \\ &= V_{Hartree}[\rho(\vec{r})] + E_{qm}[\rho(\vec{r})] \end{aligned} \tag{2.34}$$

where $E_{qm}[\rho(\vec{r})]$ is the non-classical (quantum mechanical) contribution to the electron-electron interaction, i.e., self-interaction correction, exchange and Coulomb correlation.

These approximations neglect all the many-body interactions included in the functional $F[\rho(\vec{r})]$. All the complexity arising from the quantum mechanical many-body interactions is then introduced into a term called the exchange-correlation energy E_{XC}, which is defined as:

$$E_{XC}[\rho(\vec{r})] = (T_{elec-elec}[\rho(\vec{r})] - T_{KS}[\rho(\vec{r})]) + (V_{elec-elec}[\rho(\vec{r})] - V_{Hartree}[\rho(\vec{r})]) \tag{2.35}$$

The exchange-correlation energy corresponds to the heart of the Kohn-Sham single-particle approximation and is the functional that contains everything that is unknown. In other words, it is simply the sum of the error made in using a non-interacting kinetic energy and the error made in treating the electron-electron interaction classically.

Hence, the total energy functional from equation 2.30 (without the nuclei-nuclei interaction) can be written based on the Kohn-Sham reformulation as:

$$E_{KS}[\rho(\vec{r})] = T_{KS}[\rho(\vec{r})] + V_{Hartree}[\rho(\vec{r})] + V_{elec-nuc}[\rho(\vec{r})] + E_{XC}[\rho(\vec{r})] \tag{2.36}$$

The question which arises is how the orbitals in the non-interacting reference system can be uniquely determined. An effective potential is defined such that the ground state density of the real interacting system is reproduced from the Kohn-Sham system. This potential is the sum of the functional derivatives of the potential energy due to electron-nuclei interaction, the Hartree energy and the exchange correlation energy with respect to the electronic density:

$$\begin{aligned} V_{KS}(\vec{r}) &= \frac{dV_{Hartree}[\rho(\vec{r})]}{d\rho(\vec{r})} + \frac{dV_{elec-nuc}[\rho(\vec{r})]}{d\rho(\vec{r})} + \frac{dE_{XC}[\rho(\vec{r})]}{d\rho(\vec{r})} \\ &= \int \frac{\rho(\vec{r\prime})}{|\vec{r}-\vec{r\prime}|}d\vec{r\prime} + V_{ext}(\vec{r}) + \frac{dE_{XC}[\rho(\vec{r})]}{d\rho(\vec{r})} \end{aligned} \tag{2.37}$$

From writing the energy functional 2.36 explicitly in terms of the density built from the single-particle orbitals $\{\phi_i(\vec{r})\}$ and applying the variational principle can be found that the orbitals, which minimise the energy, satisfy the following equation, which is like Schrödinger equation:

$$\left\{ -\frac{1}{2}\nabla^2 + V_{KS}(\vec{r}) \right\}\phi_i(\vec{r}) = \epsilon_i\phi_i(\vec{r}) \tag{2.38}$$

where $\phi_i(\vec{r})$ are the one-particle Kohn-Sham orbitals and ϵ_i are the eigenvalues of these

orbitals.

The set of the non-linear equations 2.32, 2.37 and 2.38 are the one-electron Kohn-Sham equations which describes the behaviour of non-interactive electrons in an effective local potential. The V_{KS} depends on the density, and therefore the Kohn-Sham equations have to be solved iteratively. In other words, a self-consistent solution of the equation 2.38 is required. The starting point is a generated guess of the initial electronic density which is inserted into the effective potential in order to solve the equation 2.38 and obtain the single-particle orbitals. Then, the new density is calculated from the orbitals and if the difference between this density and the density from the previous step is less than a predetermined cut off, the Kohn-Sham equations have been converged and the ground state density has been obtained, otherwise the updated density needs to be inserted back to the effective potential and the single-particle orbitals recalculated.

The single-particle orbitals $\{\phi_i(\vec{r})\}$ reproduce the electronic density of the many-body system, therefore, the Kohn-Sham scheme achieves an one-to-one correspondence of the ground state density and ground state energy of a fictitious system consisting of non-interacting fermions and the real many-body system described by the Schrödinger equation. It is important to realise that if the exact forms of the E_{XC} and V_{XC} were known, the Kohn-Sham strategy would lead to the exact ground state density via equation 2.32 and the exact ground state energy via equation 2.36. Based on this view, the Kohn-Sham DFT is an empirical methodology, as the $E_{XC}[\rho(\vec{r})]$ cannot be evaluated exactly, and further approximations needs to be considered.

2.4.3 Exchange-correlation functionals

Despite the fact that $E_{XC}[\rho(\vec{r})]$ contributes substantially less than the other terms to the total electronic energy of the system, its determination is crucial for an accurate description of the interactions in a chemically complex system.[167,168]

The simplest approximation, proposed originally by Kohn and Sham,[164] is the local density approximation (LDA) and is the basis of all approximate exchange-correlation functionals. Behind the suggestion of this model is the uniform electron gas,[162] a system in which electrons move on a positive background charge distribution such that the total ensemble is neutral. The central idea of LDA is the assumption that the E_{XC} can be expressed by the following form:

$$E_{XC}^{LDA}[\rho(\vec{r})] = \int \rho(\vec{r})\epsilon_{XC}(\rho(\vec{r}))d\vec{r} \tag{2.39}$$

where $\epsilon_{XC}(\rho(\vec{r}))$ is the exchange-correlation energy per particle of a uniform electron gas of density $\rho(\vec{r})$. This energy per particle is weighted with the probability $\rho(\vec{r})$ that there is an electron at this position. The quantity $\epsilon_{XC}(\rho(\vec{r}))$ can be further split into exchange $\epsilon_X(\rho(\vec{r}))$ and correlation $\epsilon_C(\rho(\vec{r}))$ contributions. The exchange part, ϵ_X, which represents the exchange energy of an electron in a uniform electron gas of a particular density, was originally derived by Bloch and Dirac in the late 1920's:[169]

$$\epsilon_X = -\frac{3}{4}\left(\frac{3\rho(\vec{r})}{\pi}\right)^{\frac{1}{3}} \tag{2.40}$$

but there is no explicit expression known for the correlation part ϵ_C. Nevertheless, highly accurate numerical quantum Monte Carlo calculations of the homogeneous electron gas are available in the literature.[162] The accuracy of the LDA for the exchange energy is typically within 10%, while the normally much smaller correlation energy is generally overestimated by up to a factor 2.

The LDA performs well in situations where the density $\rho(\vec{r})$ is a slowly varying function. The structure of molecules and solids is described reliably within LDA for many systems. However, for properties such as ionisation energies of atoms, dissociation energies of molecules and cohesive energies the LDA has poor performance, as it overestimates them typically by 20-30%.[170] This moderate accuracy that LDA delivers is certainly insufficient for most applications related to materials modelling. In addition, LDA can also fail in systems which are dominated by electron-electron interaction effects, like heavy fermions for example.[170]

A more advanced approximation, the so-called generalised gradient approximation (GGA), is based on more complex operators.[171] The information about the gradient of the charge density $\nabla\rho(\vec{r})$ is included in order to account for the non-homogeneity of the true electron density and move beyond LDA. Then, the exchange-correlation energy depends on both the density at each point and the first order gradient terms as:

$$E_{XC}^{GGA}[\rho(\vec{r})] = \int \rho(\vec{r})\epsilon_{XC}(\rho(\vec{r}), \nabla\rho(\vec{r}))d\vec{r} \tag{2.41}$$

Thanks to much thoughtful work, important progress has been made in deriving successful GGA functionals, with PBE[171] (which used in this thesis) and BLYP[172,173] being amongst the most popular. However, is noted that it is not always the case that these functionals with the higher approximations give more reliable results compared with LDA. Hence, the choice of the exchange-correlation functional should be based on the relevant properties that need to be calculated for the system under study.

It is well known that the standard LDA and GGA functionals have some prominent failures related to the calculation of particular properties. These are notably the tendency to provide underestimated values, by up to 40%, of the band gap of semiconductors and insulators[174] and the trouble in describing the localised states in materials in which the electrons tend to be localised and strongly interacting.[175] It is important to realise that in many systems the exchange contribution, E_X, to the energy is dominant over the correlation energy, E_C.

An interesting class of functionals, introduced by Becke,[176] are the hybrid functionals, which combine orbital-dependent Hartree-Fock with conventional GGA functionals and their general form reads:

$$E_{XC}^{hybrid} = \alpha E_X^{HF} + (1-\alpha)E_{XC}^{GGA} \tag{2.42}$$

where E_X^{HF} is the non-local exchange term from the Hartree-Fock energy, except the Kohn-Sham single-partice orbitals $\{\phi_i(\vec{r})\}$ are used instead of the Hartree-Fock orbitals and, hence this is called "exact-exchange":

$$E_X^{HF} = -\frac{1}{2}\sum_i^N \sum_j^N \int\int \frac{\phi_i^*(\vec{r})\phi_i(\vec{r\prime})\phi_j^*(\vec{r\prime})\phi_j(\vec{r})}{|\vec{r}-\vec{r\prime}|} d\vec{r}d\vec{r\prime} \tag{2.43}$$

The coefficient α determines the amount of the exact-exchange mixing. It is a parameter that cannot be assigned from first principles and so is fitted semi-empirically. Originally Becke proposed the so-called half-and-half functional:

$$E_{XC} = \frac{1}{2}E_X^{HF} + \frac{1}{2}E_{XC}^{DFT} \tag{2.44}$$

where E_{XC}^{DFT} is obtained from an explicit DFT functional (LDA or GGA). However, from later studies, it emerged that the optimum amount of exchange mixing should be reduced to $\alpha \approx 0.25$, although the precise value needs to be employed depends upon the fitting data from the system under study.[177]

The hybrid functionals achieve significant improvement over GGA functionals in the calculation of the band gaps and the description of the localised states, and successfully demonstrate the necessity to incorporate fully non-local information in order to deliver greater accuracy.

The hybrid functional used in this thesis for the relevant calculations in chapters 3 and 6 is the PBE0_TC_LRC,[178] where the exchange-correlation energy is defined as:

$$E_{XC}^{PBE0\_TC\_LRC} = \alpha E_X^{HF,TC} + alphaE_X^{PBE,LRC} + (1-\alpha)E_X^{PBE} + E_C^{PBE} \tag{2.45}$$

TC is a truncated Coulomb operator where the $\frac{1}{|\vec{r}-\vec{r\prime}|}$ term becomes zero if the distance $|\vec{r}-\vec{r\prime}|$ exceeds a pre-defined r_c cut off value. It is noted that $\alpha = 0.25$ and $r_c = 2$ are the values, for the fraction of the exact-exchange mixing and the lower integration boundary respectively, used in the calculations.

A DFT calculation using a hybrid functional is computationally expensive as the calculation of the exact-exchange scales to the N^4 of the number of basis functions used in a calculation, as can be seen in the equation 2.43. The auxiliary density matrix method (ADMM)[179] can be employed to reduce the computational cost in the calculation of the exchange integrals. This approach makes use of an auxiliary basis set with less number of basis functions than the original basis set to construct a much smaller density matrix, and thus, the density is mapped onto a much sparser Gaussian basis set, containing less diffuse and fewer primitive Gaussian functions than the one employed in the rest of the calculation. The exact-exchange can then be calculated by using these smaller in size basis set and density matrix, hence reducing the number of calculations needed and, consequently, making the hybrid DFT calculation much faster.

2.4.4 The Gaussian plane wave method

In the Kohn-Sham scheme the objective is to solve the non-linear and self-consistent one-particle equations 2.32, 2.37 and 2.38 numerically. There is a need for an accurate representation of the single-particle orbitals $\phi_i(\vec{r})$ and hence the electronic density, in order to obtain the ground state energy, which is the solution of a constrained minimisation of the Kohn-Sham energy 2.36. Therefore, the Kohn-Sham orbitals usually are described using a set of basis functions, the so-called basis set $\{\phi_a(\vec{r})\}$. The Gaussian basis sets and the plane wave basis sets are among the most popular basis sets typically used for the solution of the Kohn-Sham equations. In the first approach the basis functions are localised (or atom centred), whereas in the second approach the basis functions are delocalised (or non-atom centred), and each of them has its own advantages and disadvantages.

In the Gaussian basis sets the molecular orbitals are approximated using the linear combination of atomic orbitals (LCAO) method.[160] In this approach a set of L predefined basis functions are introduced and the Kohn-Sham orbitals are written as a linear expansion of them:

$$\phi_i(\vec{r}) = \sum_{a=1}^{L} c_{ai}\phi_a(\vec{r}) \tag{2.46}$$

where c_{ai} are the expansion coefficients of the atomic orbitals and in principle $L \to \infty$. In practice though, a finite number of basis functions is used such that to be sufficient for the accurate description of the relevant calculated properties. The type of the atomic orbitals which is usually used is a contracted Gaussian function, which is a fixed linear combination of several single (primitive) Gaussian functions:

$$\phi_a(\vec{r}) = \sum_{\nu=1}^{N_a} c_\nu \eta_\nu(\vec{r}) \tag{2.47}$$

The primitive Gaussian function (or Gaussian Type Orbital) can be either cartesian or spherical:

$$\eta_\nu(\vec{r}) = N_k x^{l_x} y^{l_y} z^{l_z} e^{-\zeta_\nu r^2} \tag{2.48}$$

$$\eta_\nu(\vec{r}) = N_k Y_l^m(\theta,\phi) r^l e^{-\zeta_\nu r^2} \tag{2.49}$$

where N_k is a normalisation factor, $l = l_x + l_y + l_z$ is the angular momentum and ζ_ν (zeta) is a parameter which controls the width of the orbital. A double-zeta (DZ) Gaussian basis set for example includes two basis functions for each atomic orbital. In order to increase the quality of the basis set, Gaussian functions of angular momentum higher than the one in the valence orbitals of each atom need to be included. These basis functions are called polarisation functions and they enhance the flexibility of atoms to form chemical bonds in any direction and hence improve calculated atomic structures.

An example of this type of basis functions is the so-called $DZVP$, which is a double-zeta with polarisation functions contracted Gaussian basis set, and is used for the DFT calculations presented in this thesis.

The density within the LCAO scheme is represented in a Gaussian basis set through the following form:

$$\begin{aligned}\rho(\vec{r}) &= \sum_{i}^{L} |\phi_i(\vec{r})|^2 \\ &= \sum_{i}^{N} \sum_{a}^{L} \sum_{b}^{L} c_{ai} c_{bi} \phi_a(\vec{r}) \phi_b(\vec{r})\end{aligned} \tag{2.50}$$

It is noted that the expansion coefficients are usually collected in the so-called density matrix with elements P^{ab}.

The Gaussian basis sets are atomically centred functions which correspond to chemical insight and they provide a compact description of the Kohn-Sham orbitals.[160,166] They enable the analytical calculation of matrix integrals which make them computationally efficient. In addition, they give the opportunity to perform all-electrons calculations. However, one of their main disadvantages is that they fail to describe the single-particle orbitals near the nuclei, where the orbitals should have a cusp, instead of being flat. Moreover, they can suffer due to the incompleteness of the basis set, which gives rise to the so-called basis set superposition error. The basis functions are non-orthogonal, have wrong asymptotic behaviour and they are atomic position dependent which make them bad candidates for calculating forces. Also, the convergence of a calculation using Gaussian basis set is not a straightforward matter but is based on systematic improvement.

In the case of plane wave basis sets it is assumed that the system is placed inside a unit cell and the basis functions are described as:

$$\phi_a(\vec{r}) = \frac{1}{\sqrt{\Omega}} e^{i\vec{G_a}\cdot\vec{r}} \tag{2.51}$$

where Ω is the volume of the cell and $\vec{G}$ are the wavevectors of the reciprocal lattice. In this approach the single-particle orbitals are expanded as:

$$\phi_i(\vec{r}) = \frac{1}{\sqrt{\Omega}} \sum_{\vec{G}} c_i(\vec{G}) e^{i\vec{G}\cdot\vec{r}} \tag{2.52}$$

Since the density is the square of the wavefunctions, in a plane-wave basis set the density $\rho(\vec{r})$ will be represented as:

$$\begin{aligned}\rho(\vec{r}) &= \frac{1}{\Omega} \sum_{i} \sum_{\vec{G},\vec{G\prime}} c_i^*(\vec{G\prime}) c_i(\vec{G}) e^{i(\vec{G}-\vec{G\prime})\cdot\vec{r}} \\ &= \frac{1}{\Omega} \sum_{\|\vec{G}\|<2G_{max}} \tilde{\rho}(\vec{G}) e^{i\vec{G}\cdot\vec{r}}\end{aligned} \tag{2.53}$$

The electronic density can expanded exactly in a plane wave basis with a cut off four times the basis set cut off. The transition from the real space grid to the reciprocal space and back is obtained by using fast Fourier transform techniques in order to determine the expansion coefficients $c_i(\vec{G})$ and hence calculate the density $\tilde{\rho}(\vec{G})$.

The plane wave basis sets are delocalised functions and due to their periodic nature correspond to a natural choice when describing periodic systems.[166] The basis functions are orthogonal and independent of the nuclei position which make the calculation of the forces a trivial issue. The fast Fourier transform applied to efficiently switch between the real and reciprocal space result in a faster calculation of the Hartree energy. The quality of the basis set is controlled from one parameter and plane waves, in principle, form a compete basis set. The convergence of a calculation using plane wave basis set is also a straightforward matter. However, a large number of basis functions is required to describe accurately the Kohn-Sham orbitals and hence the electronic density. Moreover, the plane waves represent regions of empty space with the same accuracy as a region which contains an atom, leading to unnecessary computational cost. Although in principle plane waves form a complete basis set, it is necessary to truncate the basis set in order to make a calculation feasible.

The Gaussian plane wave (GPW) method[180] combines the two types of basis sets described above and aims to exploit the advantages of both approaches. It is designed in a way such that there are two representations of the density of the system, one in a Gaussian basis set and another in a plane wave basis set, in order to use the more advantageous basis set for the various elements of the calculation.

The density matrix P^{ab} for the expansion coefficients of the Gaussian basis set is the central property needs to be determined. The density of the localised basis set is then mapped through a fast Fourier transform to an auxiliary plane wave basis set. The usage of a pseudopotential (described in the following section) to replace the core electrons of the system allows for easier mapping of the density. Then, fewer Gaussian functions are required to produce the characteristic cusp behaviour near the nuclei, and due to the smoothly varying nature of the pseudopotentials fewer plane waves are required.

Using this double representation of the electronic density the Kohn-Sham energy functional (equation 2.36) is constructed within the GPW framework as:

$$\begin{aligned} E_{KS}[\rho(\vec{r})] &= T_{KS}[\rho(\vec{r})] + V_{Hartree}[\rho(\vec{r})] + V_{elec-nuc}[\rho(\vec{r})] + E_{XC}[\rho(\vec{r})] \\ &= \sum_{ab} P^{ab} \left\langle \phi_a(\vec{r}) \right| -\frac{1}{2}\nabla \left| \phi_b(\vec{r}) \right\rangle + 2\pi\Omega \sum_{\vec{G}} \frac{\tilde{\rho}^*_{tot}(\vec{G})\tilde{\rho}_{tot}(\vec{G})}{\vec{G}^2} \\ &+ \sum_{ab} P^{ab} \langle \phi_a(\vec{r}) | V^{PP}_{loc} + V^{PP}_{nl} | \phi_b(\vec{r}) \rangle + \frac{\Omega}{N} \sum_{\vec{R}} \tilde{\rho}(\vec{R}) \epsilon_{XC}(\tilde{\rho}(\vec{R})) \end{aligned} \tag{2.54}$$

The electronic kinetic energy and the potential energy due to electron-nuclei interaction are calculated analytically using Gaussian basis functions. The external potential

is described by norm-conserving pseudopotentials with a potential separation in a local V_{loc}^{PP} and non-local part V_{nl}^{PP}. The density within a plane wave basis set is used to calculate the Hartree energy and the exchange-correlation energy. The total density in the Hartree energy expression is defined as:

$$\tilde{\rho}_{tot}(\vec{G}) = \tilde{\rho}(\vec{G}) + \sum_{k} \tilde{\rho}_k(\vec{G}) e^{-i\vec{G}\cdot\vec{R}_k} \tag{2.55}$$

and $\vec{R}$ are the wavevectors of the regular grid.

Therefore, employing a Gaussian basis set has the advantage of allowing one to use fast analytical integration schemes, developed in quantum mechanical methods, to calculate most of the Kohn-Sham matrix elements, while the use of an auxiliary plane-wave basis set gives the opportunity to use fast Fourier transform algorithms for rapid convergence of the long-range Hartree terms. Thus, the GPW approach obtains linear scaling Kohn-Sham matrix construction and, hence, significantly reduces the computational cost of DFT calculations. Consequently, this method gives the opportunity for studies of quite large systems to be performed. The GPW method is implemented in the QUICKSTEP program[180] which is within the CP2K code[181] and is used for the DFT calculations presented in this thesis.

2.4.5 Pseudopotentials

The pseudopotential method is based on the possible, in almost any system, partition of the electrons between core and valence states.[161] This is feasible, as the core orbitals change little from their atomic counterparts, they are insensitive to the chemical environment and they are not involved in the bonding. In contrast, the majority of chemically important processes in solids, like formation and breaking of the bonds, depend upon the remainder, the valence orbitals. The valence states show a highly oscillating behaviour which is acquired mainly due to Pauli exclusion principle or, in other words, due to orthogonality constraints to core orbitals.

Although the Kohn-Sham equations have been shown to be tractable when plane waves are used to expand the single-particle orbitals, an all-electron calculation, including both core and valence states, would still be computationally inefficient using a plane wave basis set. The reason is that a large number of basis functions is required to treat correctly the tightly bound core orbitals and the oscillatory nature of the valence electrons, which lead to a prohibitively expensive calculation.[182]

In the pseudopotential approximation[183–185] the core energy levels are removed and the Pauli exclusion principle is enforced via a repulsive pseudopotential that acts on a set of pseudo wavefunctions, which are describing the valence orbitals. The usage of pseudopentials eliminates in this way the core electrons from the calculation and removes the wiggles from the valence orbitals. This allows for efficient application of a plane wave expansion, as the size of the basis set is reduced, which consequently speeds up the DFT calculation. Moreover, the reduction of the number of electrons reduces

the number of degrees of freedom and relativistic effects can also be included into the effective Kohn-Sham potential.

The pseudo wavefunctions have no radial nodes within a chosen cut off distance from the nuclei, r_{cor} (core radius), which makes them much more smooth than the real wavefunctions, and thus the approach provides a smoothly varying electronic density. The real and pseudo valence wavefunctions, and hence the electronic densities, agree beyond the r_{cor}. The pseudoptential needs to be transferable, i.e., to be accurate in different environments and the approach should reproduce the necessary physical properties of the full problem.

A class of pseudopotentials called norm-conserving proposed by Hamann *et al.*[186] and is a simple procedure to extract pseudopotentials from atomic calculations. These pseudopotentials are designed in that way so the integral of the square modulus of the pseudo valence wavefunction match with that of the real wavefunction for a chosen prototype atomic configuration. Popular pseudopotentials of this type are those developed by Goedecker, Teter and Hutter (GTH).[187] They consist of a local part, which includes a long-range and a short-range term, and a non-local part, which is described with spherical Gaussian type functions. GTH pseudopentials are used in the DFT calculations presented in this thesis.

2.5 *Ab initio* Molecular Dynamics

An approach to perform *ab initio* molecular dynamics is the so-called Born-Oppenheimer molecular dynamics (BOMD). Within the adiabatic approximation the nuclei are considered as classical point particles and only the electrons are treated quantum mechanically.[160] Thus, classical mechanics is applied to move the atoms by using forces which are derived from the electronic wavefunction. The calculation of the forces is based on the Hellmann-Feynman theorem, according to which for exact eigenstates and complete basis sets the contributions from variations of the wavefunction vanish exactly. So, in the BOMD approach the wavefunction is restricted to the ground state adiabatic wavefunction at each instant of time and the nuclei move on the ground state Born-Oppenheimer potential energy surface, which is obtained by solving the time independent electronic Schrödinger equation.[161] The total energy of the system is given by the equation 2.28 and hence the forces acting on the nuclei are represented as:

$$F_I = -\left\langle \Psi_0 \left| \frac{\partial \hat{H}_{elec}}{\partial R_I} \right| \Psi_0 \right\rangle - \frac{\partial V_{nuc-nuc}}{\partial R_I} \tag{2.56}$$

which within the DFT Kohn-Sham scheme can be also written as:

$$F_I = -\int \frac{\partial V_{ext}(\vec{r})}{\partial R_I} \rho_0(\vec{r}) d\vec{r} - \frac{\partial V_{nuc-nuc}}{\partial R_I} \tag{2.57}$$

Since the forces are determined, the equations of motion for the nuclei can be represented through the Newton's second law:

$$M_I \ddot{\vec{R}}_I(t) = -\nabla_I \left[\min_{\{\phi_i\}} E_{KS}(\{\phi_i(\vec{r})\}, \{\vec{R}_I(t)\}) \right] \tag{2.58}$$

where the $E_{KS}(\{\phi_i(\vec{r})\}, \{\vec{R}_I(t)\})$ corresponds to the Kohn-Sham total energy 2.36 and can be calculated from the single-particle orbitals. It is noted that the electronic structure changes due to the resulting motion of the ions and therefore the total ground state energy needs to be recalculated. In the BOMD approach the self-consistent one-particle Kohn-Sham equations are solved at each time step.[161] Thus, the ground state energy and forces are calculated at each time step and then the trajectory of the ions is obtained through the integration of the classical equations of motion by using the same methods as in classical MD (velocity Verlet algorithm for instance). Since no electron dynamics is considered, as it is assumed that the electrons follow adiabatically the classical nuclear motion, the equations of motion can be integrated on the time scale of the nuclear dynamics by using a time step in the order of magnitude of femtoseconds.

This approach allows the proper sampling of the phase space, as the motion of the particles in configuration space is realistic, and consequently delivers the correct dynamics of the system.[161] The drawback of this approach is that the electronic structure problem needs to be solved at each time step, which makes the BOMD simulation computationally expensive. However, the development of efficient numerical algorithms[188,189] for the solution of the Kohn-Sham equations and the extrapolation of the ground state wavefunction at each time step has led to an exceptional improvement of the efficiency of the BOMD simulations, and calculations of systems containing several hundred of atoms are possible.

In this thesis the BOMD approach, as implemented in CP2K package,[181] is used for the simulations presented in chapters 3 and 4. It is worth mentioning that the BOMD simulations accompanied with the sophisticated GPW method for the DFT calculations and the ASPC method for the extrapolation of the ground state wavefunction are computationally efficient calculations within this framework. The NVT or/and NPT ensemble is used depending on the purpose of the relevant calculation, and a description of these statistical ensembles can be found in the section 2.2.5.

For the NVT simulations in chapter 4 the Nosé-Hoover chains thermostat[190] is used to control the temperature fluctuations. The standard Nosé-Hoover thermostat is desribed in section 2.2.5 and through the equations 2.17 and 2.18, where the friction coefficient ξ is used. However, its deterministic character can lead to a non-ergodic thermostat, which may result in oscillations around the target temperature. The Nosé-Hoover chains thermostat, which is an extension of the standard thermostat, solves these issues by introducing a number of fictitious equations of motion N_c (chains), which are coupled together, to control the temperature and rescale the ionic velocities according to the target temperature. Then, the temperature fluctuations are controlled through the following set of expressions:

$$\frac{d\xi_1}{dt} = \frac{1}{Q_1}\left(\sum_{I=1}^{N}\frac{\vec{p}_I^2}{M_I} - gk_BT\right) - \xi_1\xi_2$$

$$\frac{d\xi_j}{dt} = \frac{1}{Q_j}(Q_{j-1}\xi_{j-1}^2 - k_BT) - \xi_j\xi_{j+1} \tag{2.59}$$

$$\frac{d\xi_{N_c}}{dt} = \frac{1}{Q_{N_c}}(Q_{N_c-1}\xi_{N_c-1}^2 - k_BT)$$

In this scheme the friction coefficient ξ depends on a series, "chain", of N_c-1 equations and the presence of N_c chains ensures the sampling of a canonical distribution for the positions and the momenta. This thermostat is ergodic and it has been shown to be able to handle successfully even the most difficult modelled systems.[190]

The $CSVR$[191] thermostat and barostat are used for the BOMD simulations in chapter 3. This thermostat can be considered as an extension of the standard Berendsen thermostat and its scheme is derived from a modification of the standard velocity rescaling. In the velocity rescaling method the total kinetic energy E_{kin} is assumed to be equal to the average kinetic energy $\overline{E}_{kin}$ at the target temperature in order to calculate the rescaling factor with which the velocities of the particles are multiplied. Bussi *et al.*[191] proposed a different approach to determine the rescaling factor, in which the kinetic energy is not equal to its average value but a target value is desired instead, which can be delivered from the canonical equilibrium distribution of the kinetic energy. A stochastic procedure is followed in order to obtain the correct ensemble, and a smooth approach is applied, in which the rescaling process is distributed among a number of time steps.

The $CSVR$ thermostat rescales the velocities via the following expression:

$$dE_{kin} = (\overline{E}_{kin} - E_{kin})\frac{dt}{\tau} + 2\sqrt{\frac{E_{kin}\overline{E}_{kin}}{N_f}}\frac{dW}{\sqrt{\tau}} \tag{2.60}$$

where τ is the relaxation constant, which determines the time scale of the thermostat, N_f is the number of degrees of freedom and dW is the so-called Wienen noise. The first term on the right hand side of the equation corresponds to the standard Berendsen thermostat, while the second term is the additional stochastic term.[191] When the modelled system is far from the equilibrium position, the deterministic part in the equation dominates and the thermostat drives fast the system to equilibration. Since the equilibrium is reached, the thermostat samples, under the assumption of ergodicity, the proper NVT ensemble. It is noted that for $\tau = 0$ the function of the thermostat corresponds to the stochastic velocity rescaling approach. The approach described above can also be used to sample the NPT ensemble through a suitable combination of the thermostat with a barostat. In that case, not only the momenta but also the barostat velocity is rescaled with the same method.

2.6 The generation of amorphous structures

When an assembly of atoms, with a suitable composition, is cooled quickly from the molten state, a glass can be formed, and the melt-and-quench approach is the most popular method in glass simulations, in order to generate amorphous structures. In this approach a good description of the interatomic forces acting in the modelled system is used in conjunction with molecular dynamics simulations to mimic the thermal processes experienced during a quench, and so induce the amorphous state. An example of melt-and-quench used to generate one of the glass compositions studied in this thesis is illustrated in figure 2.1. A typical melt-and-quench protocol is consisted of the following parts:

1. Melt: an atomic system is heated to a high temperature to induce a liquid like state.

2. Equilibration: the system is equilibrated in this high temperature.

3. Quench: the molten system is rapidly cooled down to 300 K to create the amorphous structure. A stepwise process is usually applied, with uniform intervals of temperature decrements.

4. Equilibration and data collection: The system is allowed to equilibrate at 300 K and the statistics are collected from the molecular dynamics trajectory.

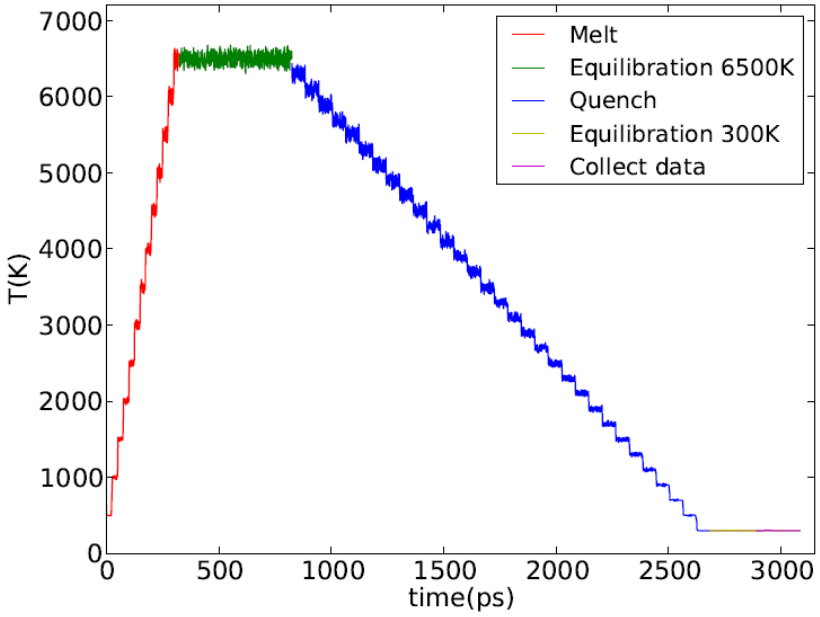

Figure 2.1: Temperature profile during the stepwise melt-and-quench approach followed to generate a $Na_2O{-}2CaO{-}4SiO_2$ glass structure of ≈ 5000 atoms, with molecular dynamics simulations. The system is heated and equilibrated at high temperature, and subsequently cooled down to 300 K, with a cooling rate of ≈ 3 K/ps. The total simulation time is about 3 ns.

Two important aspects to be assessed in glass simulations are related to the inevitable limited space and time scales to generate a glass model. Whether is limited by memory or time considerations, the number of atoms that consists the simulated system is small, in comparison to the Avogadro's number, and the modelled samples can have size of tens of nanometers. Therefore, periodic boundary conditions, as described in section 2.2.4, are used to create an infinite solid. The time-scales of the molecular dynamics simulations are limited to hundreds of nanoseconds, which are very short compared to the experimental time that is needed to form a glass. The procedure of the glass formation in the computer is another aspect, which influences the effective temperature of the simulation, and the key property is the cooling rate, which describes how the thermal energy is removed from the glass. It is noted that even for very slow rates of cooling during a computer simulation, these are still considerably faster than that used experimentally to form a glass.

The size of the models and the time-lengths of the simulations are usually constrained by the available computational resources. Even with powerful state-of-the-art machines available, combining large systems ($N > 10^5$) with slow cooling rates ($< 10^{-2}$ K/ps) still corresponds to a formidable task. However, in recent modelling studies is highlighted that the impact of size and cooling rate effects is indeed small on the accurate modelling of the structural properties of glasses.[192–194]

2.7 Potential models

The validity of the glass simulation relies on the accuracy of the potential model used for the classical molecular dynamics calculations. Two different classical interatomic potential models have been used for the molecular dynamics simulations presented in this thesis, in order to describe the forces in the modelled systems. It is noted that the choice of the force field in each chapter depends on the objective of the respective study and also on the availability of the parameters of the relevant models for the complex molar composition of the simulated glasses.

In chapters 3 and 4, a pairwise potential model is used to simulate the glass structures, which contains two terms: (i) a Coulombic potential for the long-range interactions; and (ii) a Lennard-Jones type potential for the short-range interactions.[195] Hence, the full expression for the potential model is:

$$U_{ij}(r_{ij}) = \frac{q_i q_j}{4\pi\epsilon_0 r_{ij}} + \left[\frac{\sqrt{A_i A_j}}{r_{ij}^{12}} - \frac{\sqrt{B_i B_j}}{r_{ij}^{6}}\right] \tag{2.61}$$

where q_i and q_j are the charges of the atomic species i and j respectively, ϵ_0 is the vacuum permittivity and r_{ij} is the interatomic distance. A and B are the input parameters for the Lennard-Jones function specific to the interacting species. The two A and B parameters[196] for every ion of the glass structures simulated in the relevant chapters that this force field is used are shown in Table 2.1.

Table 2.1: Parameters for the short-range potential in the 2.61 force field, which are based on the consistent valence force field with additional values suitable for the simulation of borosilicate glasses being used.

Atom	A (eV Å^{12})	B (eV Å^{6})
Ca^{+2}	18661.429	66.589
Na^{+1}	9735.806	103.097
Li^{+1}	50.055	0.000
Si^{+4}	368.510	0.000
B^{+3}	0.579	0.001
O^{-2}	42895.736	29.351

In chapters 5 and 6, the force field developed by Pedone *et al.*[197] is used for the classical molecular dynamics simulations, which is based on a rigid ionic model with partial charges, in order to handle the partial covalency of the silicate glasses. This potential model contains three terms: (i) a long-range Coulombic potential; (ii) a Morse potential for the short-range interactions; and (iii) a repulsive term, which is used to describe the repulsive contributions and is applicable only to the cases of high temperature and pressure. Hence, the full expression for the potential model reads as:

$$U_{ij}(r_{ij}) = \frac{z_i z_j e^2}{4\pi\epsilon_0 r_{ij}} + D_{ij}[\{1 - exp[-a_{ij}(r_{ij} - r_0)]\}^2 - 1] + \frac{C_{ij}}{r_{ij}^{12}} \qquad (2.62)$$

where z_i and z_j are the charges of the atomic species i and j respectively, ϵ_0 is the vacuum permittivity and r_{ij} is the interatomic distance between the two specific atomic species. D_{ij}, a_{ij} and r_0 are the input parameters for the Morse function and C_{ij} is the parameter for the repulsion term.

The four parameters[197] of the potential model for every ionic pair of the glass structures simulated in the relevant chapters that this force field is used, together with the partial charge of the alkali, alkaline-earth, silicon and oxygen ions, are listed in Table 2.2.

It is noted that this potential model has been used with some considerable success in many previous modelling studies of silicate glasses of various molar compositions.[198–202]

2.8 Modelling properties

2.8.1 Glass transition temperature

The glass transition is the reversible transition in amorphous materials from a hard and relatively brittle state into a molten state, and in silicate glasses it is related to the energy required to break and re-form covalent bonds in an random network of covalent bonds. The liquid-glass transition is associated with a discontinuous change in the structure and, hence, it does not have a sharp transition temperature. Instead,

Table 2.2: Parameters for the Morse function and the repulsion term in the 2.62 force field, which were derived by fitting both structural and mechanical properties of inorganic oxides.

Atom pair	D_{ij} (eV)	a_{ij} (Å^{-1})	r_0 (Å)	C_{ij} (eV Å^{12})
$Li^{+0.6} - O^{-1.2}$	0.001114	3.429506	2.681360	1.0
$Na^{+0.6} - O^{-1.2}$	0.023363	1.763867	3.006315	5.0
$K^{+0.6} - O^{-1.2}$	0.011612	2.062605	3.305308	5.0
$Ca^{+1.2} - O^{-1.2}$	0.030211	2.241334	2.923245	5.0
$Sr^{+1.2} - O^{-1.2}$	0.019623	1.886000	3.328330	3.0
$Ba^{+1.2} - O^{-1.2}$	0.065011	1.547596	3.393410	5.0
$Si^{+2.4} - O^{-1.2}$	0.340554	2.006700	2.100000	1.0
$O^{-1.2} - O^{-1.2}$	0.042395	1.379316	3.618701	22.0

it can be viewed as a transformation range that extends over several Kelvin or even more, and upon cooling or heating through this range, one observes a discontinuity in the temperature variation of the thermal expansion coefficient and the specific heat. However, the temperature that these effects are observed depends on the temperature variation rate and, in a more general aspect, on the preparation protocol of the glass sample. It is highlighted that the glass transition temperature is also influenced by the molar composition of the glass.

Therefore, the glass transition temperature, T_g, in silicate glasses is usually defined by convention. The idea of the calculation of the glass transition temperature for the glass compositions modelled in this thesis is based on figure 2.2. A volume−temperature, $V(T)$, plot is constructed from the results of the molecular dynamics simulations and the discontinuity in the slope is indicative for the identification and the distinguish of the liquid and solid states. Hence, two linear fittings are applied in the two (liquid/solid) states respectively, and the intersection of the two straight lines is able to provide an estimation of the glass transition temperature for the simulated glass structure.

2.8.2 Short-range order structure

A useful structural property that can be extracted from a molecular dynamics simulation is the pairwise radial distribution function (PDF), which measures how atoms organise themselves around one another, and it is proportional to the probability of finding two atoms separated by a distance $r + \Delta r$. The PDF can be expressed as:[203]

$$g_{ij}(r) = \frac{\sum_{k=1}^{M} N_j^k(r, \Delta r)}{M1/2N_i\rho_j V(r, \Delta r)} \tag{2.63}$$

where $N_j^k(r, \Delta r)$ is the number of atoms of the j^{th} species found at the instant time t_k in a spherical shell of radius r and thickness Δr, with the shell centred on an atom of the i^{th} species, $V(r, \Delta r)$ is the volume of the shell, N_i is the number of atoms of the i^{th} species and $\rho_j = \frac{N_j}{V}$ is the density of atoms of the j^{th} species. During a molecular

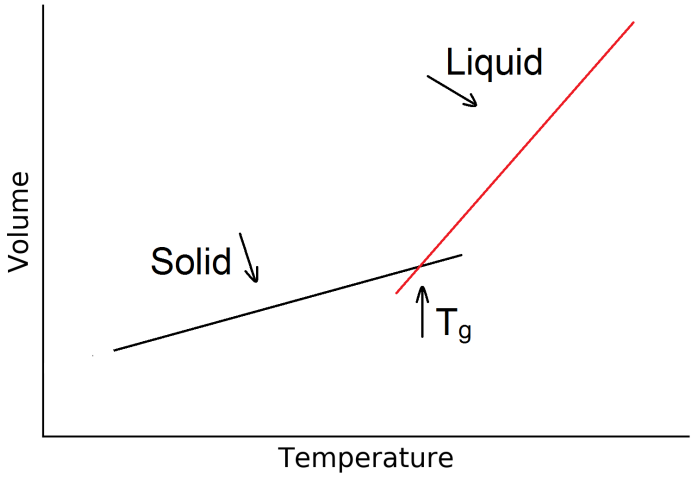

Figure 2.2: A schematic of volume−temperature diagram used for the calculation of the glass transition temperature in the simulated glass structures. The intersection between liquid and solid state corresponds to an estimation of the glass transition temperature.

dynamics run, the $N_j(r, \Delta r)$ term of the equation above is measured at M times and then is averaged, in order to calculate the relevant average interatomic distance between i^{th} and j^{th} species.

The integration of the $g_{ij}(r)$ between two positions, r_1 and r_2, provides information about the coordination number (CN) of the respective coordination shell and is obtained as:[203]

$$CN_i(r_1, r_2) = \sum_j \int_{r_1}^{r_2} 4\pi\rho_j r^2 g_{ij}(r) dr \tag{2.64}$$

It is noted that usually in modelling studies of the structure of glasses, one is interested most in the geometry of the first coordination shell of the atoms, in order to describe their local atomic structure within the glass network, and hence provide details about their local environments. Therefore, the interatomic distance and the respective coordination number, which correspond to the first peak of the $g_{ij}(r)$ are calculated from the simulation results.

2.8.3 Medium-range order structure

The amount of bridging and non-bridging oxygen atoms associated with the SiO_4 tetrahedra is an important index in the description of the simulated glass structure. The ring size distribution is a useful tool to characterise the intermediate-range order structure of the glass models, and it is defined as the number of tetrahedra involved in the smallest closed chains formed by bridging oxygen atoms and network formers in the glass network. It is noted that rings that can be decomposed into two or smaller rings usually are not counted in the distribution. Although the ring size distribution is not

obtainable experimentally for silicate glasses, the structural models in the literature are frequently discussed in terms it.[12,198,199,202]

In the simulated glass compositions studied in this thesis, the medium range order of the glass structure is characterised using the R.I.N.G.S statistics package.[204] In the calculations the ring size is described in terms of the number of network forming (Si and/or B) nodes, and hence an n-fold (n-members) ring is containing n nodes. The Guttman's shortest path criterion[205] is used to define a ring inside the glass network, and based on that, a ring corresponds to the shortest path which comes back to a given node from one of its nearest neighbours. It is noted that the calculation of the rings depends on the simulated Si−O $g(r)$, as the cut off from the first Si coordination shell is used as an input parameter.

2.8.4 Velocity autocorrelation function & Vibrational spectrum

An autocorrelation function describes the extent to which a system retains the memory of its previous values, in other words, how long it takes for the system to lose its memory. A representative example is the velocity autocorrelation function (VACF), $C_{vv}(t)$, which indicates the degree that the velocity at time t is correlated with the velocity at time 0. It is a property that can be quantified from a molecular dynamics simulation by averaging over the total number N of atoms in the modelled system:[203]

$$C_{vv}(t = \Delta t) = \frac{1}{N}\sum_{i=1}^{N}\frac{\langle \vec{v}_i(t_0) \cdot \vec{v}_i(t_0 + \Delta t)\rangle}{\langle \vec{v}_i(t_0) \cdot \vec{v}_i(t_0)\rangle} \tag{2.65}$$

where $\vec{v}_i(t_0)$ is the velocity of an atom i at an initial time t_0 and $\vec{v}_i(t_0 + \Delta t)$ is the velocity of the same atom at some later time, with Δt being the timestep used for the integration of the equations of motion in the molecular dynamics simulation. It is noted that the angle brackets in the equation above correspond to the time average.

The velocity autocorrelation function usually exhibits an initial value of 1 and at long times has a value around zero, and the time taken to lose the correlation is often called relaxation time. It is noted that the screening of the simulated trajectory needs to be for a time frame that is longer than the relaxation time, and hence sufficient data can be extracted from the simulation to calculate the correlation function and investigate the short-time dynamical behaviour of the atomic species in the modelled glass structure.

The structural and dynamical calculations from a molecular dynamics simulation can be transformed between time and frequency domains, or between normal and reciprocal space. The velocity autocorrelation function can be used, at low temperature, as a tool to investigate the vibrational properties of the simulated glass structure, and compare them to experimental measurements. The vibrational spectrum of the glass can be calculated from the Fourier transform of the velocity autocorrelation function as:[206,207]

$$F(\omega) = \frac{1}{\sqrt{2\pi}}\int_{-\infty}^{\infty} C_{vv}(t)e^{i\omega t}dt \tag{2.66}$$

Hence, the vibrational density of states (VDOS) is: $\Phi(\omega) = F^2(\omega)$. It is noted that usually the frequencies of the peaks in the VDOS of the simulated glass structures are obtained from the real part of the Fourier transform in the equation 2.66.

2.8.5 Ionic diffusion

Molecular dynamics allows one to follow the time evolution of the system, and hence the method is naturally suited to following dynamical processes in condensed phases. The output collected from the simulation contains all the information needed to describe the atomic processes underlying the transport of the mobile species in the glass composition. The main challenge to face in order to apply standard MD approaches to model ion migration in silicate glasses has to do with the infrequent nature of the hopping events that compose the diffusive process.[38,39,194] It is noted that transport properties, such as diffusion coefficients and activation energies for diffusion, usually are obtained experimentally by tracer diffusivity measurements in temperatures between 450 - 750 K, with annealing times varying from 30 minutes, at the higher temperatures, to 90 days, at the lower temperatures. However, in a computer simulation, the phase space can be sampled for annealing time ranging from hundreds of picoseconds to hundreds of nanoseconds, depending on the available computational resources. Therefore, the molecular dynamics simulations are performed at higher temperatures than that of 300 K, in order to accelerate the statistical sampling, and hence observe a considerable ionic diffusion during the relatively short simulation time. Nevertheless, the selected temperatures to model the mobility of the ions in the glass structure are below the glass transition temperature, and thus no significant structural changes are anticipated to occur at these conditions, ensuring that the ions still diffuse in an essentially silicate network, whose average configuration matches with the corresponding at 300 K configuration. Consequently, the comparison between the experimental measurements and the computational derived data is not straightforward. It is noted that computational modelling of ionic diffusion is used to analyse the trends in the behaviour of the ions, and hence characterise qualitatively their mobility within the glass network.

The mean squared displacement (MSD) contains information about the atomic diffusivity of the individual species in the glass structure, and it is a measurable quantity which relates directly to the underlying motion of the molecules. The MSD measures the average distance that an atom of the j^{th} species travels in the time t, and it is defined as:[198]

$$MSD(t) = \frac{1}{N_j} \sum_{i=1}^{N_j} \left\langle |\vec{r}_i(t) - \vec{r}_i(t=0)|^2 \right\rangle \tag{2.67}$$

where $\vec{r}_i(t) - \vec{r}_i(t=0)$ is the vector distance travelled by an atom i during some time intervals of length t, and the squared magnitude of this vector is averaged over many such time intervals and over all the atoms of the j^{th} species in the simulated glass structure.

The self-diffusion coefficient, D_j, for specific particles of type j, is one of the most important properties used to study the dynamics in silicate glasses, which can be calculated from the mean squared displacement via the Einstein relation:[198]

$$D_j = \frac{1}{6} \lim_{t \to \infty} \frac{d}{dt} MSD(t) \tag{2.68}$$

Hence, the self-diffusion coefficient is obtained from the slope of the linear regime of the MSD plotted as function of the simulation time.[199,207,208] It is noted that the Green-Kubo integral of the velocity autocorrelation function is another approach to estimate the self-diffusion coefficient of an ion in the simulated glass structure.[34]

The diffusion coefficients are found to vary considerably with temperature, and this variation can be approximated in terms of an Arrhenius behaviour, through the equation:[198]

$$lnD(T) = lnD_0 - \frac{E_a}{k_B T} \tag{2.69}$$

where T is the temperature, D_0 is the pre-exponential factor, k_B is the Boltzmann's constant and E_a is the activation energy for diffusion. Therefore, based on the calculation of diffusion coefficients at several temperatures an Arrhenius type plot can be constructed, and hence the activation energy barrier that an ion must overcome to migrate between two sites, is obtained by linear regression between the natural logarithm of diffusion coefficient and the reciprocal temperature.[207,208]

2.8.6 Excited state & Luminescence

The excited state of the simulated glass structures was modelled, using ground-state density functional theory methods, by calculating the system in a triplet state, with promotion of an electron from the top of the valence band into the bottom of the conduction band. In that case, the lowest energy excited state of the modelled system is determined by restricting its electronic structure to the lowest energy triplet state. The configuration of the triplet state was then found by minimising the total energy of the system with respect to the atomic positions. It is noted that this approach has been followed in other computational modelling studies of relevant structures,[209–211] as it is known that after singlet excitation, excitons quickly convert into the lower triplet state.

The ΔSCF (Delta-SCF) method[212,213] is used in order to calculate the excitation and luminescence energies in the glass models. This approximation corresponds to a density functional method, closely resembling standard DFT, with the only difference being that in ΔSCF approach one or more electrons are placed in higher lying Kohn-Sham orbitals,[214,215] instead of placing all electrons in the lowest possible orbitals, as one does when calculating the ground state energy within standard DFT based methods. Hence, the ΔSCF method corresponds to the difference of two self-consistent field calculations by subtracting the energy between two states of the same geometry. Thus,

the excitation energy is calculated as the difference between the total energies of the glass structure in the ground singlet and the lowest triplet state at the geometry of the ground singlet state. Subsequently, the luminescence corresponds to the vertical triplet-singlet transition at the geometrical configuration of the relaxed triplet state. The luminescence energy is calculated as the difference between the total energy of the fully relaxed triplet state and the total energy of the ground singlet state at the triplet geometric structure.

3 Glass transition temperature, structure and electronic properties of mixed alkali borosilicate glass

3.1 Introduction

Alkali borosilicate glasses of various compositions have a multitude of practically important applications, ranging from utensils in the kitchen to the vitrification of high level nuclear wastes, which is accounted for by their simplicity of synthesis, good chemical durability, low melting temperatures, high chemical stability, low thermal expansion, mechanical strength, good insulation properties, and a number of other technologically and technically important aspects.[85,103,216] These properties are usually determined by the structural features of the glass, specifically the polymerisation of the silicate network and the boron local environments, which in turn are strongly correlated to the composition of the glass sample.

One of the most complex aspects related to the structure of borosilicate glasses is the multiple coordination environments possible for boron within the glass network, as both 3- and 4-coordinated B atoms may be present simultaneously, in the form of BO_3 triangles and BO_4 tetrahedra respectively.[86] The ratio of these two local geometries is mainly related to the temperature and the glass composition. High temperatures, which correspond to a molten structure, tend to stabilise the BO_3 formation as compared to the tetrahedral geometry. At room temperature, which corresponds to the glass structure at 300 K, this ratio (3- to 4- coordinated) depends on the specific value of the melting temperature, the cooling rate from the melt (in other words, the degree to which the high temperature structure has been "frozen in"), the melting pressure and the molar composition of the glass.[217–219] In particular, it has been observed that increasing the cooling rate leads to a decrease to the proportion of the 4-coordinated B, whereas high pressures cause an increase of the BO_4 tetrahedra within the glass structure.[218,219]

A number of structural models have been proposed based on experimental data, aimed at understanding the change in the fraction of 3- and 4- coordinated boron in alkali borosilicate glasses.[220–222] However, these models are inadequate for the description of the data from glass compositions with high concentration of alkali oxides. Dell

et al. used ^{11}B solid-state NMR and Raman spectroscopy to investigate extensively the structural properties of alkali borosilicate glasses, in order to extend the domain of applicability of the existing structural models.[223] Based on their experimental measurements, they developed and established a structural model, which hereafter is referred to as YBD (Yun-Bray-Dell), able to describe the modification of the glass structure when alkali cations are added to the system and the mechanism of creation of non-bridging oxygen atoms within the glass network. Two parameters are introduced, $K = \frac{SiO_2}{B_2O_3}$ and $R = \frac{A_2O}{B_2O_3}$, which determine the relevant structural features of the glass. It is noted that increasing K and/or R is equivalent to increasing SiO_2 and/or the alkali oxide content respectively, or decreasing the boron oxide content in each ratio.

In the YBD model, four distinct regions are defined to predict the proportion of 3- and 4-coordinated boron, as well as the fraction of the bridging oxygen atoms, as a function of the glass composition. The first region is for compositions with $R < 0.5$, in which the additional oxygen from the alkali oxide (A_2O) enters the borate network exclusively, enhancing the formation of BO_4 tetrahedra. Thus, the BO_3 units are transformed to BO_4 with the alkali cations acting as charge compensators. The second regime is for $0.5 \leq R \leq R_0$, where $R_0 = \frac{1}{2} + \frac{1}{16}K$ is the threshold composition, in which the extra oxygen continues to form 4-coordinated B atoms, which are connected to SiO_4 tetrahedra, and open reedmergnenite-like structures are formed on intermediate length scales. The third section is for $R_0 < R \leq R_1$, where $R_1 = \frac{1}{2} + \frac{1}{4}K$, in which the additional alkali cations are assumed to enter the polymerised silicate glass network starting to act as network modifiers, and hence, forming non-bridging oxygens. Thus, no further increase in the fraction of the 4-coordinated boron atoms occurs. The final, fourth region, is for $R_1 < R \leq R_2$, where $R_2 = 2 + K$, and corresponds to the upper limit of the model, in which the added A_2O is presumed to be proportionally shared between the silicate and borate network, leading to a decrease in the number of 4-coordinated B within the glass structure.

Manara *et al.* assigned certain bands of the Raman spectra measured for sodium borosilicate glasses at different temperatures to medium-range order structures, and they proposed a revision of the YBD model.[224,225] In their studies, the peaks around 580 cm^{-1} and 630 cm^{-1}, which are two of the main features in the 550−850 cm^{-1} frequency range, were designated to breathing models of borosilicate reedmergnenite-like and danburite-like rings respectively. It is noted that a reedmergnenite-like ring is made up from one BO_4 tetrahedron and two SiO_4 tetrahedra, while a danburite-like ring includes two BO_4 and two SiO_4 tetrahedra. In practise, this revision of the YBD model modifies the threshold composition R_0 for the second region to $R_0 = \frac{1}{2} + \frac{1}{2N}K$, where N ranges between 5 and 6. Recently, Roderick *et al.* reported also a detailed analysis about the variations in density and boron coordination environments observed for a series of alkali borosilicate glasses with increasing R.[226]

As described in section 1.3, mixed alkali borosilicate glasses have long been preferred for the immobilisation of high level nuclear waste due to the fact that these compositions meet many requirements for an effective nuclear waste-form. However, in order

to acquire the desirable glass properties related to the immobilisation process, an understanding of the chain which connects composition−structure−property relationships is crucial. While there have been many modelling studies of glasses in recent years, only a handful have concerned alkali borosilicate glass compositions,[227–229] which, although these are limited to small compositional ranges, can demonstrate the ability of molecular dynamics simulations to reproduce the changes observed in the glass structure with composition. It is noted that the main reason that the modelling of mixed alkali borosilicate glasses has been rather limited is related to the different coordination environments of B atoms within the glass network, which makes the development of a reliable interatomic potential an arduous task.

In this thesis, a combination of classical and *ab initio* MD simulations, together with static electronic structure calculations, are presented for lithium sodium borosilicate glasses with pre-defined compositions, which are of importance of IHI-corporation nuclear waste vitrification program. In the first part of the analysis a method to calculate the glass transition temperature is presented and evaluated through the comparison with the experimental data. In the second part of the analysis a systematic investigation into the structural and electronic properties of four glass compositions is presented by fixing the concentration of Li_2O and Na_2O oxides and varying the $\frac{SiO_2}{B_2O_3}$ content of the glass sample.

3.2 Computational details

In the first part of the simulations presented in this chapter, four glass compositions were modelled using periodic boundary conditions in order to investigate the effect of the addition of several oxides with specific concentration on the calculation of the glass transition temperature of the glass sample. The starting configuration was a pure SiO_2 glass, which then was doped, initially, with 23.8 % mol Li_2O and, afterwards, with 5.8 % mol Na_2O. In the final stage, 27.4 % mol B_2O_3 was introduced in the glass composition, resulting in the mixed alkali borosilicate glass that corresponds to a simplified nuclear waste glass of interest for the vitrification facility of IHI at Rokkasho in Japan. The total number of atoms in the pure silicate glass and in the models with the alkali oxides is 1536, whereas in the simulated structure that the boron oxide was added is 1816. The atoms were placed randomly in a cubic simulation box with imposed constraints to avoid un-physically small interatomic distances, and the cell size was calculated from the experimental density provided by IHI for each structure. The various glass compositions in terms of the oxides combination, the number of atoms of each species and the density for every simulated structure are shown in Table 3.1. It is noted that the four modelled systems thereafter referred as S, SL, SLN and SLNB, from the SiO_2 to the lithium sodium borosilicate glass composition respectively.

The pairwise potential model 2.61 described in section 2.7 was employed for the calculations. The Coulomb interactions were calculated using the Ewald summation method[151] with a precision of 10^{-6}. The cut off for the short-range interactions was

Table 3.1: The combination of the four different oxides in the modelled systems in terms of molar compositions (in %), the number of atoms of each type and the experimental density (in g/cm^3). The total number of atoms in the first three models is 1536, while in the mixed alkali borosilicate glass is 1816.

System	SiO_2	Li_2O	Na_2O	B_2O_3	Si	O	Li	Na	B	ρ
S	100	0	0	0	512	1024	0	0	0	2.20
SL	76.2	23.8	0	0	390	902	244	0	0	2.28
SLN	70.4	23.8	5.8	0	360	872	244	60	0	2.47
SLNB	52.4	13.4	6.8	27.4	268	1060	138	70	280	–

set to 10 Å. The DL_POLY classic package[230] was used for the molecular dynamics simulations and the velocity Verlet algorithm was applied for the integration of the equations of motion with a timestep of 1 fs.

The glass structures were generated using a melt-and-quench approach, and the NPT ensemble was applied to allow the volume of the simulation box to change. The Nosé-Hoover thermostat and barostat have been used to control the temperature and pressure fluctuations with relaxation constants 0.1 and 0.5 ps respectively. The initial configuration was heated up gradually in steps of 100 K with a 60 ps MD run at each temperature. The molten structure was equilibrated at 4000 K using first the NPT and then the NVE ensembles with 600 ps MD run in total, in order to ensure that the structure was well equilibrated at this temperature. The system was subsequently cooled, using a uniform stepwise process, with temperature decrements of -5 K and 60 ps NPT runs at each temperature, until the temperature of the system reached 300 K. It is noted that during the first 2000 steps of each quench run the velocity was scaled every timestep in order to equilibrate the structure at the specific temperature. A further 200 ps NPT run was carried out at 300 K, followed by a 200 ps NVE run in order to equilibrate the structure. The quench scheme took place in 740 steps and corresponds to a cooling rate of $\approx$ 0.1 K/ps, while the total simulation time was $\approx$ 50 ns.

It is noted that the melt-and-quench approach is the standard method to form a glass, which, however, can add some noise in the calculation of the glass transition temperature. Therefore, for every chemical composition, the configuration obtained from the melt-and-quench was reheated from 300 K up to 1500 K with a heating rate of $\approx$ 0.1 K/ps and the $V(T)$ plot is constructed in order to calculate the glass transition temperature with the method described in section 2.8.1. This procedure was repeated five times and the T_g was averaged over these attempts in order to obtain a virtually independent calculation of the glass transition temperature for every modelled system. The S glass composition was cooled down from the melt with faster cooling rates, specifically with 1, 5, 10, 15, 20, 25 K/ps, in order to investigate how the simulated cooling rate can influence the calculation of both the glass transition temperature and the density of the glass structure.

Based on the SLNB composition, in the second part of the simulations presented in this chapter, a series of four lithium sodium borosilicate glasses, of the composition $(SiO_2)_{52.4+27.4-x} \cdot (Li_2O)_{13.4} \cdot (Na_2O)_{6.8} \cdot (B_2O_3)_x$, with $x = 25, 20, 15, 10$, was modelled using periodic boundary conditions. The modelled systems based on the four x values of the boron oxide concentration hereafter referred as SLNB25, SLNB20, SLNB15 and SLNB10 respectively. The starting configurations were generated by placing atoms randomly in a cubic simulation box with imposed constraints to avoid un-physically close separations. The total number of atoms in the SLNB25 glass is 224 (35 Si, 18 Li, 8 Na, 32 B and 131 O), in the SLNB20 glass is 218 (38 Si, 18 Li, 8 Na, 26 B and 128 O), in the SLNB15 glass is 210 (42 Si, 18 Li, 8 Na, 18 B and 124 O), and in the SLNB10 glass is 204 (45 Si, 18 Li, 8 Na, 12 B and 121 O).

Classical MD simulations with the modelling conditions and the melt-and-quench scheme described above were performed in order to generate the amorphous structures. For each composition, the final glass structure at 300 K was then used as an input configuration for two consecutive *ab initio* BOMD simulations. The structure was equilibrated with a 10 ps NPT BOMD run, and the $CSVR$ thermostat and barostat were applied with relaxation constants 0.1 and 1.0 ps respectively. A subsequent BOMD run of 10 ps, with the NVT ensemble and the $CSVR$ thermostat, was carried out, as a production run, to sample the trajectories every 2 steps and collect the data for the structural analysis. The electronic structure was described by the DFT Kohn-Sham formulation,[164] as implemented in the CP2K code,[181] using the GGA with the PBE exchange-correlation functionals,[171] and in the calculations, all the atomic species were represented using a double$-\zeta$ valence polarised ($DZVP$) Gaussian basis set[231] in conjunction with the GTH pseudopotential.[187] The plane-wave cut off was set to 700 Ry and the MD timestep was 1 fs. The density of the simulated glass compositions was estimated by performing a cell optimisation using variable cell BOMD with a timestep of 1 fs and a convergence threshold of 0.1 kbar for the components of the stress tensor. The electronic structure of the glass models was calculated with a fixed volume geometry optimisation of the relaxed structure obtained from the variable cell calculations, and the Broyden-Fletcher-Goldfarb-Shanno (BFGS) optimiser was applied to minimise the forces on atoms to within 40 pN (2.5 x 10^{-2}eV Å^{-1}). The hybrid functional PBE0_TC_LRC, described in section 2.4.3, was also used for separate geometry optimisations of the glass structures, as the inclusion of the Hartree-Fock exchange will provide a more accurate calculation of the band gap.

3.3 Results of calculations & Discussion

3.3.1 Glass transition temperature

The glass transition temperature was measured for the simulated glass compositions in order to understand how the inclusion of the two alkali oxides (Li_2O and Na_2O) and the second network former (B_2O_3) will affect the glass transition of the pure SiO_2

glass sample. The volume−temperature diagram for the SLN glass composition and the method applied to calculate the glass transition temperature, are shown in figure 3.1. From linear regression on the $V(T)$ data in the glass and melt state respectively, the glass transition temperature was estimated from the intersection of the two straight lines. It is noted that similar approach was followed to calculate the glass transition temperature for every modelled system.

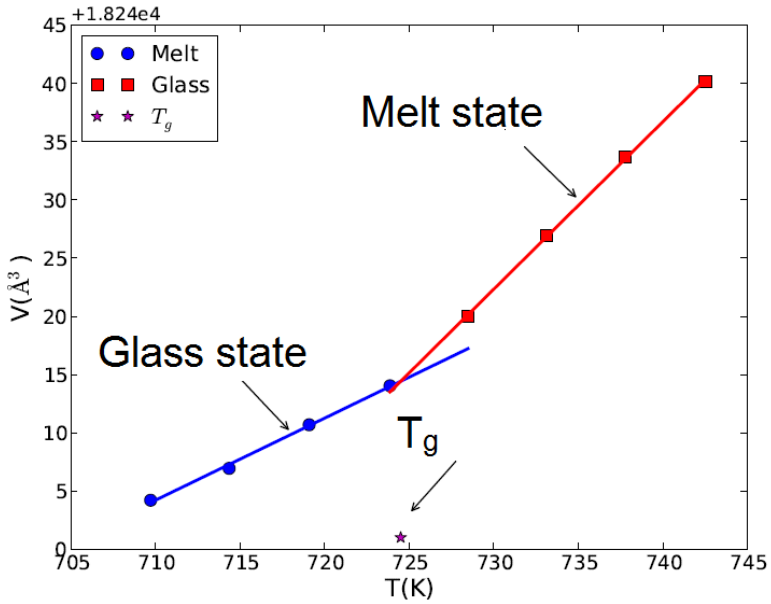

Figure 3.1: Volume−temperature plot constructed for the lithium sodium silicate glass model (SLN composition). The glass structure retrieved from the melt-and-quench was heated up to 1500 K with a heating rate of ≈ 0.1 K/ps. The change of the slope is an indication of the transition from the solid to the liquid state, and hence the glass transition temperature is estimated from the intersection between the glass and melt state.

The results (average values) from the calculation of the glass transition temperature along with a measure of variability (standard deviations) for every simulated composition are reported in Table 3.2, together with the comparison to the relevant experimental measurements for the same molar compositions by IHI. As it was expected, the additives into the pure SiO_2 glass bring down the glass transition temperature of the glass sample. The presence of more than one alkali oxides in the glass composition leads to a larger decrease of the glass transition temperature, while the subsequent addition of the boron oxide results in a further reduction of the calculated temperature. It is noted that the glass transition temperatures predicted in the simulations presented in this chapter are over-estimated for each modelled composition. Nevertheless, the computer simulated values are in very good quantitative agreement with the experimental measurements from the IHI glass structures, which corresponds to a sufficient validation for the method followed to estimate the glass transition temperature in this thesis.

The density of the simulated glass compositions was also calculated based on the final volume at 300 K, which corresponds to the outcome equilibrated structure from

Table 3.2: Calculated glass transition temperature (mean value and standard error of the mean) for the four simulated glass compositions and comparison with the experimental data provided by IHI.

Composition	T_g (K) from MD	T_g (K) from IHI
S	1973 ± 3	1942
SL	744 ± 4	717
SLN	725 ± 4	702
SLNB	569 ± 3	–

the melt-and-quench protocol followed to generate the glass models, and the results are shown in Table 3.3. It is noted that, for every chemical composition, the simulated density is under-estimated by ≈ 3 % with respect to the experimental measurement from the IHI glass structures. However, it can be observed that there is the same systematic trend in the variation of the experimental and calculated densities from the S to SLN composition. The cause of the difference between the calculated and the experimental values probably lies in the accuracy of the interatomic potential used to generate the amorphous structures in this study.

Table 3.3: Calculated density for the four simulated glass compositions and comparison with the experimental data provided by IHI.

Composition	ρ (g/cm^3) from MD	ρ (g/cm^3) from IHI
S	2.15	2.20
SL	2.22	2.28
SLN	2.41	2.47
SLNB	2.42	–

In order to investigate the impact of the cooling rate on the calculation of the glass transition temperature and the amorphous density, test simulations with different cooling rates were performed for the pure SiO_2 composition, and the results are presented in Table 3.4. Six faster cooling rates, which varied from 1 to 25 K/ps, were applied for the quench of the structure starting from the same equilibrated configuration at the melt. It can be observed that the glass transition temperature decreases as the quenching from the melt becomes slower, whereas the density of the glass structure decreases as the cooling is more rapid. Consequently, this behaviour indicates a dependence of the calculated values for the glass transition temperature and the glass density on the simulated cooling rate. Such kind of observations are in agreement with previous computer simulation study reported by Vollmayr, Kob and Binder,[192] in which their analysis reveals that the glass properties show a relatively small, but nevertheless noticeable dependence on the cooling rate with which the glass was generated.

Table 3.4: Calculated glass transition temperature and density for the pure SiO_2 glass using six different cooling rates for the quench procedure starting from the same molten equilibrated structure. The experimental values of the glass transition temperature and glass density for this composition are 1942 K and 2.2 g/cm^3 respectively.

Cooling rate (K/ps)	T_g (K)	ρ (g/cm^3)
25	2327	2.01
20	2306	2.03
15	2217	2.06
10	2201	2.07
5	2175	2.10
1	2121	2.12

3.3.2 Pairwise radial distribution functions & coordination numbers

The local atomic structure of the individual components within the four simulated compositions was investigated through the pairwise radial distribution functions, g(r). The first peak of the g(r) gives information about the first coordination shell of the atomic species in the glass models. Si atoms are the main network formers in the continuous random network of the silicate glasses,[20] and their local environment in the simulated glasses were analysed though the g_{Si-O}(r), shown in figure 3.2 for every composition. In all 4 simulated glass configurations Si was found to be $\approx$ 94% 4-fold and $\approx$ 6% 5-fold coordinated to oxygen atoms with an average Si−O interatomic distance of 1.62 Å in the SLNB10 and 1.64 Å in the SLNB15, SLNB20 and SLNB25 compositions. The typical measurements from the literature for the Si−O bond length are 1.58−1.64 Å for a broad range of compositions,[12,232] while in borosilicate glasses this distance was measured experimentally[233] as 1.60 Å and with classical MD simulations[234] 1.58 Å.

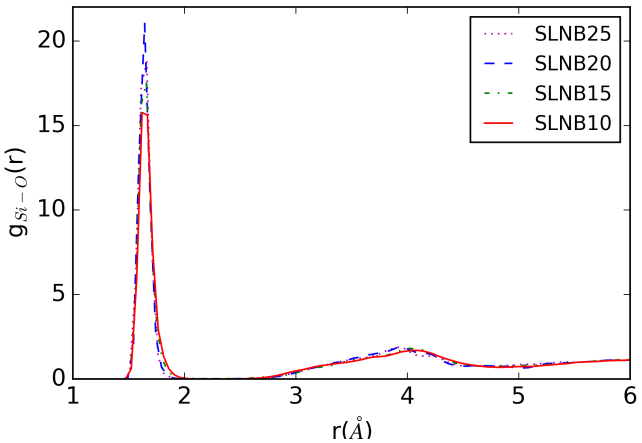

Figure 3.2: Pairwise radial distribution functions of the silicon−oxygen interatomic distances in the four simulated lithium sodium borosilicate glasses. The Si−O bond length was calculated 1.62 Å in the SLNB10 composition and 1.64 Å in the rest three glass models, while the average coordination number is 4 in every simulated glass structure.

The boron atoms have also the role of the network formers in the polymerised network of the borosilicate glasses. The local environment around B was analysed through the pairwise radial distribution functions, $g_{B-O}(r)$, shown in figure 3.3 for each simulated composition. The average B−O interatomic distance was measured 1.38 Å, 1.42 Å, 1.39 Å and 1.41 Å in the SLNB10, SLNB15, SLNB20 and SLNB25 glass models respectively. The average oxygen coordination numbers were found to be 3.33, 3.26, 3.31 and 3.23 for the SLNB10, SLNB15, SLNB20 and SLNB25 simulated glasses respectively. It was observed that in every composition the calculated coordination number is ≈ 3.3, indicating 3-fold coordination environment for the B atoms within the glass structures. The B−O bond length was measured experimentally to be 1.38 Å and 1.47 Å for 3- and 4-coordinated B atoms respectively.[235] A previous modelling study reported an average interatomic distance of 1.41 Å, while the corresponding oxygen coordination number was estimated 3.5, in lithium sodium borosilicate glasses of similar molar concentrations.[234]

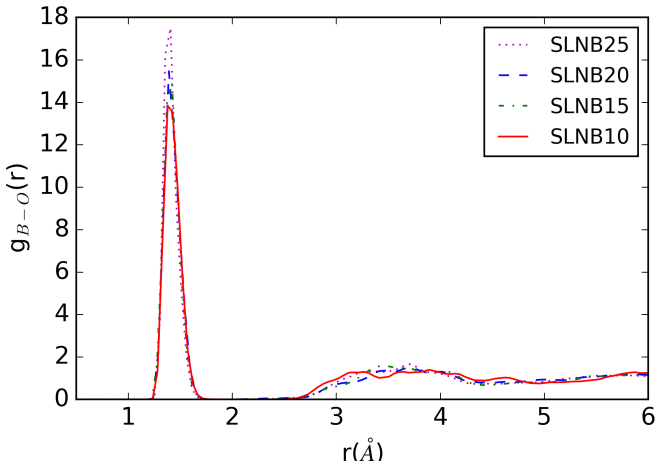

Figure 3.3: Pairwise radial distribution functions of the boron−oxygen interatomic distances in the four simulated lithium sodium borosilicate glasses. The B−O bond length was calculated 1.41 Å in SLNB25, 1.39 Å in SLNB20, 1.42 Å in SLNB15 and 1.38 Å in SLNB10, while the average oxygen coordination number was ≈ 3.3 in every simulated composition.

The average interatomic distances between silicon and boron atoms were calculated in the simulated glass structures from the pairwise radial distribution functions, $g_{B-Si}(r)$, shown in figure 3.4 for each composition. The B−Si distances were measured as 2.84 Å, 2.86 Å and 2.87 Å in SLNB25, SLNB20 and SLNB15 glass models respectively, whereas the relevant distance in SLNB10 composition was calculated as 2.69 Å. It was observed that within the polymerised borosilicate network of the simulated glass structures, B and Si are able to approach closer to each other in the SLNB10 composition in comparison to the other three glasses.

The local atomic structure of the two alkali ions was examined in the simulated glass structures through the pairwise radial distribution functions, $g_{Li-O}(r)$, shown in figure 3.5, and $g_{Na-O}(r)$, shown in figure 3.6 for Li and Na cations respectively.

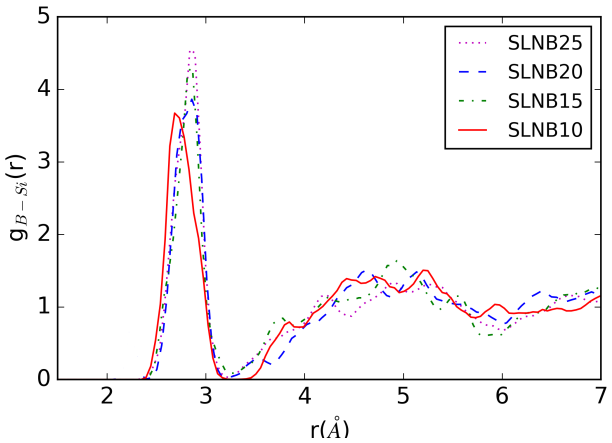

Figure 3.4: Pairwise radial distribution functions of the boron−silicon interatomic distances in the four simulated lithium sodium borosilicate glasses. The B−Si bond length was calculated 2.69 Å in SLNB10, 2.87 Å in SLNB15, 2.86 Å in SLNB20, and 2.84 Å in SLNB25. B and Si atoms in SLNB10 glass model are in closer distances than that in the rest three simulated compositions.

The average oxygen bond lengths for the lithium ions were calculated as 1.91 Å in SLNB10 and SLNB25 glass models, 1.90 Å and 1.95 Å in SLNB15 and SLNB20 compositions respectively. The average oxygen coordination number around Li atoms was found to be 4 in SLNB10 glass and ≈ 3.6 in the other three simulated compositions, indicating a 4-fold coordination geometry for lithium within the glass structures. Experimental and modelling studies in lithium silicate glasses reported 4-coordinated Li atoms and an Li−O interatomic distance of 1.96 - 2.10 Å,[7,198] while a previous modelling study in lithium sodium borosilicate glasses reported an average Li−O interatomic distance of 2.07 Å, with an average oxygen coordination number 3.5.[234]

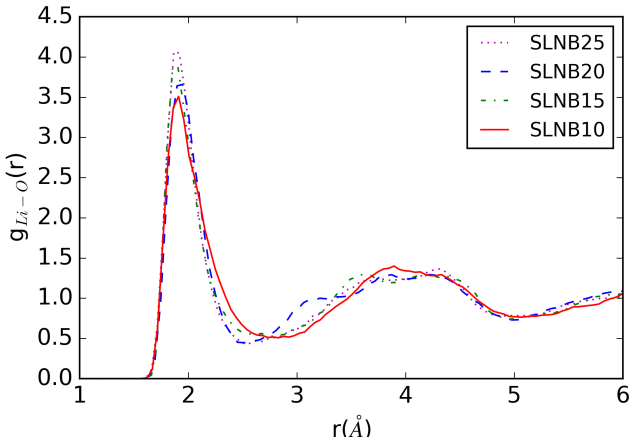

Figure 3.5: Pairwise radial distribution functions of the lithium−oxygen interatomic distances in the four simulated lithium sodium borosilicate glasses. The Li−O bond length was measured 1.91 Å in SLNB25 and SLNB10 compositions, 1.95 Å in SLNB20 and 1.90 Å in SLNB15, while the average oxygen coordination number was calculated ≈ 4 in every simulated glass structure.

For the sodium cations the average Na−O bond length was computed as 2.38 Å in SLNB25 composition, 2.34 Å in SLNB15, and 2.35 Å in SLNB10 and SLNB20 glass models. The average oxygen coordination numbers around Na cations were found to be 6.2 in SLNB10 and SLNB15 compositions, 6.1 in SLNB20, and 5.5 in SLNB25 showing that sodium ions are mainly 6-fold coordinated to oxygen atoms within the glass structures. The Na−O interatomic distance was calculated in borosilicate glasses as 2.2 - 2.55 Å experimentally[233] and 2.82 Å in a previous modelling study[234] of similar molar compositions. In previous modelling studies, an average oxygen coordination number of 6 was reported for Na cations in sodium silicate glasses, while an average oxygen coordination number of 8 was reported in lithium sodium borosilicate glasses.[198,232,234]

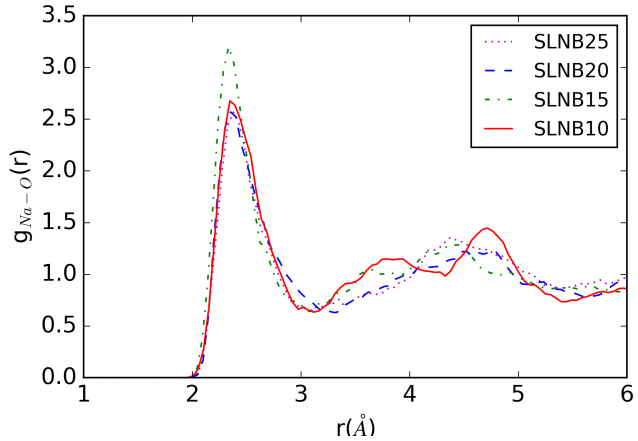

Figure 3.6: Pairwise radial distribution functions of the sodium−oxygen interatomic distances in the four simulated lithium sodium borosilicate glasses. The Na−O bond length was measured 2.38 Å in SLNB25, 2.35 Å in SLNB20 and SLNB10, and 2.34 Å in SLNB15, while the average oxygen coordination number was calculated ≈ 6 in every glass model.

The average oxygen interatomic distances and the corresponding average oxygen coordination numbers for Si, B, Li and Na atoms in the four simulated lithium sodium borosilicate glass structures are summarised in Tables 3.5 and 3.6 respectively.

Table 3.5: Average oxygen interatomic distances for silicon, boron, lithium and sodium atoms in the SLNB25, SLNB20, SLNB15 and SLNB10 simulated glass structures. The bond lengths correspond to the first peak position of the respective pairwise radial distribution functions for each species.

Composition	Si−O (Å)	B−O (Å)	Li− (Å)	Na−O (Å)
SLNB25	1.64	1.41	1.91	2.38
SLNB20	1.64	1.39	1.95	2.35
SLNB15	1.64	1.42	1.90	2.34
SLNB10	1.62	1.38	1.91	2.35

Table 3.6: Average oxygen coordination numbers, CN, for silicon, boron, lithium and sodium atoms in the SLNB25, SLNB20, SLNB15 and SLNB10 simulated glass compositions. The coordination numbers were calculated from the integration of the first peak of the respective g(r) for each species.

Composition	CN_{Si-O}	CN_{B-O}	CN_{Li-O}	CN_{Na-O}
SLNB25	4.03	3.23	3.58	5.53
SLNB20	4.04	3.31	3.63	6.12
SLNB15	4.06	3.26	3.64	6.22
SLNB10	4.06	3.33	4.04	6.21

3.3.3 Bond angle distributions

The bond angle distribution, g(θ), provides further information about the local geometry of the first coordination shell of each atomic species within the simulated glass structures.

The O−Si−O bond angle distributions, $g_{OSiO}(\theta)$, are shown in figure 3.7 for every simulated composition. The maximum of the distribution is located at 108.5° in the SLNB25, SLNB20 and SLNB15 glasses, while the relevant peak in the SLNB10 glass is located at a slightly smaller angle, 107.5°. It can be observed that the value of the O−Si−O bond angle in every chemical composition is in good agreement with the value of the perfect tetrahedron (109.5°), which together with the ≈ 94% 4-fold coordinated Si atoms indicates the formation of SiO_4 tetrahedra in the simulated glass structures. The "shoulder" peak in the $g_{OSiO}(\theta)$ at ≈ 90° corresponds to the small proportion of 5-fold coordinated Si atoms found in the simulated glass structures.

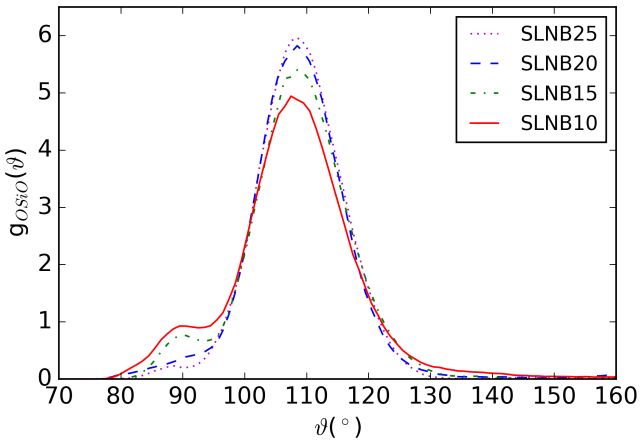

Figure 3.7: Oxygen−silicon−oxygen bond angle distributions in SLNB25, SLNB20, SLNB15 and SLNB10 simulated compositions. The peak of the distributions is located at angles close to the tetrahedral angle (109.5°), which indicates the tetrahedral local geometry for Si atoms in their first coordination shell within the four simulated glass structures.

The connection between the SiO_4 tetrahedra within the glass network can be analysed through the Si−O−Si bond angle distributions, $g_{SiOSi}(\theta)$, shown in figure 3.8 for each composition. According to the relevant distributions, the Si−O−Si bond angle between the tetrahedron linkages is about 128.5° in SLNB20 glass, 127.5° in SLNB15 glass, and 132.5° in SLNB25 and SLNB10 simulated compositions. In a pure SiO_2 glass this angle is 150°, but the addition of the alkali oxides usually leads to decrease of the Si−O−Si bond angle in the silicate network.

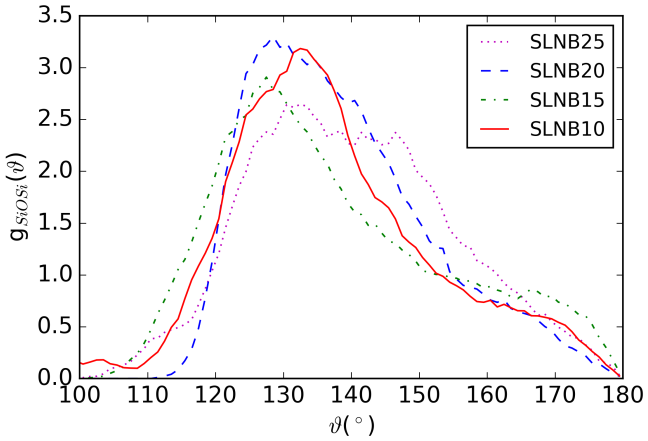

Figure 3.8: Silicon−oxygen−silicon bond angle distributions in SLNB25, SLNB20, SLNB15 and SLNB10 simulated compositions. The peak of the distributions is located at angles ≈ 130°, while in pure SiO_2 glass this angle is 150°.

The O−alkali−O bond angle distributions, $g_{OLiO}(\theta)$ and $g_{ONaO}(\theta)$, for the two alkali cations in the four simulated glass compositions are shown in figures 3.9 and 3.10 for Li and Na respectively.

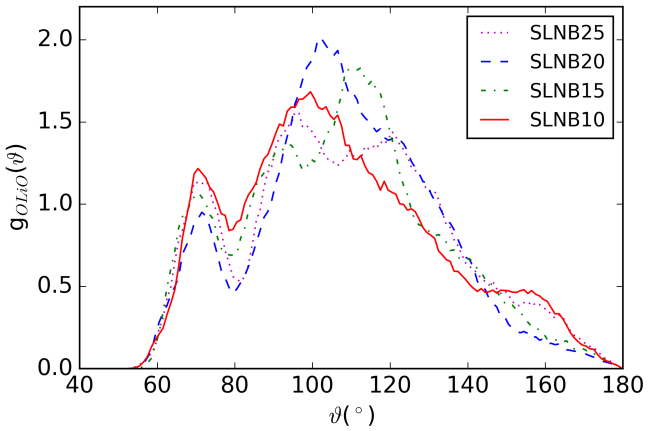

Figure 3.9: Oxygen−lithium−oxygen bond angle distributions in the simulated lithium sodium borosilicate glasses. Two peaks can be identified in every glass model, while a third peak is also revealed in SLNB25 and SLNB15 compositions.

For Li cations the distributions extend from 60° to 180° in every chemical composition. In all four lithium sodium borosilicate glasses there are two peaks, the first at

about 70° and the second at about 100°, while in SLNB25 and SLNB15 glasses a third peak can be identified, which corresponds to ≈ 120° and 112° O−Li−O angles respectively. It can be observed that the intensity of the peaks, which correspond to larger O−Li−O angles, is stronger than that of the peak, which correspond to the smaller angle. The values of these angles are relatively close to the tetrahedral angle, which, together with the average oxygen coordination number of ≈ 4 for the Li cations in the glass models, indicates that there is formation of "frustrated" LiO_4 tetrahedra within the glass structures.

For Na cations the O−Na−O bond angle distributions extend from 40° to 180° for each simulated glass. In SLNB10 and SLNB25 compositions there are two main peaks, which are located at ≈ 60° and 90°. In SLNB15 and SLNB20 glasses a peak at ≈ 60° is also revealed, but the second main peak in these distributions is appears at larger angles, at ≈ 110° and 130° respectively. The values of the O−Na−O angles obtained from the g(θ) functions, together with the 6-fold coordinated Na ions found in the glass models, suggest that the sodium cations tend to form octahedra in the simulated glass structures.

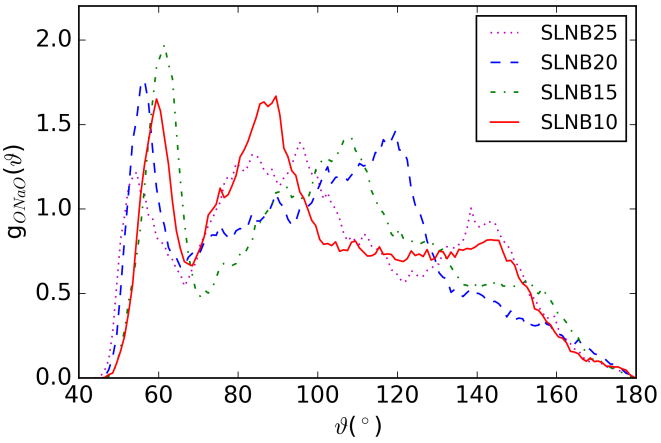

Figure 3.10: Oxygen−sodium−oxygen bond angle distributions in SLNB25, SLNB20, SLNB15 and SLNB10 simulated glass structures. In every composition the g(θ) function shows two main peaks, indicating the formation of sodium octahedra within the glass structures.

Figure 3.11 illustrates the O−boron−O bond angle distributions, $g_{OBO}(\theta)$, for B atoms in the four simulated lithium sodium borosilicate compositions. In SLNB25, SLNB20 and SLNB15 glass models, the O−B−O g(θ) functions exhibit one clear peak at 117.5°, 118.5° and 119.5°, which along with the average oxygen coordination number of ≈ 3.3, indicate that B ions have a preference to form BO_3 triangles within the glass structures. In SLNB10 glass model the relevant g(θ) bond angle distribution has a large width, including O−B−O angles from 108° to 120°, revealing a more flexible local geometry for B ions within this simulated structure. The average oxygen coordination number of ≈ 3.3 in the SLNB10 composition suggests, along with the $g_{OBO}(\theta)$, that the boron atoms form tetrahedra, as well as triangles, in the modelled system.

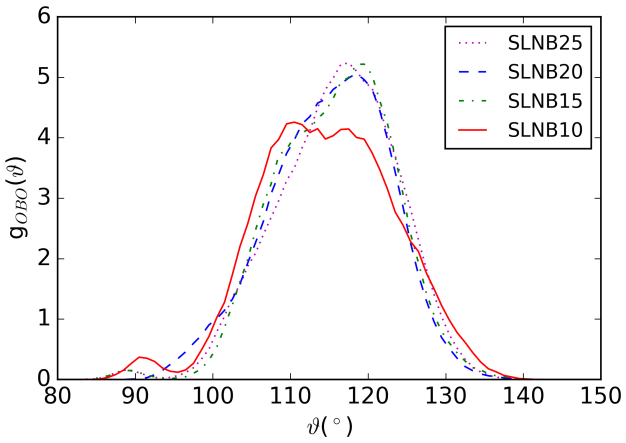

Figure 3.11: Oxygen−boron−oxygen bond angle distributions in the four simulated lithium sodium borosilicate glass structures. In SLNB25, SLNB20 and SLNB15 compositions boron atoms are present in planar ($g(\theta) \approx 120°$) local geometry, whereas in SLNB10 glass they show more flexible local environments.

The connection between the BO_3 triangles and the SiO_4 tetrahedra within the borosilicate glass network can be examined through the B−O−Si bond angle distributions, shown in figure 3.12 for every modelled composition. In SLNB10 and SLNB20 glasses the B−O−Si bond angle between the relevant linkages is about 124.5°, while in SLNB15 and SLNB25 these angles are located at 132.5° and 134.5° respectively. Two examples of the linkages between the SiO_4 tetrahedra and the BO_3 triangles within the simulated glass structures, resulting in a 3-member ring formation in the SLNB10 composition, and a 5-member ring formation in the SLNB25 glass model, are illustrated in figure 3.13.

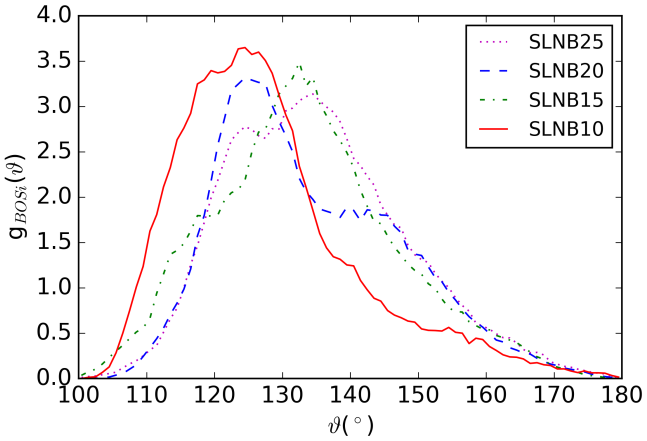

Figure 3.12: Boron−oxygen−silicon bond angle distributions in the four simulated lithium sodium borosilicate glass structures. In SLNB25 and SLNB15 compositions the peaks of the distributions are at angles of ≈ 133-135°, whereas in SLNB10 and SLNB20 glass models the peaks of the distributions are at angles of ≈ 125°.

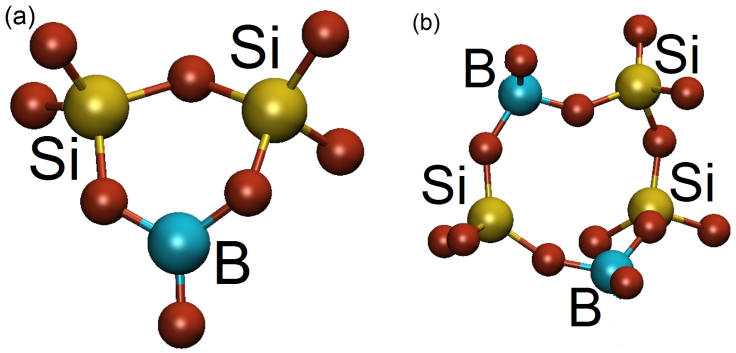

Figure 3.13: Atomistic structures of (a) 3-member ring formation in SLNB10 simulated glass structure, which is consisted of two SiO_4 tetrahdera and one BO_3 triangle; (b) 5-member ring formation in SLNB25 composition, which is made up of two SiO_4 tetrahdera and two BO_3 triangles.

3.3.4 Density of the glass structures

The calculated densities of the four simulated lithium sodium borosilicate glass structures, obtained following the approach outlined in section 3.2, were 2.36 g/cm^{-3}, 2.39 g/cm^{-3}, 2.41 g/cm^{-3}, and 2.44 g/cm^{-3} for the SLNB25, SLNB20, SLNB15 and SLNB10 glass models respectively. For the exact compositions of the modelled systems in this chapter there are no experimental density measurements available, however, the predicted densities are in good agreement with experimental densities for lithium sodium borosilicate glasses of similar molar compositions, which range between 2.43 - 2.47 g/cm^3.[226]

3.3.5 Electronic density of states

The electronic structure calculations show a HOMO-LUMO Kohn-Sham band gap of 4 eV, 3.9 eV, 3.7 eV, and 3.6 eV for the SLNB25, SLNB20, SLNB15 and SLNB10 simulated glasses respectively. Experiments have not yet determined the values of the band gap in lithium sodium borosilicate glasses. However, a comparison between the calculated values for the compositions studied in this chapter and values from modelling studies for different glasses can be performed. Previous calculations using DFT obtained a band gap of 5 - 5.3 eV for pure amorphous SiO_2,[236,237] whereas for sodium silicate glass[238] a band gap of 3.2 eV, and for lithium silicate glass[239] a band gap of 3.4 eV were predicted. A recent study reported a band gap of approximately 3 eV for sodium borosilicate glass with high Na_2O concentration.[240] The narrowing of the band gap has been associated to the addition of impurities in the pure glass,[241–243] and the presence of the Li and Na atoms is also probably responsible for the calculated values retrieved for the simulated compositions presented in this thesis.

It is well known that standard DFT calculations substantially under-estimate the band gaps, both for semiconductors and insulators,[167] and the inclusion of the Hartree-Fock exchange will provide a more accurate prediction. For this reason, calculations

with a nonlocal functional were also performed in order to compare, not only the values of the band gap, but also the behaviour between the different modelled systems. The electronic structure calculations with the hybrid functional reveal a band gap of 6.1 eV, 5.8 eV, 5.7 eV and 5.6 eV for the SLNB25, SLNB20, SLNB15 and SLNB10 glass models respectively. It can be observed that PBE predicts the band gaps in the range of 3.6 - 4 eV, while PBE0 estimates the band gaps between 5.6 - 6 eV, from SLNB10 to SLNB25 composition. Even though the difference is 2 eV between the two calculations, the two functionals predict the same trend in the behaviour of the band gap. As the $\frac{SiO_2}{B_2O_3}$ ratio increases, in other words the B_2O_3 concentration decreases in the composition, the band gap of the simulated glass structure gets slightly narrower. The calculated values of the band gap for the four glass models using the two different functionals are presented in Table 3.7.

Table 3.7: Calculated HOMO-LUMO band gap for the four simulated lithium sodium borosilicate glass structures, using a standard (PBE) and a nonlocal (PBE0) functional. An energy difference of ≈ 2 eV was observed in the calculated values with the two different functionals for each glass model. Nevertheless, the same qualitative trend was obtained in both cases with respect to the change of the $\frac{SiO_2}{B_2O_3}$ ratio in the composition.

	Band gap (eV)	
Composition	PBE	PBE0
SLNB25	4.04	6.08
SLNB20	3.91	5.82
SLNB15	3.69	5.72
SLNB10	3.63	5.63

The total electronic density of states (DOS) for the SLNB25 and SLNB10 glass models are shown in figure 3.14. In the same figure is also shown the projection of the DOS onto atomic states of the different species (PDOS), which allows the identification of the separate contributions to the total density. The total electronic density of states reveals two valence bands below the Fermi level. The lower energy band is between -25 and -18 eV and it shows a double peak structure. The peak at $E \approx$ -24 eV is associated with Na sharp features, while the peak at $E \approx$ -21 eV is mainly composed of O 2s states, and part of it can be assigned to electronic states of Si and B atoms, which have at least one non-bridging oxygen atom, since this peak is absent in fully connected networks such as pure SiO_2 and B_2O_3. These observations are in agreement with a previous modelling study in sodium borosilicate glass,[240] as well as with studies in lithium and sodium silicate glasses.[238,239,243] The second valence band is between -11 and 0 eV and it is dominated by O 2p states. Bonding states involving Si sp^3 and O 2p states, as well as hybridised 2s and 2p orbitals of B atoms, also contribute to this energy band. The top of the valence band in silicate and borosilicate glasses is usually formed by lone pair non-bridging oxygen 2p states.[236,244] It is clear that the contribution from the Si and B states in the total electronic density of states, both in valence and

conduction bands, depends on the $\frac{SiO_2}{B_2O_3}$ content in the simulated glass structure.

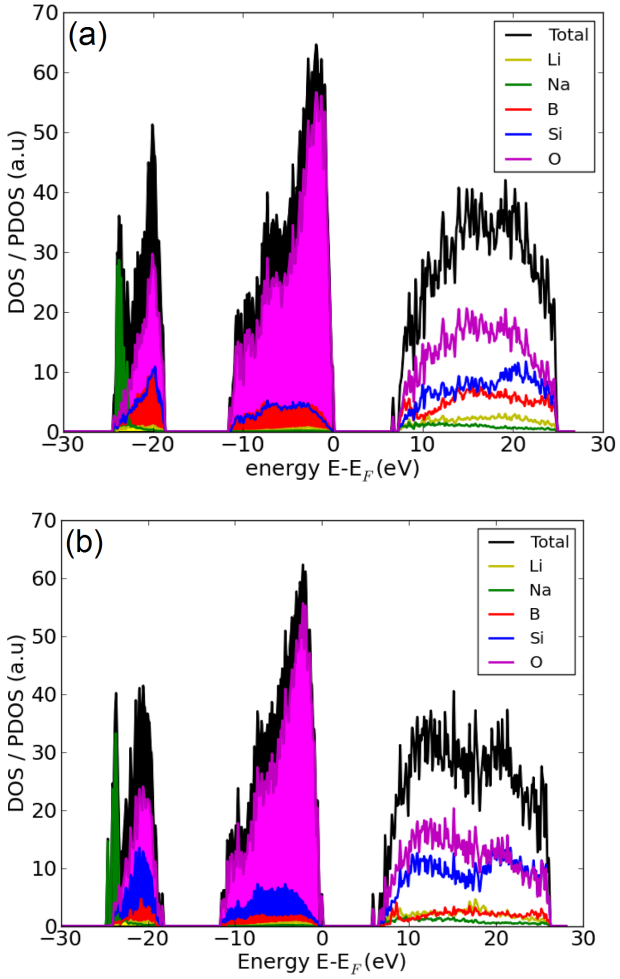

Figure 3.14: Total (DOS) and partial (PDOS) electronic density of states of the (a) SLNB25 and (b) SLNB10 glass models. In the simulated composition with the low B_2O_3 content the band gap is narrower by $\approx$ 0.5 eV than that of the glass with the high B_2O_3 concentration. In addition, the contribution of the B states in the DOS is different with respect to the $\frac{SiO_2}{B_2O_3}$ ratio.

3.4 Summary & Conclusions

In this chapter the results from two sets of simulations using classical and *ab initio* techniques, were presented in order to study the glass transition temperature, the structural features and the electronic properties of lithium sodium borosilicate glasses with compositions related to nuclear glasses of interest for the vitrification of nuclear wastes program of IHI in Japan.

In the first set of calculations, a computational method to estimate the glass transition temperature in mixed alkali borosilicate glass was implemented, and the very good agreement with the experimental data confirms the validity of the model and approximations used in this work. The inclusion of the Li_2O and Na_2O oxides in the pure SiO_2

glass leads to a decrease in the glass transition temperature, while the further doping with the B_2O_3 oxide decreases the glass transition temperature down to around 600 K.

In the second set of calculations, detailed information about the local atomic structure around the network formers, Si and B atoms, and the two alkali cations, Li and Na, was obtained from the simulations of four lithium sodium borosilicate compositions with varying the $\frac{SiO_2}{B_2O_3}$ content and fixed molar composition of the two alkali oxides. The calculated results for the geometry and the density of the simulated glass structures are in good agreement with previous modelling and experimental studies in borosilicate and alkali borosilicate glasses of similar compositions.

In addition, in this chapter the first electronic structure calculations of mixed alkali borosilicate glasses are presented. A standard and a hybrid density functional theory approach were applied and both reveal a slight dependence of the band gap on the $\frac{SiO_2}{B_2O_3}$ ratio. It was observed that by decreasing the B_2O_3 concentration the band gap in the simulated glass structure gets narrower.

4 Local atomic structure of molybdenum in nuclear waste glasses

4.1 Introduction

Molybdenum is found in high concentrations in high level nuclear waste and it is known to have low solubility in borosilicate glasses.[103] The formation of the yellow phase (described in section 1.3) during the vitrification process for the immobilisation of the nuclear waste is highly undesirable and, therefore, it is imperative to suppress the crystallisation of the molybates during melt cooling.

The molybdenum structural environment in inactive nuclear waste glasses has been investigated using extended X-ray absorption fine structure spectroscopy (EXAFS)[245] and X-ray absorption near edge structure spectroscopy (XANES)[246] probing Mo−K edge. The analysis suggests that Mo cations tends to form $[MoO_4]^{2-}$ molybdate groups which are not directly connected to the borosilicate network, and it is proposed that the molybdate tetrahedra are located in depolymerised regions (i.e. non-bridging oxygen atoms rich regions) of the glass structure surrounded by cation modifiers, both alkali and alkaline-earth ions. This specific environment of the Mo species and its complex structure are thought to be responsible for the low solubility of Mo in the glass network.[247] The prevailing oxidation state of the Mo cations in these borosilicate glass compositions is 6+, and the presence of crystalline molybdates may arise from the fact that when nuclear glasses are prepared under oxidising (O_2) or neutral (air atmosphere) conditions, molybdenum mainly occurs in this particular oxidation state (Mo^{6+}).

However, other oxidation states, such as Mo^{3+}, Mo^{4+} and Mo^{5+}, may be present under more reducing conditions or appear transiently as a result of the concentration fluctuations at the processing conditions. These species would inevitably create other structural elements, which would have different types of bonding to the glass network. Different oxidation states, known as redox states, in commercial bulk glass compositions have been studied before,[248] however, the effects of redox states on nuclear waste glasses have received much less attention so far.

Previous experimental studies demonstrated that the segregation rate of the crystalline phases, and hence the solubility of molybdenum, can be influenced by the chemical composition of the glass host. For instance, MAS NMR and Raman spectroscopy stud-

ies[247,249] revealed that when B_2O_3 concentration increases, Na cations move from their sites near non-bridging oxygen atoms to preferentially bind to BO_4 tetrahedra. This modification of the distribution of the Na cations within the glass led to a modification in the nature of molybdate crystals formed during melt cooling, as the volume fraction of $CaMoO_4$ crystals became larger while the volume fraction of Na_2MoO_4 became smaller.

It is crucial to design glasses in which the formation of the molybdate crystals is suppressed in order to maximise the waste disposal efficiency. In this thesis, *ab initio* Born-Oppenheimer molecular dynamics simulations are performed in order to model the local atomic structure of molybdenum in lithium sodium and calcium sodium borosilicate glasses and investigate the effect of ionic and covalent components on the glass structure and the formation of the crystallisation precursors. The structural motifs of the molybdenum short-range ordering provide a direct insight on the yellow phase formation and evaluate the solubility of Mo cations in the simulated nuclear glasses. The results from the BOMD simulations are compared to experimental data and the structural effects determined by the inclusion of the molybdenum cations in the glass structures are also discussed in the context of the bond valence model.

4.2 Computational details

Ab initio molecular dynamics simulations have previously been used, with some considerable success, to model the structural properties of pure silica and alkali silicate glasses,[243,250–253] as well as, sodium borosilicate glass[240] and bio-active phosphate glasses.[254–257] This approach enables accurate modelling of many-body systems and it can account for switching chemical bonds in the modelled structure. It is noted that reliable atomistic models of nuclear glasses are very limited in the literature, as classical MD simulations are hampered by the lack of reliable force fields able to describe the complex interactions in multicomponent borosilicate glass compositions.[258] Hence, BOMD, despite being computationally expensive, as compared to classical MD, is the computational method of choice in this chapter, to efficiently probe the various heterogeneous local environments found in nuclear waste glasses and provide insight into the solubility of Mo cations from the atomistic level.

Two systems with composition $(SiO_2)_{57.5} \cdot (B_2O_3)_{10} \cdot (Na_2O)_{15} \cdot (CaO)_{15} \cdot (MoO_3)_{2.5}$ and $(SiO_2)_{57.3} \cdot (B_2O_3)_{20} \cdot (Na_2O)_{6.8} \cdot (Li_2O)_{13.4} \cdot (MoO_3)_{2.5}$, which thereafter referred as BNCM and BNLM respectively, were modelled using periodic boundary conditions. The molar composition of the BNCM glass is based on nuclear waste glass compositions that have been previously studied experimentally.[249] In order to investigate the effect of the chemical nature and composition of the glass host on the local atomic structure of Mo and its solubility in the borosilicate glass network the molar composition of B_2O_3 is increased, the concentration of Na_2O is decreased and the CaO is substituted with Li_2O, resulting in the BNLM composition. It is noted that the BNLM glass is based on the SLNB20 borosilicate glass studied in the chapter 3 of this thesis, and corresponds

to a good candidate for the purpose of this study, as the SiO_2 concentration is the same, the B_2O_3 is double, the Na_2O is almost half and the Li_2O is at similar levels with respect to the molar compositions of the individual oxides in the BNCM glass. The concentration of MoO_3 is the same in both glasses in order to avoid effects due to compositional dependence of the molybdenum.

The starting configurations were generated by placing atoms randomly in a cubic simulation box with imposed constraints to avoid un-physically close separations. The total number of atoms in the BNCM glass is 202 (38 Si, 12 B, 20 Na, 10 Ca, 2 Mo and 120 O), while in the BNLM glass it is 226 (38 Si, 26 B, 8 Na, 18 Li, 2 Mo and 134 O). The densities were calculated for the mixed alkali alkaline-earth and mixed alkali borosilicate glasses before the addition of the MoO_3, following the approach described in section 3.2 in this thesis. For the calcium sodium borosilicate glass structure, the calculated value of the density was 2.59 g/cm^3, which is in very good agreement with the experimental value (2.62 g/cm^3).[259] For the exact composition of the simulated mixed alkali borosilicate glass in this study there are no experimental density measurements available, however, the calculated density of this glass composition (2.39 g/cm^3) is in good agreement with experimental densities (2.43 - 2.47 g/cm^3) for lithium sodium borosilicate glasses of similar molar composition.[226] The densities of the modelled Mo-containing nuclear waste glasses, BNCM and BNLM, were not obtainable experimentally, nor available via glass property modelling databases. Hence, the effect on the density of incorporating Mo to the two glass compositions was estimated by performing a cell optimisation using variable cell BOMD with a timestep of 1 fs and a convergence threshold of 0.1 kbar for the components of the stress tensor, and the simulation cell sizes, 13.61 Å and 13.90 Å for BNCM and BNLM respectively, were chosen to match the calculated densities of the two modelled systems.

The BOMD simulations were carried out using the CP2K code.[181] The electronic structure was treated through the DFT Kohn-Sham formulation[164] using the GGA with the PBE exchange-correlation functionals.[171] The Gaussian basis set employed for all the atomic species was a double$-\zeta$ basis set with polarisation functions $(DVZP)$[231] in conjunction with the GTH pseudopotential.[187] The plane-wave cutoff was 700 Ry and the MD timestep was 2 fs. The glass structures were generated using a melt-and-quench approach. The canonical ensemble was applied and the Nosé-Hoover thermostat chain, with a relaxation constant 0.1 ps, was chosen to control the temperature fluctuations. For each composition, the initial configuration was heated up at 2300 K with a 25 ps BOMD run to ensure that the system was melted and well equilibrated at this temperature. The molten structure was subsequently cooled using a stepwise process, consisting of a series of nine NVT BOMD runs of 10 ps each, with target temperatures set to 2000 K, 1800 K, 1600 K, 1400 K, 1200 K, 1000 K, 800 K, 600 K and 300 K. At 300 K the structure was further equilibrated for 10 ps, followed by a final BOMD production run of 10 ps, to sample the trajectories at every step and collect the structural data. This computational scheme corresponds to a total simulation time of 135 ps and a nominal cooling rate of around 20 K/ps.

Cooling rates of this order of magnitude have been used in previous simulation studies, using *ab initio* molecular dynamics,[240,255–257,260,261] in order to prepare accurate structural models of glasses that are in agreement with experimental results. It is noted that the fixed volume approach for the melt-and-quench process will generate a glass structure with high final pressure in the cell. In general, fixing the simulation cell volume to match the target-glass density throughout the melt-and-quench is a robust approach, employed and well tested in prior modelling studies in order to obtain models representative of the experimental structures. It also avoids complications due to the volume fluctuation and, thus, reduces equilibration time, which is particularly important in resource demanding DFT simulations. However, this approach results in residual pressure and stress. Energy minimisation, geometry optimisation and cell optimisation calculations were performed in the final glass structure at 300 K in order to calculate the residual pressure in the glass models and determine its effect on the final cell volume of the simulated structures. The results shown in Table 4.1 indicate that relaxation of the cell has an effect on the density of the BNCM glass but the difference is comparable to the DFT error, while almost no difference in the final glass volume after relaxation for the BNLM composition was observed. Consequently, this residual pressure does not affect the quality of the calculations, since the effect of the cell relaxation is small on the volume of both glass compositions.

Table 4.1: Calculation of the pressure and the volume of the cell for the two simulated glass structures before and after relaxation.

Type of calculation	Residual pressure (kbar)		Cell volume (Å^3)	
	BNCM	BNLM	BNCM	BNLM
Energy minimisation	-17.75	-4.57	2715.87	2687.36
Geometry optimisation	-8.68	-2.98	2715.87	2687.36
Cell & geometry optimisation	0.05	0.04	2671.59	2678.48

During the melt of the modelled systems a small drift in the total energy was recorded. The structures were melted and equilibrated with a 25 ps BOMD run and an increase of $\approx$ 5 eV in the total energy was observed over this period of time for both compositions (4.81 eV and 5.35 eV in BNLM and BNCM glasses respectively). In order to validate the performance of the timestep that used for the simulations, the initial configuration of the BNLM composition was heated up at the same temperature (2300 K) with a 20 ps AIMD run using 1 fs as timestep, and an increase of $\approx$ 4 eV was observed in the total energy over this period of time in this case. Although, a smaller timestep leads to a decrease in the drift of the total energy, this does not differ greatly from the one observed with the 2 fs, as in higher temperatures the narrowing of the band gap causes a drift in the kinetic energy which cannot be avoided. It is noted that the choice of the timestep is related to the whole melt-and-quench protocol and the relatively high value of 2 fs that used for the BOMD simulations is compensated with the slow cooling

rate applied to generate the glass structures.

4.3 Results of calculations & Discussion

4.3.1 Short-range order of network formers

Silicon and boron atoms have the role of the network formers in the polymerised network of the nuclear glasses.[20] The local environments around Si and B were analysed through the pairwise radial distribution functions, g(r), shown in figure 4.1 for the BNLM glass. In both glass compositions, Si was found to be 96% 4-coordinated and 4% 5-coordinated to oxygen atoms with an average Si−O interatomic distance of 1.64 Å. The typical measurements from the literature for the Si−O bond length are 1.58 - 1.64 Å for a broad range of silicate glasses, and specifically in borosilicate glasses, Cormier *et al.*[233] reported a Si−O interatomic distance of 1.60 Å. The average B−O interatomic distance was calculated 1.40 Å and 1.41 Å in the BNCM and BNLM simulated glasses respectively, while the average coordination number was 3.4 for both glass compositions. However, further analysis of the glass models shows that B ions have two different coordination environments within each glass structure. 3- and 4-coordinated B ions were found to exist simultaneously in both glasses in the form of BO_3 triangles and BO_4 tetrahedra respectively. Majérus *et al.*[235] measured the B−O bond length in nuclear glasses 1.38 Å and 1.47 Å for 3- and 4-coordinated B atoms respectively.

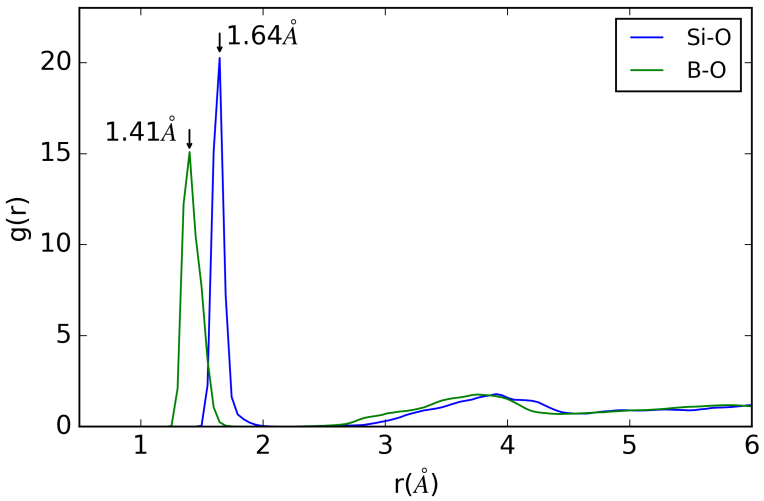

Figure 4.1: Pairwise radial distribution functions of the network former−oxygen interatomic distances for Si and B atoms in the simulated lithium sodium borosilicate nuclear glass (BNLM composition). It is noted that, the g(r) functions are almost indistinguishable for the BNCM and BNLM glass models.

It is also noted that the calculated results presented in this thesis are in very good agreement with a previous modelling study in lithium sodium borosilicate glasses, as Connely *et al.*[234] reported for Si and B similar interatomic distances, 1.58 Å and 1.41 Å for Si−O and B−O respectively, and coordination numbers 4 and 3.5 for Si and

B respectively. A recent first principles simulation study reported also 7.5% 5-fold coordinated Si for sodium borosilicate glass.[240]

The O−Si−O bond angle distribution, g(θ), shown in figure 4.2 for the BNLM glass, provides further information about the first coordination shell of Si atoms in the glass structure. The peak of the distribution is located at 108.5°, close to the tetrahedral angle (109.5°), which is indicative of the formation of near perfect SiO_4 tetrahedra in the simulated glass structure. The O−B−O g(θ) for both compositions are shown also in figure 4.2, and reveal further details about the structure of the B environment in the two glass models. In BNCM glass, the O−B−O g(θ) exhibits two almost equivalent peaks at 110.5° and 121.5°, which along with the average coordination number of 3.4 indicate that B ions have flexible local environment within the BNCM glass forming triangles and tetrahedra. On the contrary, in BNLM glass the O−B−O g(θ) has only one peak at 110.5°, which suggests that B ions have a stronger preference for tetrahedral local environment in the lithium sodium borosilicate (BNLM) glass model. However, it is noted that the large width of the g(θ) in BNLM glass, along with the coordination number of 3.4, indicate that the modelled system contains also distorted, i.e., non-planar 3-coordinated B ions.

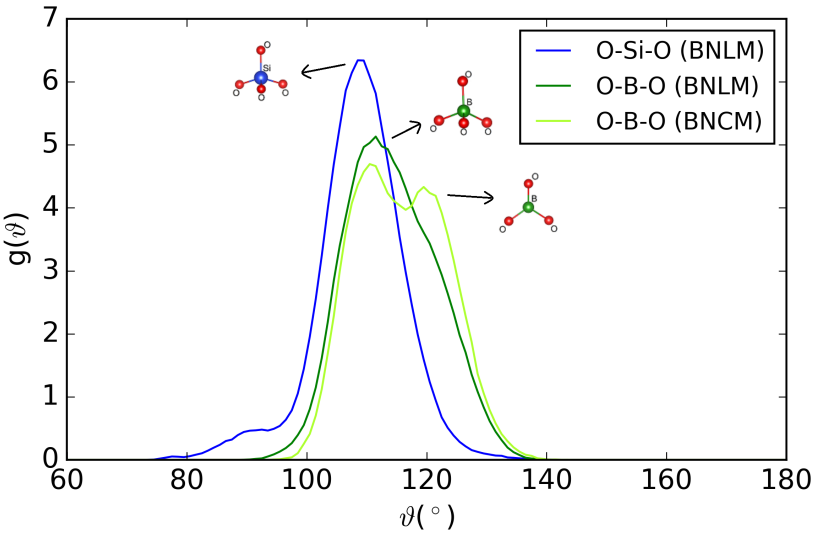

Figure 4.2: Oxygen−network former−oxygen bond angle distributions for Si atoms in BNLM glass, and for B atoms in BNCM and BNLM compositions. Tetrahedral local geometry for Si atoms in their first coordination shell within the BNLM glass. Boron is present in planar (g(θ) ≈ 120°) and tetrahedral (g(θ) ≈ 109.5°) environments within both glass structures. It is noted that, the O−Si−O g(θ) are indistinguishable for the BNLM and BNCM glass models.

4.3.2 Short-range order of Ca, Li and Na

Structural analysis for the short-range ordering of the alkali and alkaline-earth cations was also performed through the pairwise radial distribution functions, g(r), shown in figure 4.3. The average oxygen interatomic distances for the three cations are Ca−O =

2.30 Å, Li−O = 1.94 Å and Na−O = 2.34 Å and 2.39 Å in the BNCM and BNLM simulated glasses respectively, while the average oxygen coordination numbers around Ca, Li and Na ions were found to be 5.8, 4.1 and 5.6 (in BNCM)/6.7 (in BNLM) respectively. A previous modelling study in lithium sodium borosilicate glasses[234] reported an average Li−O interatomic distance of 2.07 Å with an average oxygen coordination number 3.5, while a neutron diffraction study in lithium silicate glasses[7] reported 4-coordinated Li atoms and an Li− O interatomic distance of 1.99 Å. The Na−O bond length was calculated in borosilicate glasses 2.2 - 2.55 Å by Cormier *et al.*,[233] and 2.82 Å by Connelly *et al.*[234], with an average oxygen coordination number for Na cations 8 in both studies. Finally, Michel *et al.*[259] measured the Ca−O interatomic distance 2.35 Å in nuclear glass compositions. Overall, the calculated values of the bond lengths and oxygen coordination numbers, presented in this thesis, for the alkali and alkaline-earth cations in the two modelled compositions are in very good agreement with prior experimental and modelling studies from the literature.

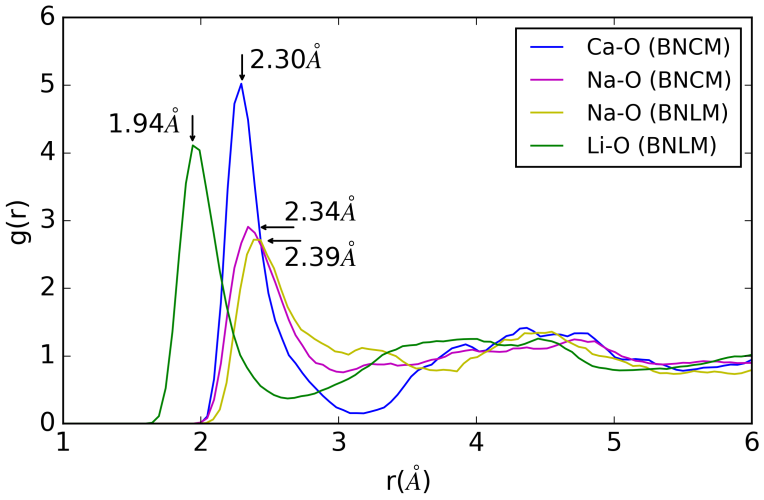

Figure 4.3: Pairwise radial distribution functions of the alkaline-earth (Ca)−oxygen and the alkali (Na and Li)−oxygen interatomic distances in the BNCM and BNLM simulated compositions. The Na−O bond length is slightly longer in the BNLM glass than that in the BNCM glass.

The O−cation−O bond angle distributions, g(θ), shown in figure 4.4 for the two simulated glass compositions, further highlight the structure of the coordination shell of Ca, Li and Na ions and give information about the connection of the cations with the oxygen species within the glass structures. A peak in the g(θ) at $\approx 90°$ is due to the bonding between the cation and two non-bridging oxygen atoms (NBO−cation−NBO) belonging to different chains of tetrahedra in the borosilicate network. A peak in the g(θ) at $\approx 60°$ originates from the linkages of the cation to two bridging oxygen atoms (BO−cation−BO) or one bridging and one non-bridging oxygen (BO−cation−NBO) belonging to the same tetrahedron.[256,262]

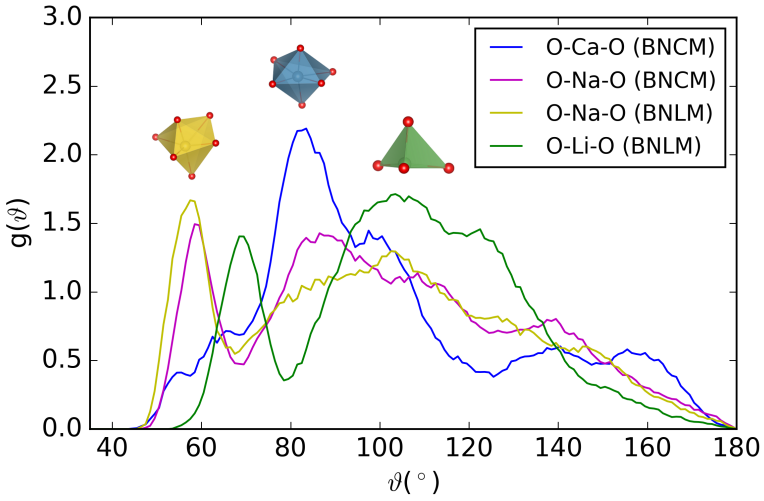

Figure 4.4: Oxygen−cation−oxygen bond angle distributions for Ca, Na and Li cations in the BNCM and BNLM simulated glass structures. Na and Ca cations have an octahedral geometry in their first coordination shell within both glass compositions, while Li cations form LiO_4 tetrahedra in the BNLM glass.

In O−Ca−O g(θ) function there is one main peak located at 83.5°, which indicates that the distribution is dominated by the NBO−Ca−NBO contribution. The combined information of the average oxygen coordination number ($\approx$ 6.0) together with the peak at the g(θ) (at $\approx$ 90°) suggests that the first coordination shell of the Ca ions has a strong preference for the octahedral geometry in the BNCM glass. The O−Li−O g(θ) function feature two peaks located at 68.5° and 106.5°. The intensity of the second peak is stronger than that of the first peak and its value is quite close to the tetrahedral value. Hence, together with the 4-coordinated Li ions found in the BNLM composition, this suggests that there is formation of LiO_4 tetrahedra in the glass structure. In O−Na−O g(θ) functions there are also two peaks, which are located at 58.5°/86.5° and 57.5°/99.5° in the BNCM and BNLM compositions respectively. The Na cations tend to form octahedra in both glass structures, but the connection of the cation with the oxygen species changes. The intensity of the first peak for the g(θ) function in the BNLM glass is stronger than that of the respective peak in the BNCM composition, which indicates that Na cations have a stronger preference to connect with two bridging oxygen atoms or one bridging and one non-bridging oxygen of the same SiO_4 and/or BO_4 tetrahedron within the BNLM glass.

The average oxygen interatomic distances and the corresponding oxygen coordination numbers for Si, B, Ca, Li and Na in the BNCM and BNLM simulated glass structures are summarised in Table 4.2.

4.3.3 Local environments of Mo

The local environment around the Mo cations was characterised in the BNCM and BNLM compositions using the pairwise radial distribution functions, g_{Mo-O}(r), shown

Table 4.2: Average oxygen interatomic distances and average oxygen coordination numbers for the network formers (Si and B), and the alkaline-earth (Ca) and alkali (Li and Na) cations in the BNCM and BNLM simulated glass structures. The bond lengths correspond to the first peak position of the respective pairwise radial distribution functions, while the coordination numbers were calculated from the integration of this peak for each species.

	Bond length (Å)		Coordination number	
Atom pair	BNCM	BNLM	BNCM	BNLM
Si−O	1.64	1.64	4.04	4.04
B−O	1.40	1.41	3.4	3.4
Ca−O	2.30	–	5.8	–
Li−O	–	1.94	–	4.1
Na−O	2.34	2.39	5.6	6.7

in figure 4.5. The first peak of the distribution function gives information about the first coordination shell of the Mo cations in the two nuclear glasses modelled in this thesis. It can be observed that in BNCM composition the g(r) has one clear peak which corresponds to an average bond length Mo−O = 1.75 Å, whereas in BNLM glass the g(r) exhibits two distinct peaks in the first coordination shell. The strongest peak corresponds to a Mo−O bond length of 1.75 Å, as in the BNCM glass structure, and the other sharp peak corresponds to a Mo−O bond length of 1.94 Å. The average oxygen coordination number around the Mo cations was found to be 4.0 and 4.2 for the BNCM and BNLM glasses respectively, and thus, the molybdenum ions are mainly 4-fold coordinated to oxygen atoms in the simulated glass structures.

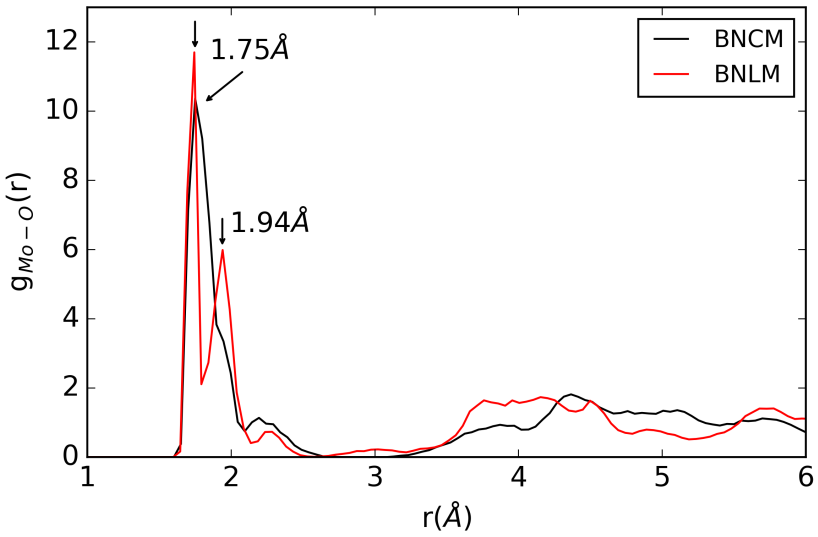

Figure 4.5: Pairwise radial distribution functions for the molybdenum−oxygen interatomic distances in the BNCM and BNLM simulated compositions. The maxima at 1.75 Å coincide for the two glass models. In BNLM glass the g(r) manifests a second peak in the first coordination environment located at 1.94 Å.

It is noted that the same cutoff, 2.2 Å, which corresponds to the local minima of the distributions, was used to calculate the integral of the first peak of the Mo−O g(r) for each glass model, in order to avoid dependence on the cutoff to the calculation of the coordination number and be able to make a comparison between the two modelled compositions. In order to evaluate the accuracy of the selected value for the cutoff, the same analysis for larger cutoff was performed, and no significant changes for the calculated coordination numbers was observed, as for 2.7 Å cutoff, which corresponds to the value g(r) goes to zero, the coordination numbers were found to be 4.1 and 4.3 for the BNCM and BNLM glasses respectively. Hence, the local minimum value that was used for the calculations covers with success the whole first coordination shell for both structures and is sufficient for the calculation of the coordination numbers.

The bond angle distribution, g(θ), can provide further information about the structure of the first coordination shell of the Mo cations. The O−Mo−O g(θ) function for the BNLM composition is illustrated in figure 4.6, and it can be seen that there is one main peak located at 102.5°, which has the higher intensity in the distribution and is relatively close to the value of the perfect tetrahedron (109.5°). The combined information of the average oxygen coordination number and the g(θ) indicates that the coordination environment of Mo cations in the simulated nuclear glasses has a strong preference to tetrahedral geometry, resulting in the formation of MoO_4 molybdate tetrahedra.

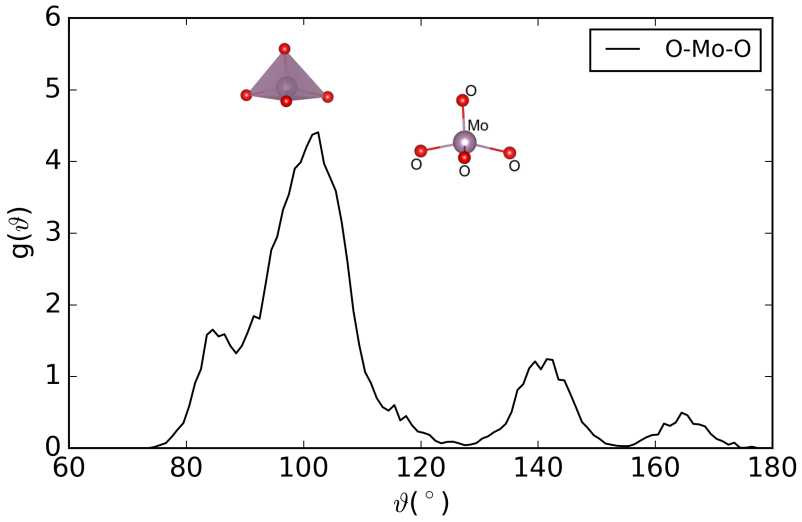

Figure 4.6: Oxygen−molybdenum−oxygen bond angle distribution in the BNLM simulated glass structure. The distribution shows three peaks and one shoulder. The main peak corresponds well to the tetrahedral coordination, and hence the Mo cations have a preference to the tetrahedral local geometry in their first coordination shell, forming MoO_4, in agreement with experimental data.

The calculated values, presented in this thesis, for the local atomic structure of Mo cation in the two simulated compositions are in very good agreement with EXAFS and XANES studies in nuclear borosilicate glasses.[104,246,247] The EXAFS data acquired from high level nuclear waste glasses with similar compositions[245] reveal an analogous picture

for the molybdenum local environment, as these data demonstrate that Mo cations are 4-coordinated to oxygen with an average Mo−O interatomic distance of 1.76 - 1.78 Å, which leads to the formation of MoO_4 tetrahedrally coordinated species.

The values of bond length, coordination number and bond angle for the Mo cation in the BNCM and BNLM simulated glass structures are summarised in Table 4.3. It is noted that the molar composition of MoO_3 (2.5 %) in the two simulated glasses corresponds to 2 Mo atoms for ≈ 200 atoms simulation cell. Consequently, due to the small number of Mo cations in the periodic cell, the amount of data is insufficient for accurate statistical representation of the local atomic structure of Mo. Nevertheless, these results are sufficient in order to distinguish between different types of Mo local environment. In addition, the results of the simulations are in very good agreement with experimental data, which validates the accuracy of the calculations for the two glass models and, therefore, these structures are treated as representative for the purpose of this study. It is also noted that accumulating reliable statistics for such systems requires either a large number of simulations and/or simulations of large system. However, modelling of disordered systems containing low concentration dopants is computationally demanding, as *ab initio* molecular dynamics simulations are very expensive, and only the available computational resources limit the size of the glass models.

Table 4.3: Analysis of the molybdenum first coordination shell, through the bond length, coordination number and bond angle, and comparison between the two simulated glass structures.

Composition	Mo−O (Å)	Coordination number	O−Mo−O (°)
BNCM	1.75	4	103.5
BNLM	1.75 & 1.94	4.2	102.5

The MoO_4 tetrahedral formation within the glass structure, and also its connection with the other species in the BNCM composition, is shown in figure 4.7. The atomistic structure reveals that the molybdate tetrahedron is located in a region surrounded by alkali (Na) and alkaline-earth (Ca) cations and it is not linked directly to the borosilicate network. This specific structural position within cationic domains and the absence of connectivity with the polymerised glass network explains the low solubility of Mo in nuclear waste glasses and the possible phase separation of a yellow phase consisting of sodium or calcium molybdates.

The local environment of the Mo cation in the BNLM glass model is shown in figure 4.8. For the 4-coordinated Mo cation, two of the Mo−O bonds are due to the first peak in the g(r), which corresponds to a shorter interatomic distance, whereas the two other bonds correspond to the second peak at the larger interatomic distance. This picture confirms that for average Mo−O interatomic distances of ≈ 1.75 - 1.78 Å, the molybdate tetrahedra do not link to network formers within the glass structure. However, the longer Mo−O bond lengths, which are possible in the BNLM composition,

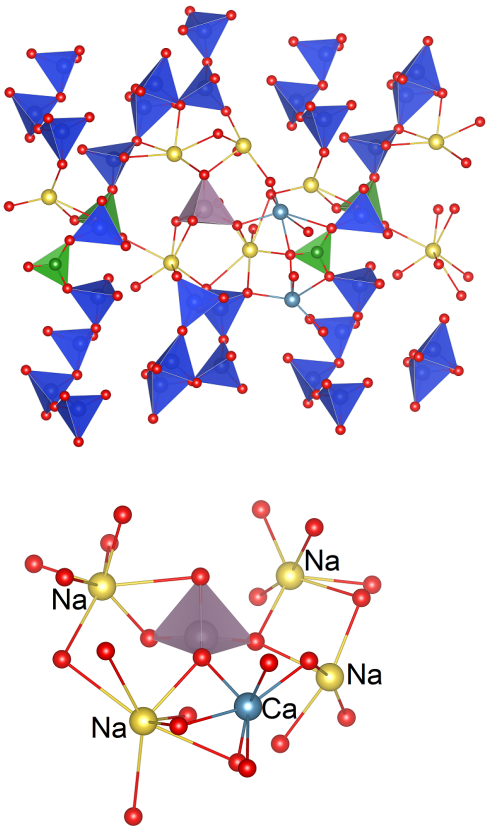

Figure 4.7: Tetrahedral coordination environment of the Mo cation and location within the glass network in the calcium sodium borosilicate (BNCM) simulated composition. The MoO_4 tetrahedron is surrounded by Na and Ca cations, there is no connectivity with the borosilicate network and the molybdate unit is linked to the rest of the host lattice via the ionic bonds only. Light gray ball is Mo, blue ball is Si, green ball is B, light blue ball is Ca, yellow ball is Na and red ball is O.

enable the MoO_4 tetrahedron to connect with Si and B atoms and incorporate, partially, into the borosilicate glass network.

4.3.4 Validation of the Mo−O− linkages

The bond valence model[263] was used to further investigate the Mo−O− linkages with the network formers and the alkali and alkaline-earth cations in the BNCM and BNLM glass structures. The valence, S, of the Mo−O bond was calculated using the equation:

$$S_{Mo-O} = exp\left[\frac{R_0 - d(Mo-O)}{b}\right] \tag{4.1}$$

where R_0 = 1.907 Å is the bond valence parameter for an oxidation state of 6+ for the Mo cation, $d(Mo-O)$ is the molybdenum−oxygen interatomic distance and b is a constant (b = 0.37 Å).[264,265] According to this model, the sum of the bond valences relative to an oxygen atom must be less than or equal to the theoretical value of 2.0 valence units.

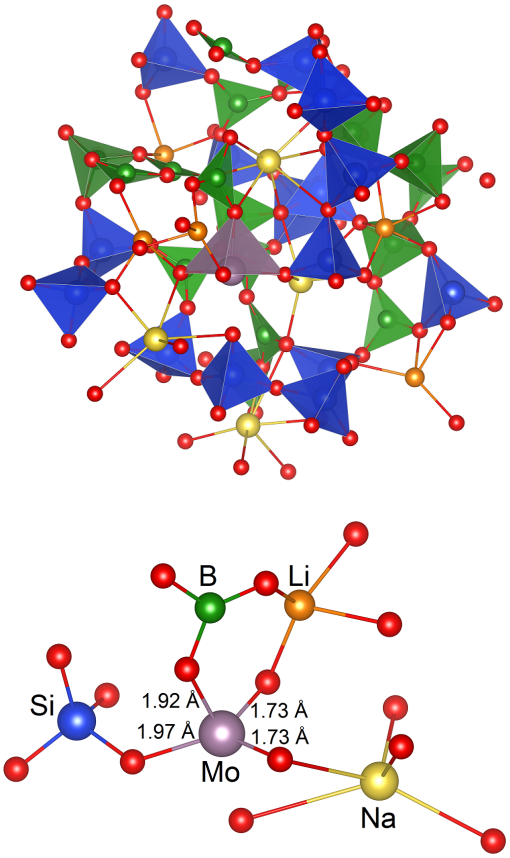

Figure 4.8: Tetrahedral local environment of the Mo cation and connection with the other species in the lithium sodium borosilicate (BNLM) simulated glass structure. The MoO_4 tetrahedron is located closer to the network formers (Si and B atoms), and the longer Mo−O bonds enable the partial connection of the molybdate unit with the polymerised network of the glass. Light gray ball is Mo, blue ball is Si, green ball is B, orange ball is Li, yellow ball is Na and red ball is O.

The Mo−O−Si linkage in figure 4.8 corresponds to Mo−O = 1.97 Å and, based on the equation 4.1, the bond valence is $S_{Mo-O} = 0.84$ v.u.. The sum of the bond valences for this particular oxygen is $S_{Mo-O} + S_{Si-O} = 1.84$ v.u. < 2.0 v.u., assuming that for the 4-coordinated Si atom the bond valence is $S_{Si-O} = 1.0$ v.u..[266] The Mo−O−B linkage in figure 4.8 corresponds to Mo−O = 1.92 Å and the relative bond valences are $S_{Mo-O} = 0.98$ v.u. and $S_{B-O} = 0.77$ v.u. for the 3-coordinated B atom,[266] which results in a sum of the bond valences 1.75 v.u. < 2.0 v.u.. In both cases, the Pauling's stability rules[267] are fulfilled, as the sum of the bond valences is less than 2.0 v.u. for the oxygen between Mo and Si or B respectively, and therefore the specific oxygen atom will not be over-bonded. Consequently, the molybdenum−oxygen linkages with the network formers are not forbidden within the glass network of the BNLM composition for the larger Mo−O interatomic distances, which are possible in the first coordination shell of Mo cations in this glass model.

For the two shorter Mo−O bonds (1.73 Å) in figure 4.8 the calculated bond valence is $S_{Mo-O} = 1.61$ v.u.. The molybdenum−oxygen linkages with Si and B in these cases

are forbidden as the sum of the bond valences would be 2.61 and 2.38 v.u. respectively, which are much larger than 2.0 v.u. for the oxygen between the cations. In such a situation the oxygen atom would be over-bonded, so for these shorter interatomic distances the oxygen from the Mo−O bond is connected to an alkali cation (Li or Na). In the BNCM composition the calculated S_{Mo-O} bond valence for the average Mo−O interatomic distance (1.75 Å) also results in a sum of bond valences larger than 2.0 v.u. for the oxygen atom, which leads again to forbidden connections with the network formers within the glass structure, and results in an MoO_4 tetrahedron isolated from the polymerised network.

The mean of the S_{Mo-O} bond valences for the 4-coordinated Mo cation can be also used to estimate the oxidation state, and based on this approach, the Mo cation in the BNCM glass was found to have an oxidation state +6, whereas Mo in the BNLM composition has a redox oxidation state, +5. Electron spin resonance (ESR) spectra of alkali borosilicate nuclear waste glasses, containing 1% mol MoO_3, melted under reducing conditions,[268,269] demonstrate that at least partial reduction of the oxidation state of Mo cations has occurred. Moreover, ESR studies in calcium sodium borosilicate glasses[246,268–271] have revealed that even under oxidising conditions some of the molybdenum is present as Mo^{3+} or Mo^{5+}.

4.3.5 Effect of glass composition on Mo local environments

The alkali and alkaline-earth cations have a multiple role within the borosilicate network as they can act as network modifiers[20] and charge compensators.[245] Classical MD simulations in alumino-borosilicate glasses show that most of the Na cations charge compensate network forming Al or B atoms. These calculations have been recently improved by a combination of MD and reverse Monte Carlo calculations based on wide angle X-ray scattering.[233]

In the two nuclear glasses modelled in this thesis, the Ca and Li cations exhibit different coordination environments within the simulated glass structures, while Na cations seems to have different role in the BNCM composition than that in the BNLM glass.

In BNCM glass Na and Ca cations have a pure network modifying role. The borosilicate network is significantly modified as the cations break the bonds between the Si/B and O atoms, and the alkali and alkaline-earth cations tend to cluster within the glass structure, forming the domains in which the molybdate tetrahdron prefers to locate (see figure 4.7). In addition, the B atoms are mainly 3-coordinated within the BNCM glass and, hence, the crystalline molybdate units will form as a result of the higher availability of modifier cations in presence of majority 3-coordinated boron, as the only charge compensating cations that can be found around the MoO_4 tetrahedron to stabilise its negative charge are Na and Ca ions.

On the contrary, in BNLM composition the tetrahedral local geometry for the B atoms is more favourable within the glass structure. In this glass model the Na−O bond

length elongates (from 2.34 Å in BNCM to 2.39 Å in BNLM) and the Na cations move from positions near non-bridging oxygen atoms to positions near BO_4 tetrahedra to act as charge compensators. Consequently, the number of Na cations able to compensate the MoO_4 tetrahedra strongly decreases, and the depolymerised regions in which the MoO_4 units are usually located become depleted in Na when the B_2O_3 concentration increases and the Na_2O decreases. The Li cations, according to their first coordination environment, seems to act as pseudo-network formers within the BNLM glass structure, and thus, the replacement of CaO for Li_2O oxide leads to less depolymerisation of the borosilicate network, allowing the MoO_4 tetrahedron to approach closer to Si and B atoms and, hence, increasing in that way the possibility of incorporation.

It is noted that the results presented in this thesis are consistent with previous experimental studies of sodium calcium borosilicate nuclear glasses containing MoO_3, in which, structural investigations by MAS NMR and Raman spectroscopy[247,249] revealed that increasing the B_2O_3 concentration in the composition of the glass strongly modifies the distribution of Na cations within the glass structure, which leads to an evolution of the nature of molybdates that can crystallise during melt cooling.

4.4 Summary & Conclusions

In this chapter two models of nuclear waste glasses with different molar compositions were studied by means of *ab initio* molecular dynamics simulations, in order to investigate the dependence of the Mo local environment on the chemical nature and molar composition of the nuclear glass.

Detailed information about the local atomic structure around the network formers (Si and B atoms) and the alkali (Li and Na) and alkaline-earth (Ca) cations was obtained from the calculations, and the results are in very good agreement with previous modelling and experimental studies in borosilicate glasses, providing a good validation for the simulated glass structures in this thesis.

The Mo cations were found to exist in a tetrahedral environment forming almost perfect MoO_4 in both glass models. The position of the first peak in the Mo−O pairwise radial distribution function is at 1.75 Å for both compositions. However, in the BNLM glass the g(r) manifests a second sharp peak in the first coordination shell, which corresponds to a larger interatomic distance, 1.94 Å, resolving a qualitatively different type of Mo bonding with the neighbouring oxygen atoms.

Detailed structural analysis demonstrated that the MoO_4 tetrahedron exhibit different structural positions within the glass network in the BNCM and BNLM compositions, coupled also with the electronic state of the Mo species. In BNCM composition the MoO_4 unit is isolated from the borosilicate glass network and is located in a depolymerised region of the glass structure surrounded by alkali and alkaline-earth cations. The shorter Mo−O bonds in this simulated structure results in +6 oxidation state for the Mo cation, which is indicative for the crystallisation of the molybdate tetrahedron. In contrast, in BNLM composition the MoO_4 tetrahedron is located closer to the network

formers and there is connectivity of the molybdate unit with the polymerised glass network. The longer Mo−O bonds in BNLM glass result in a redox state, Mo^{+5}, at room temperature for the molybdenum in this composition, which enables the connection of the MoO_4 tetrahedron with the borosilicate glass network. Thus, reducing the valency of the Mo cation could both eliminate the formation of the isolated alkali/alkaline-earth molybdates and increase the solubility of Mo cation in the borosilicate glass network by reducing the field strength around the cation.

Atomistic simulations are able to provide atomistic pictures of the glass structures and detailed insight into compositional-atomic structure relationships. In the two nuclear waste glasses modelled in this thesis, it seems that the stability of the Mo cation in the polymerised glass network is correlated to the glass composition. The structural data from *ab initio* molecular dynamics simulations, together with the bond valence model, suggest that increasing the B_2O_3 concentration, decreasing the Na_2O concentration and replacing of CaO for Li_2O oxide will decrease the tendency to form yellow phase within the glass structure and, hence, enhance the solubility of Mo cation in the glass network.[272]

5 Structure and ionic diffusion of alkaline-earth ions in mixed cation silicate glasses

5.1 Introduction

Amorphous silica doped with alkali and alkaline-earth ions is used for various applications and forms the basis for a wide range of commercially available products, including window glasses, solid electrolytes and glasses used for nuclear waste disposal. The addition of ions affects the structural, dynamical and transport properties of the host silica glass and, thus, enables tailoring of its characteristics to a diverse range of applications.

The structure of sodium calcium silicate glass has been modelled using molecular dynamics for several concentrations of the cation impurities.[198,232,273] The Ca species were found to modify the silica structure in a similar way to Na. The coordination number of Ca is about six, while the O−Ca−O bond angle distribution shows that its coordination polyhedron is a reasonably regular octahedron. A combination of the bond length data and the bond angle distribution suggests that the modifier cations are connected to BO of a single SiO_4 tetrahedron, while the NBO are preferentially bonded to Ca rather than to Na ions due to its larger field strength. The medium-range order of these glass structures remains unchanged and seems to be unaffected by the molar composition of the sodium and calcium oxides. Mixed alkali/alkaline-earth silicate glasses containing Na, Ca and Sr for several molar compositions have been studied using neutron diffraction, reverse Monte Carlo (RMC) modelling and vibrational spectroscopy techniques.[274] The local environments of Ca and Na were again similar in these modelled systems, whereas the short-range order of Sr was different from the other cations, probably due to its slightly larger ionic radius. In addition, the structural analysis highlights that the replacement of Ca by Na opens up the glass structure, which was attributed to the fact that the Ca^{2+} ions are replaced by twice as many Na^{+} ions.

Experimental research has revealed that mixed alkali/alkaline-earth silicate glasses exhibit mixed cation effects, which are manifested in the diffusion of the both alkali and alkaline-earth cations. For example, in sodium calcium silicate glasses, the mobility of both Na and Ca increases when CaO is partially substituted by Na_2O. The increase

in the number of cation sites leads to the structure modification described above and results in the formation of additional diffusion pathways. In turn, this enhances diffusion of both Na^+ and Ca^{2+} ions, since Ca^{2+} ions may make use of the empty Na^+ sites. In other words, Na^+ ions stimulate diffusion of the Ca^{2+} ions. Consequently, when an alkali and an alkaline-earth ion are mixed together, a kind of inverse mixed mobile ion effect occurs, referred to as "the mixed alkali/alkaline-earth anomaly".[275] It is noted that Ca^{2+} ions seems to be less mobile that Na^+ ions due to the higher field strength of their bond with the oxygen atoms within the glass structure. In silicate glasses containing an alkali and several alkaline-earth cations, for instance Na, Ca and Sr, a mixed alkaline-earth effect, similar to the mixed alkali effect, is found, such that the mobility of the alkaline-earth ions is lower in the mixed composition than in the single alkaline-earth glass.[47]

The most interesting compositions in terms of the anomalous mobilities of the alkaline-earth ions are $A_2O{-}2MO{-}4SiO_2$, in which A is an alkali and M is an alkaline-earth cation. A combination of experiments, such as radio tracer diffusion techniques, dynamic mechanical loss spectroscopy and conductivity measurements, gives a thorough picture of the alkaline-earth diffusion in these mixed cation glasses.[36,276–279] These measurements reveal a distinct correlation between the alkaline-earth cation mobility and the ratio of the alkaline-earth cation radius to that of the alkali cation. The alkaline-earth ions are more mobile if this ratio is close to unity, i.e. when the alkali and alkaline-earth ions in the glass structure are of similar size. In spite of extensive experimental studies, understanding of atomic scale processes resulting in the enhancement or suppression of the alkaline-earth cation diffusion is lacking and modelling studies have been limited to RMC modelling of compositions with particular combinations of the cations (Na/Ca and Na/Sr silicate glasses).[274]

In this thesis, classical MD simulations are used to investigate the mixed cation effects observed experimentally in $A_2O{-}2MO{-}4SiO_2$ compositions in order to understand the effect of the type of the cations on the structural, vibrational and transport properties of the alkaline-earth ions in the glass structure. Detailed analysis of the short- and medium-range order, as well as of the short-time dynamical behaviour, of the alkaline-earth cations is presented. The mobility of the alkaline-earth ions is examined through the calculation of the diffusion coefficients and, hence, the activation energy for diffusion of the cations is evaluated in each simulated structure. The results from the MD simulations are compared to experimental data and they are also discussed in the context of a theoretical model proposed by Kirchheim in order to describe the trends in the mobility of the alkaline-earth ions in the simulated glasses.

5.2 Computational details

A series of nine mixed cation silicate glasses of the composition $A_2O{-}2MO{-}4SiO_2$ with all possible combinations of A = Li, Na, K and M = Ca, Sr, Ba, was modelled using periodic boundary conditions. The total number of atoms of each type was: A = 494, M

= 494, Si = 987 and O = 2715, and it was kept the same in every glass in order to avoid compositional dependence and focus on the effect of the type of the alkaline-earth cation on the calculating properties. The atoms were placed randomly in a cubic simulation box with imposed constraints to avoid non physically small interatomic distances, and the cell size was calculated from the experimental density for each structure.[276–279] The various glass compositions in terms of the alkali/alkaline-earth cations combination, the density and the simulation box size for every modelled structure are shown in Table 5.1.

Table 5.1: The combination of the alkali and alkaline-earth cations in the $A_2O{-}2MO{-}4SiO_2$ composition, experimental density of each glass and the corresponding simulation box size of the modelled systems. The total number of atoms in each structure is 4690.

A & M cations	Density (g/cm^3)	Cell size (Å)
Li/Ca	2.68	38.82
Na/Ca	2.72	39.68
K/Ca	2.66	40.98
Li/Sr	3.23	39.28
Na/Sr	3.19	40.31
K/Sr	3.10	41.53
Li/Ba	3.64	40.20
Na/Ba	3.62	41.01
K/Ba	3.51	42.15

The pairwise potential model developed by Pedone *et al.*[197] (see equation 2.62) and described in section 2.7 was employed for the calculations. The DL_POLY classic package[230] was used for the MD simulations and the velocity Verlet algorithm was applied for the integration of the equations of motion with a timestep of 1 fs. The Coulomb interactions were calculated using the Ewald summation method[151] with a precision of 10^{-6}. The cut off for the short-range interactions was set to 8 Å.

The glass structures were generated using a melt-and-quench approach. The canonical ensemble was applied to keep the density of the simulated glass close to the experimental value. The Berendsen thermostat was used to control the temperature fluctuations with a relaxation constant 0.1 ps. The system was heated up gradually in steps of 500 K with a 25 ps MD run at each temperature. The molten structure was equilibrated at 6500 K using first the NVT and then the NVE ensembles with 400 ps MD run in total in order to ensure that the structure was well equilibrated at this temperature. The system was subsequently cooled using a uniform stepwise process, with temperature decrements of -200 K and 60 ps NVT runs at each temperature, until the temperature of the system reached 300 K. A further 200 ps NVT run was carried out at 300 K, followed by a 200 ps NVE run in order to equilibrate the structure and collect the data for the structural analysis. This quench scheme corresponds to a cooling rate of $\approx$ 3 K/ps and the total simulation time was about 3 ns. The atomic

trajectories were collected every 50 steps during the last 40 ps of the final NVE run and the structural data were averaged over these 800 configurations. It is noted that for the calculation of the velocity auto-correlation functions the trajectories were saved every timestep (40000 configurations) to obtain sufficient data for the short-time dynamical behaviour of the alkaline-earth cations and, hence, determine the vibrational density of states of the simulated glasses.

The ionic diffusion of the alkaline-earth ions was analysed in the temperature range of 1000-1600 K. For every chemical composition, the configuration obtained from the melt-and-quench was reheated from 300 K to a specific temperature within the above range and equilibrated for 200 ps using the NPT ensemble so as to relax internal stresses. The Berendsen barostat and thermostat with relaxation constants 0.4 ps were used, and the timestep of the MD simulations was 2 fs. The NPT run was followed by a 2 ns production run using the NVT ensemble with the Nosé-Hoover thermostat. The atomic trajectories were stored every 50 steps (0.1 ps) and these were used to determine the diffusivity of the alkaline-earth ions within the simulated glasses. The MSD of the alkaline-earth cations was calculated through the equation 2.67 and the self-diffusion coefficients were obtained through the Einstein relation (see equation 2.68). Based on the diffusion coefficient at each temperature, the activation energy barriers for diffusion were extracted from an Arrhenius type plot by using the equation 2.69.

5.3 Results of calculations & Discussion

5.3.1 Short-range order

The local atomic structure of the alkaline-earth ions was scrutinised in order to understand how the type of the cation affects its arrangement within the glass network. It is noted that the three alkaline-earth species (Ca, Sr and Ba) act as network modifiers: they break the Si−O bonds and, thus, interrupt the continuous random silicate network. The local environment around the alkaline-earth ions was investigated in the glass structures in which Na is the alkali component, through the pairwise radial distribution functions, g(r), shown in figure 5.1. The first peak of the g(r) gives information about the first coordination shell of the alkaline-earth cations in the simulated glasses. The average oxygen bond lengths for the three alkaline-earth modifiers are Ca−O = 2.32 Å, Sr−O = 2.64 Å and Ba−O = 2.83 Å, as highlighted in figure 5.1. Reverse Monte Carlo modelling in Na/Ca and Na/Sr silicate glasses with the same molar composition shows similar results.[274] In that study, the Ca−O and Sr−O distances were found to be 2.25 and 2.6 Å respectively, in very good agreement with the calculations presented in this thesis.

From the cation−cation g(r), shown in figure 5.2, the Ca−Ca, Sr−Sr and Ba−Ba nearest neighbour distances are determined as 3.44, 3.78 and 3.99 Å respectively. The study of the local atomic structure for the three alkaline-earth ions in the simulated glass structures reveals a clear systematic change in the cation−oxygen and cation−cation

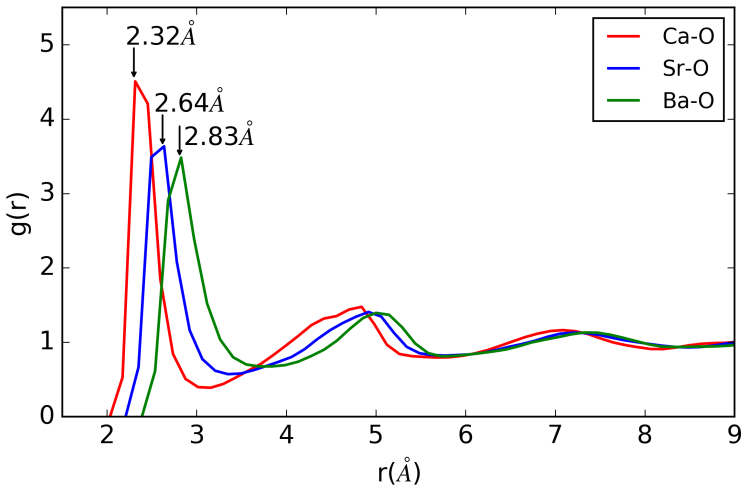

Figure 5.1: Pairwise radial distribution functions of the M−O distances for the three alkaline-earth ions (M = Ca, Sr and B) in the $Na_2O-2MO-4SiO_2$ compositions. The average oxygen bond length elongates as the size of the alkaline-earth cation increases in the simulated glass structure.

distances in the first coordination shell as a function of the ionic size of the alkaline-earth cation, highlighting a correlation with the type of the alkaline-earth ion.

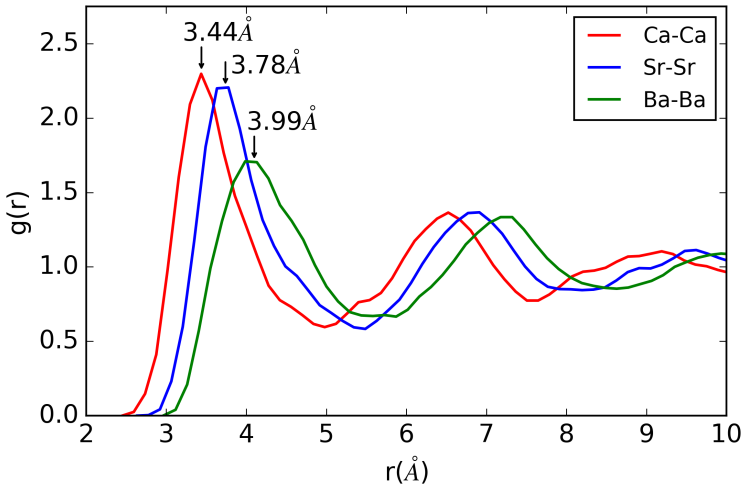

Figure 5.2: Pairwise radial distribution functions of the M−M distances for the three alkaline-earth ions (M = Ca, Sr and B) in the $Na_2O-2MO-4SiO_2$ glasses. The cation−cation interatomic distance becomes longer as the size of the alkaline-earth ion increases in the simulated composition.

The oxygen ions, based on the connection with the Si network former and the alkali and alkaline-earth network modifiers, can be separated in three different types. The O ions bonded to two Si, i.e., Si−O−Si, were labelled as bridging oxygens, BO, those bonded to only one Si and one of the network modifiers, i.e., Si−O−Li/Na/K/Ca/Sr/Ba structural motifs, were considered as non-bridging oxygens, NBO, and those bonded to no Si but only to alkali and/or alkaline-earth cations were regarded as free oxygens, FO.

Representative examples of each type are shown in figure 5.3.

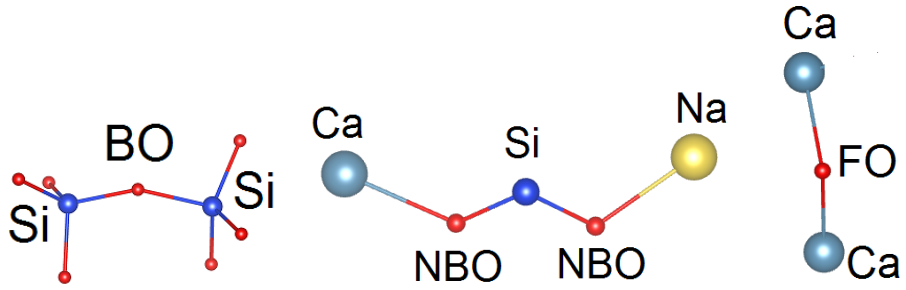

Figure 5.3: The three types of oxygen bonding in the simulated glass structures. Bridging oxygen: bonded to two Si atoms, non-bridging oxygen: bonded to one Si and one of the network modifiers and free oxygen: bonded to two alkali and/or alkaline-earth cations.

The coordination analysis of the oxygen ions in the Na-containing glass structures, shown in figure 5.4, reports that the percentage of the NBO is $\approx 54\%$, of the BO is $\approx 46\%$ and of the FO is $\approx 0.3\%$ in every simulated glass structure. The concentration of the NBO was found to be very high in the glass models, mainly due to the high concentration of the modifier cations, both alkali and alkaline-earth species, in the compositions. The presence of the cation modifiers cause these terminations in the continuous silicate network, which form diffusion pathways for the alkali and alkaline-earth ions within the glass network. It is noted that the percentage of the NBO, BO and FO was almost the same in every simulated glass structure, which indicates that the bonding of the O ions with the other species in the structure is unaffected by the size of the alkaline-earth modifier, demonstrating no correlation with the type of the alkaline-earth ion.

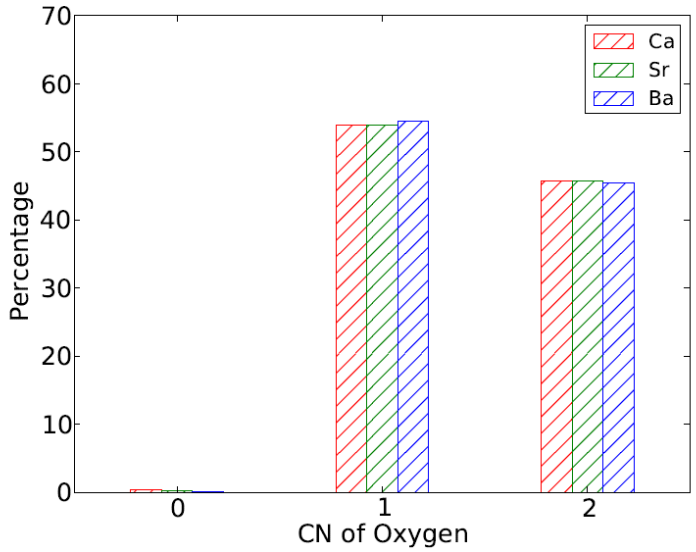

Figure 5.4: Coordination analysis of the oxygen atoms in the Na-containing simulated glasses. The type of bonding of the O atoms with the other species within the glass models remains the same upon the presence of different alkaline-earth cation.

The average oxygen coordination numbers around the alkaline-earth ions, calculated from the integral of the first peak of the cation−oxygen g(r) in figure 5.1, were found to be 6.2, 6.5 and 6.8 for Ca, Sr and Ba respectively. It is observed that they have similar values and hence the alkaline-earth ions are 6 - 7-fold coordinated, by 4.5 - 5.0 to NBO and 1.5 - 2.0 to BO. However, further analysis of the coordination environment of the alkaline-earth ions results in distributions of the coordination numbers which range from 4 to 9 for each cation and they are shown in figure 5.5 for the alkaline-earth cations in the Na-containing glass models. Ca shows a strong preference for 6-fold coordination having a well-defined peak and a narrow distribution, while Sr and Ba, on the contrary, have broader distributions. The different behaviour of the cations suggests that the first coordination shell of the Ca ions is tightly bound, with a preference for the octahedral geometry, whereas Sr and Ba are quite flexible in their coordination environment and both of them show a similar tendency to adopt 7-fold coordinated environment. It is also noted that amongst the different alkaline-earth ions, Ba has the highest proportion of 8-fold oxygen coordination. The bigger cations are able to pack more anions around them which possibly explains the larger coordination number, and thus demonstrates a correlation between the coordination number and the type of the alkaline-earth ion.

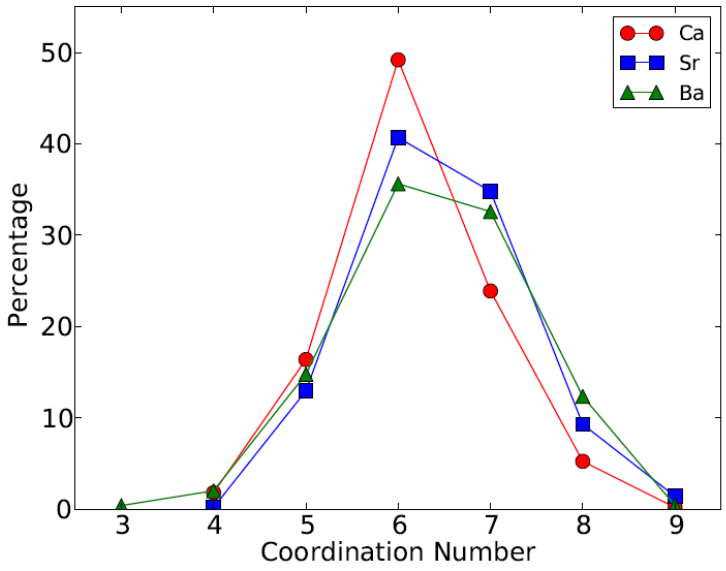

Figure 5.5: Distributions of the oxygen coordination numbers for the three alkaline-earth ions in the $Na_2O-2MO-4SiO_2$ simulated glasses. Ca ions are 6-fold coordinated to oxygen atoms, while Sr and Ba cations show higher flexibility and a similar tendency to 7-fold coordination.

The average oxygen coordination number of Ca in sodium calcium silicate glasses have been reported by previous modelling studies to be 5.8 - 6.2,[232] in very good agreement with the calculated value in this thesis. The coordination numbers of both Sr and Ba in silicate glasses are in the range of 6 - 8. These values are consistent with the oxygen coordination number distributions for Sr and Ba reported in figure 5.5.

The bond angle distribution, g(θ), can provide further information about the structure of the coordination shell of the alkaline-earth ions. Figure 5.6 illustrates the O−M−O (oxygen−alkaline-earth−oxygen) g(θ) functions for Ca, Sr and Ba in the simulated compositions with the same (Na) alkali content. For every cation, the distribution extends from 40° to 180° and there are two main peaks, the first at about 50° - 60° and the second at about 75° - 85°. The exact values of the two peaks in the O−M−O g(θ) for each alkaline-earth cation are reported in Table 5.2. The strongest peak is due to the bonding between the alkaline-earth ions and two non-bridging oxygen atoms belonging to different chains of tetrahedra in the glass network, while the weaker, first, peak originates from the linkage of the cations to two bridging oxygen atoms or one bridging and one non-bridging oxygen belonging to the same tetrahedron.[199,256,262]

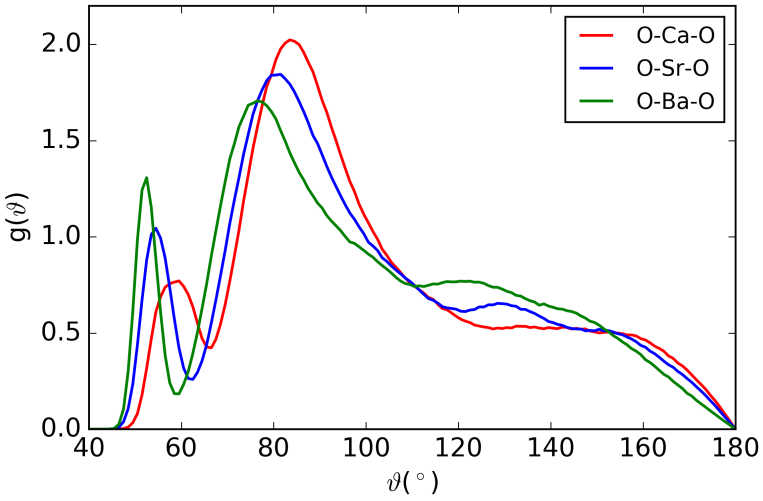

Figure 5.6: O−M−O bond angle distributions of the three alkaline-earth ions (M = Ca, Sr and Ba) in $Na_2O{-}2MO{-}4SiO_2$ compositions. For every cation the BAD exhibits two peaks and their positions are correlated with the type of the alkaline-earth ion in the simulated glass structure.

Table 5.2: Positions of the two peaks in the bond angle distributions of the three alkaline-earth cations in the $Na_2O{-}2MO{-}4SiO_2$ simulated glasses.

O−M−O	First peak (°)	Second peak (°)
O−Ca−O	59.5	83.5
O−Sr−O	54.5	81.5
O−Ba−O	52.5	76.5

As the size of the alkaline-earth cation increases, in the sequence Ca < Sr < Ba, the two peaks in the g(θ) move to lower values and the intensity of the first peak becomes stronger than that of the second peak. This indicates that the Ca distribution is dominated by the NBO−Ca−NBO contribution and only very few Ca cations were found linking to oxygen atoms belonging to the same SiO_4 tetrahedron. The connection

of the cation with the oxygen species changes as the size of the alkaline-earth ion becomes larger. The Ba cation seems to prefer to connect with two bridging oxygen ions or one bridging and one non-bridging oxygen of the same tetrahedron and its coordination environment shows higher flexibility. The analysis of the bond angle distributions of the three cations shows a dependence on the type of the alkaline-earth ion.

From previous classical MD simulations in sodium calcium silicate glasses containing 70-75 mol% SiO_2[232] and calculations in 45S5 bio-glasses,[262] as well as from Car-Parrinello MD simulations in multicomponent silicate glasses,[256] the O−Ca−O bond angle distribution features two peaks at about 60° and 90°, while the corresponding values from the simulations reported in this thesis are 59.5° and 83.5° respectively.

5.3.2 Medium-range order

The effect of the type of the alkaline-earth cation on the medium-range order was characterised through the ring size distributions, which were determined for the Na-based silica glasses containing Ca, Sr and Ba and they are shown in figure 5.7. The ring size distributions reveal that in every simulated structure the 5-member ring is dominant, while rings with 4 to 8 network formers are also quite frequent and there are some larger rings with up to 15 Si members. It is noted that the weight to 4-member rings in the Ca-glass is slightly larger than that in Sr-glass, while the opposite was found for the 5-fold rings. Overall, the combined weight of the 4-, 5-, and 6-fold rings is approximately equal in the compositions containing Ca and Sr. For comparison, the weights of the 5-, 6-, and 7-fold rings in Ba-containing model are noticeably smaller than those in Ca- and Sr-containing glasses, pointing to a weak dependence of the ring size distribution on the size of the alkaline-earth ions. Consequently, the medium-range order does not change significantly upon the different type of the alkaline-earth ions, as a 5-fold ring is the most frequent in each case, where also a broad ring size distribution and large rings were observed.

The results presented in this thesis are consistent with previous modelling studies in sodium calcium silicate glasses with 70-75 mol% SiO_2,[198,232,273] where the medium-range order of these structures is unaffected by the molar composition of the Na and Ca oxides. Moreover, a specific structure from these studies with composition $15Na_2O{-}10CaO{-}75SiO_2$ shows a tendency to 5-fold rings, which is in excellent agreement with the calculated value from the ring size distribution of the equivalent glass structure ($Na_2O{-}2CaO{-}75SiO_2$) simulated in this thesis. It is also noted that the existence of large rings is consistent with the high concentration of NBO ($\approx 54\%$ as calculated above) in the simulated glasses, which disrupt the continuous −Si−O−Si− network and, thus, make the number of available rings smaller and their size larger.[280] Similar results in sodium aluminosilicate glasses[201] and in magnesium-doped sodium calcium silicate glasses[199] have been reported in previous simulation studies.

Polyhedral connectivity between SiO_4 tetrahedra is another way to characterise medium-range order in the glass configurations. All the Si atoms were 100% 4-coordinated

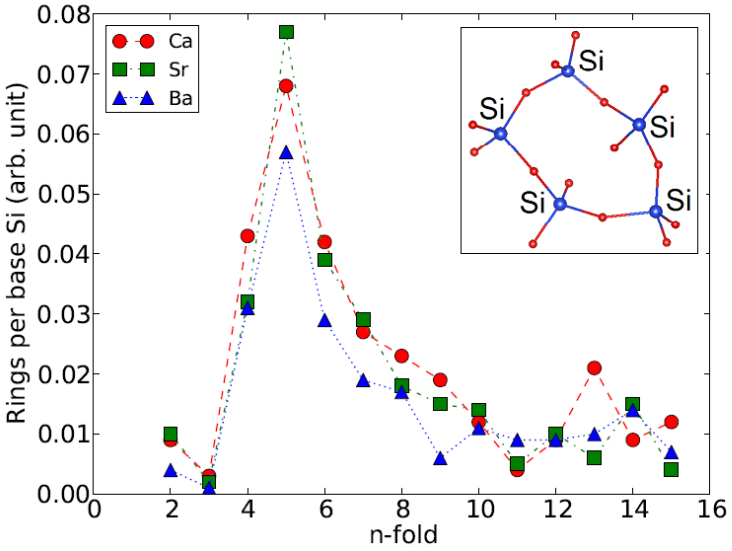

Figure 5.7: Ring size distributions in the $Na_2O{-}2MO{-}4SiO_2$ simulated compositions for M = Ca, Sr and Ba. The lines are included to guide to the eye. Inset: Atomistic structure of a 5-Si member ring, which is the prevailing ring formation within the glass structures.

by O atoms in their first coordination shell and the connections between SiO_4 and SiO_4 tetrahedron were found to be all through corner sharing in the simulated glasses. No edge sharing was observed and the connection is totally independent from the glass molar composition which means that the type of the alkaline-earth ion does not affect the connection of the tetrahedra. Figure 5.8 illustrates the corner sharing connection between the SiO_4 tetrahedra and also how the alkali and alkaline-earth cations are distributed among these tetrahedra.

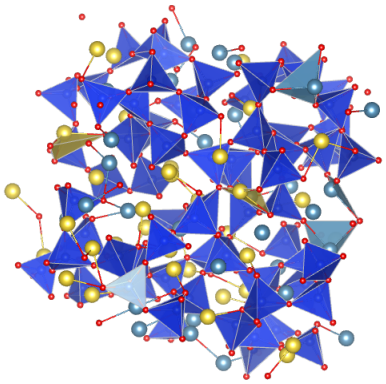

Figure 5.8: Formation of SiO_4 tetrahedra in the $Na_2O{-}2CaO{-}4SiO_2$ simulated glass, corner sharing connections between the different tetrahedra and distribution of the alkali and alkaline-earth cations within the glass network. Blue ball is Si, red ball is O, yellow ball is Na and light blue ball is Ca.

5.3.3 Short-time dynamics and vibrational properties

The partial velocity auto-correlation functions for the $Na_2O{-}2CaO{-}4SiO_2$ glass structure at 300 K are shown in figure 5.9(a). The minimum in the VACF corresponds to the average time needed for the velocity of the ions to be reversed.[255] It can be seen that for Si and O reversals of the velocity are taking place at $\approx$ 0.02 ps, while the oscillations of the VACFs are fast and they are almost in phase during the whole time period, which suggests that the two atoms are strongly correlated, as a result of the rigid intra-tetrahedral vibrations.[207,255] For the alkali and alkaline-earth cations the VACFs reveal only one deep, broad, minimum, which indicates that the relevant reversal of their atomic velocities is happening later in time, and specifically at 0.1 ps and 0.08 ps for Na and Ca respectively.

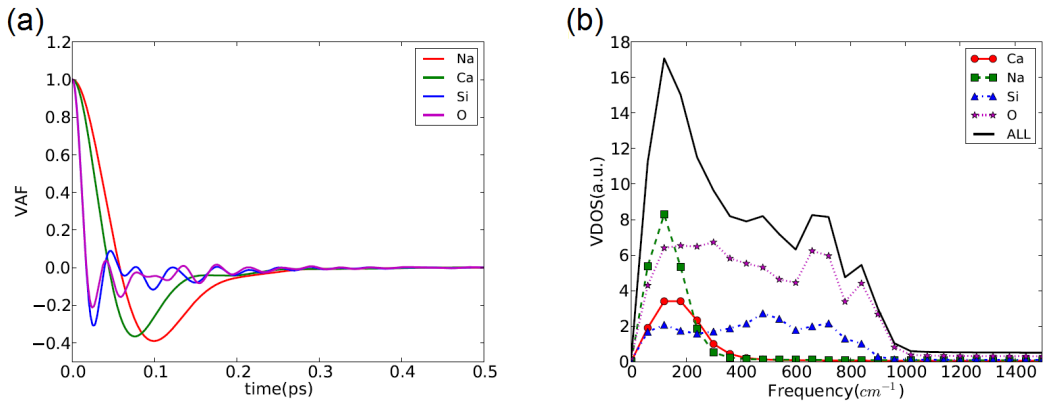

Figure 5.9: (a) Velocity auto-correlation functions of the individual species and (b) Partial and total vibrational density of states in the $Na_2O{-}2CaO{-}4SiO_2$ simulated glass at 300 K. The vibrational spectrum of the glass is calculated from the Fourier transform of the corresponding VACFs.

The vibrational spectrum of the simulated glass can be calculated from the Fourier transform of the VACFs, through the equation 2.66, and hence the partial and total vibrational density of states of this composition are shown in figure 5.9(b). The strongest peak of the spectrum is located at the low frequency end, approximately at 100 cm^{-1}, and all the different species that constitute this glass configuration contribute to this peak. The two peaks located in higher frequencies are mainly due to Si and O contributions. The peak at $\approx$ 850 cm^{-1} can be related to Si$-$O bond stretching, while the broad peak between 450 and 750 cm^{-1} can be assigned to the rocking and bending vibrations between the SiO_4 tetrahedra.[207,255] It is noted that the network modifiers, both alkali and alkaline-earth cations, do not show any high frequency characteristics.

The partial velocity auto-correlation functions of the three alkaline-earth ions in the Na-containing glass structures at 300 K are shown in figure 5.10(a). The oscillation of the VACF for all the alkaline-earth ions is slow and each of the distributions have only one deep, broad minimum. However, it can be observed that as the size of the alkaline-earth ion increases the minimum of the function is located later in time and also

gets broader. Hence, the average time between reversals of the velocity of the alkaline-earth ions occurs at 0.08 ps, 0.14 ps and 0.2 ps for Ca, Sr and Ba respectively, and this is consistent with the larger cations needing more time to reverse their direction of motion within the glass network. Consequently, there is a clear correlation between the short-time dynamical behaviour and the type of the alkaline-earth ion.

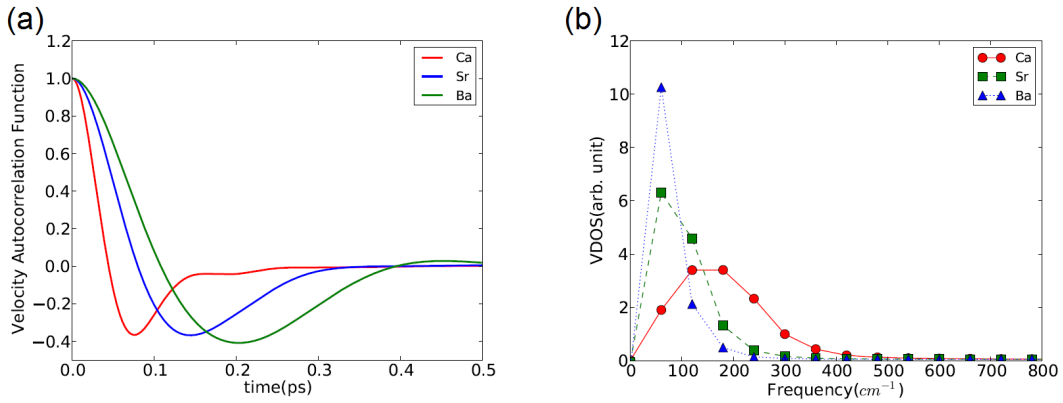

Figure 5.10: (a) Velocity auto-correlation functions and (b) vibrational density of states of the three alkaline-earth ions (Ca, Sr and Ba) in the $Na_2O-2MO-4SiO_2$ compositions at 300 K. The VACF of every cation exhibits only one deep and broad minimum, while the corresponding partial VDOS shows only low frequency peak. The short-time dynamical behaviour and the vibrational properties of the alkaline-earth ions depend on the size of the cation.

Similar behaviour for the network modifying cations has been reported in 45S5 bio-active glasses by Du *et al.*.[207] In addition, 0.08 ps was the value calculated by Tilocca for the average time between reversals of the velocity for Ca ions in sodium calcium bio-active glass,[255] which matches very well with the calculated value in the simulated composition in this thesis.

The partial vibrational density of states of the different alkaline-earth ions for the Na-glass configurations, obtained from the respective velocity auto-correlation functions, are shown in figure 5.10(b). The alkaline-earth cations do not show any high frequency characteristics and each of them exhibit only one low frequency peak, which shifts to lower frequencies and gets narrower as the alkaline-earth ion gets bigger. It is noted that the lower frequencies for larger ions are attributed to their higher mass and weaker bonding with the oxygen atoms, and therefore the vibrational properties are affected by the type of the alkaline-earth ion.

Pedone *et al.*[198] have reported a similar trend in the behaviour of the alkali ions in silicate glasses with 70-75 mol% SiO_2 from molecular dynamics simulations. In addition, experimental studies of far infra-red spectra revealed a band, named "cation mode", which is related to the interaction of the alkali ions with the NBO in the glass structures.[281] In this band the dependence of the frequency on the network former is negligible, but there is a strong correlation between the frequency and the type of the alkali cation, as observed for the alkaline-earth ions from the simulations in this thesis.

5.3.4 Transport properties

The diffusion coefficients, D, of the three alkaline-earth ions were calculated in every glass configuration by measuring the mean square displacement for several temperatures. Figure 5.11 illustrates the MSD of the alkaline-earth ions at 1600 K, plotted as a function of the simulation time, for the Na-containing systems. The non-linear portion of the MSD behaviour, corresponding to the initial ballistic regime, was neglected in each case and, therefore, the first 20 ps of the atomic motion are not considered for the calculation of the ion's diffusion. Nevertheless, the long trajectories stored in the MD simulations (2 ns production run) ensure that the ion will be in a regime that the MSD exhibits a linear relationship with time. Hence, the self-diffusion coefficients of the three cations were quantitatively calculated through the equation 2.68, by fitting the linear region of the MSD of the ions, at temperatures 1000 K, 1200 K, 1400 K and 1600 K, for all the compositions modelled in this thesis.

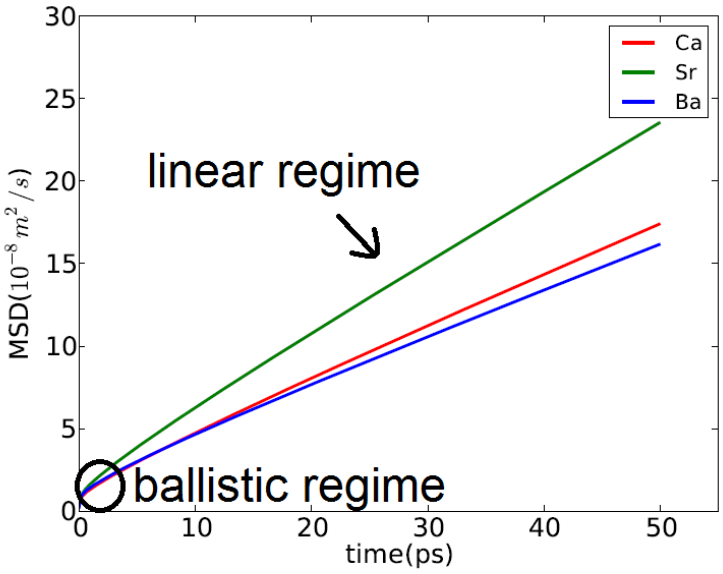

Figure 5.11: Mean square displacement as a function of the simulation time for the three alkaline-earth ions (Ca, Sr and Ba) in $Na_2O-2MO-4SiO_2$ compositions measured at the temperature of 1600 K. The initial ballistic regime of the atomic motion is not considered for the calculation of the diffusion coefficient. The 2 ns trajectory that was sampled during the MD simulations ensures that the MSD of each ion will exhibit a linear relationship with time.

The activation energies for diffusion, E_a, were calculated for each alkaline-earth ion in the simulated glasses from the Arrhenius plots of variation of the diffusion with temperature. Figure 5.12 shows the Arrhenius type behaviour for the temperature dependence of the diffusion coefficients of the three alkaline-earth ions, as calculated in the Na-based glass models. The activation energy barriers for diffusion were calculated for the alkaline-earth ions, in each simulated glass structure, from linear regression of the data, and the results are presented in Table 5.3. The simulated values are also compared with the relevant experimental measurements in the same molar compositions.[279]

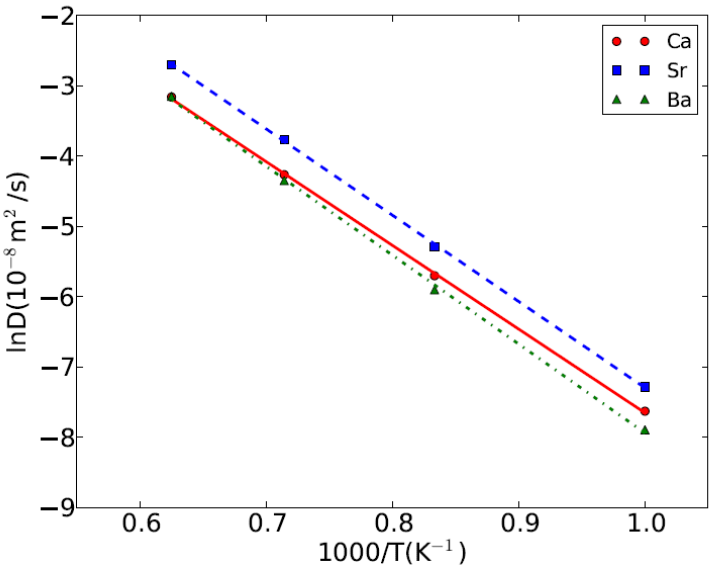

Figure 5.12: Natural logarithm of the calculated self-diffusion coefficients as a function of the reciprocal temperature for the three alkaline-earth ions (Ca, Sr and Ba) in $Na_2O{-}2MO{-}4SiO_2$ glasses. The activation energy barriers for diffusion were determined for all the cations by linear regression of the Arrhenius type plots in every simulated composition.

The diffusion activation energies of the alkaline-earth ions predicted in the simulations presented in this thesis follow the same trend as the experimental data but differ numerically. In general, discrepancies between computational and experimental results have three sources: insufficiently valid models, inaccuracies of simulations as such, and the difference between the measurement process and the computing algorithms aiming to obtain the same property. However, it is noted that the numerical discrepancy with the experimental measurements observed in this thesis is of the same order of magnitude as found in other simulations[198,199,207] and, therefore, the latter two factors are mainly responsible for this difference, and can be attributed to the generic challenges of classical interatomic potentials in simulating temperature activated processes. Indeed, for the force fields employed in classical MD simulations the position of the minimum and the curvature of pairwise potentials near the minimum can be relatively well parametrised, but this is not generally the case for the profile of the potential away from the minimum. Hence, even though classical potentials provide a good description of the glass structural characteristics, they are not necessarily able to perform equally well in modelling transport properties. Unfortunately, this source of errors is difficult to eliminate and, as was mentioned in section 2.8.5, computational studies of ionic diffusion usually focus on the analysis of the trends of the calculated properties in order to extract a qualitative representation of the behaviour of the ions.

In order to validate the accuracy of the calculated results, the diffusion activation energies were compared to computationally derived data, albeit reported for other glass compositions. For example, the calculated diffusion activation energies for Ca^{2+} and

Table 5.3: Calculated diffusion activation energies of the alkaline-earth ions in the simulated $A_2O-2MO-4SiO_2$ glasses and comparison with experimental data for the same compositions. The standard deviation of the calculated E_a is ± 0.0045 eV.

Composition	Alkaline-earth ion M	E_a (eV) simulated[202]	E_a (eV) experimental[279]
$Li_2O-2MO-4SiO_2$	Ca^{2+}	1.05	1.76
	Sr^{2+}	1.11	1.97
	Ba^{2+}	1.17	2.18
$Na_2O-2MO-4SiO_2$	Ca^{2+}	1.03	1.95
	Sr^{2+}	1.06	2.07
	Ba^{2+}	1.09	2.35
$K_2O-2MO-4SiO_2$	Ca^{2+}	1.05	2.12
	Sr^{2+}	0.99	1.89
	Ba^{2+}	0.92	1.49

Sr^{2+} (0.8 eV) in 45S5 bio-active glass, as predicted by Du and Xiang with MD simulations,[207] agree well with the calculated values presented in this thesis. The activation energies for diffusion of the alkali ions were also calculated in the nine simulated compositions, and the results are presented in Table 5.4. In $Na_2O-2CaO-4SiO_2$ glass the diffusion activation energy of the Na^+ was calculated 0.77 eV, which is in very good agreement with previous simulations by Pedone *et al.*, where the activation energy barrier for diffusion of sodium ions was reported 0.74 eV, in sodium calcium silicate glasses with different molar compositions.[198]

Table 5.4: Calculated diffusion activation energies of the alkali ions in the simulated glasses. The standard error in the calculated values of E_a is ± 0.0012 eV.

Composition	Alkali ion (A)	E_a (eV)
$A_2O-2CaO-4SiO_2$	Li^+	0.83
	Na^+	0.77
	K^+	0.85
$A_2O-2SrO-4SiO_2$	Li^+	0.80
	Na^+	0.74
	K^+	0.75
$A_2O-2BaO-4SiO_2$	Li^+	0.82
	Na^+	0.79
	K^+	0.77

Figure 5.13 illustrates the dependence of the diffusion activation energies of the alkaline-earth diffusion on the ratio of the alkaline-earth ions to alkali ions radii. It can be observed that when the sizes of the alkali and alkaline-earth ions are similar, i.e., $\frac{r_M}{r_A} \approx 1$, the diffusion activation energy of the alkaline-earth ion, in a series of compositions with the same alkali content, reaches a minimum value. If the alkaline-

earth ions are smaller than the alkali ions ($\frac{r_M}{r_A} < 1$), as it is the case for the compositions in which A = K, the activation energy for diffusion of the alkaline-earth ions decreases linearly as the $\frac{r_M}{r_A}$ ratio increases. Conversely, in the case of $\frac{r_M}{r_A} > 1$, (i.e., for glasses with A = Li or Na), the diffusion activation energy of the alkaline-earth cations increases linearly as the $\frac{r_M}{r_A}$ ratio increases. It is noted that the diffusion activation energy for the smallest alkaline-earth ion (Ca^{2+}) is almost independent of the radii of the three alkali atoms, whereas the activation energy of the largest alkaline-earth cation (Ba^{2+}) changes by as much as 30%. This suggests that the transport properties of each particular species can be controlled by the appropriate choice of the chemical composition.

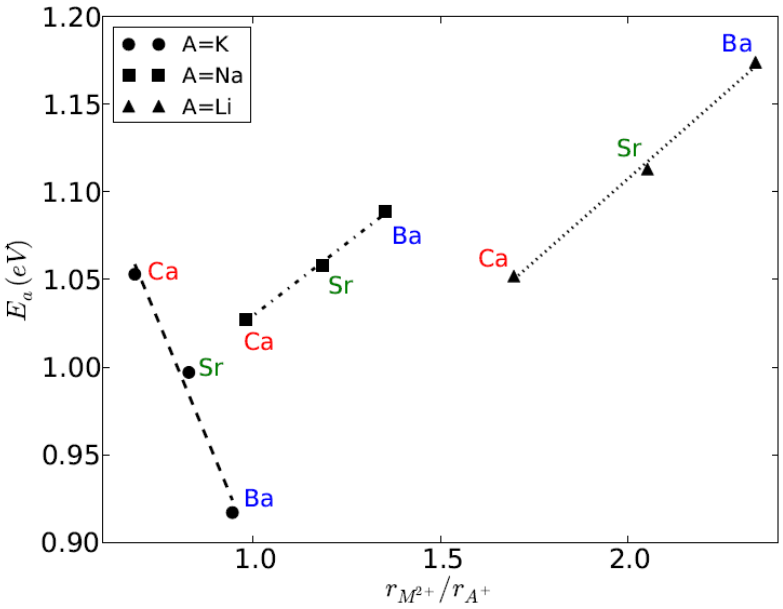

Figure 5.13: Calculated self-diffusion activation energies of the alkaline-earth ions (M = Ca, Sr and Ba) in $A_2O{-}2MO{-}4SiO_2$ glasses with A = Li, Na and K plotted as a function of the alkaline-earth ions to alkali ions radii ratio. The activation energy barrier for diffusion of the alkaline-earth ions decreases linearly as the cations radii ratio approaches unity. For compositions in which $\frac{r_M}{r_A} > 1$ the E_a of the alkaline-earth ions increases linearly as the ratio increases, whereas for glasses in which $\frac{r_M}{r_A} < 1$, the E_a of the alkaline-earth cations decreases linearly as the ratio increases.

This specific behaviour of the diffusion activation energy of the alkaline-earth ions can be well described using linear relationships with the respective $\frac{r_M}{r_A}$ radii ratios for the Li-, Na-, and K-containing simulated glasses:

$$E_a = 0.17 \times \frac{r_M}{r_{Li}} + 0.86$$

$$E_a = 0.19 \times \frac{r_M}{r_{Na}} + 0.73 \tag{5.1}$$

$$E_a = -0.52 \times \frac{r_M}{r_K} + 1.41$$

It is noted that the ionic radius of each of the cations was determined from the values tabulated by Shannon,[282] based on the calculated oxygen coordination numbers of the modifier cations in the simulated glass structures. In particular, the ionic radius of the 4-fold coordinated Li in the structures is 0.59 Å. Na and Ca ions were found to be 6-fold coordinated, which corresponds to the ionic radii of 1.02 and 1.00 Å respectively, while K, Sr and Ba were 7-fold coordinated, giving ionic radii of 1.46, 1.21, 1.38 Å, respectively, for these ions.

A theoretical model proposed by Kirchheim is able to describe this interesting mixed cation effect observed in the diffusion activation energy of the alkaline-earth ions in the simulated compositions.[283] In this model the activation energy for diffusion is related to the electrostatic interaction between the cations and the non-bridging oxygen atoms and the elastic deformation of the glass network induced by the diffusing cations, and two different cases are discussed.

The first case is for radii ratios $\frac{r_M}{r_A} > 1$, in which the elastic interaction between the glass network and the alkaline-earth ions has the most effect on the mobility of the cations.[283] Smaller alkali ions in the structure lead to a reduced mesh size of the silicon/oxygen glass network and, therefore, larger alkaline-earth ions have larger network deformations associated with their jumps. The atomic packing density can help to interpret the influence of the elastic interactions on the mobility of the alkaline-earth ions. The glass atomic packing density, C_g,[284] is defined as the ratio between the minimum theoretical volume occupied by the ions and the corresponding effective volume of the glass:

$$C_g = \rho \frac{\sum_i f_i V_i}{\sum_i f_i M_i} \tag{5.2}$$

For the i^{th} component with formula $A_x B_y$: $V_i = \frac{4}{3\pi} N(x r_A^3 + y r_B^3)$, ρ is the density of the glass structure, N is the Avogadro number, r_A and r_B are the ionic radii, f_i is the molar fraction and M_i is the molar mass. This formula was used for every oxide in the simulated glasses, SiO_2 , A_2O (A = Li, Na and K) and MO (M = Ca, Sr and Ba) in order to estimate the packing density of each glass model. It is noted that for the ionic radii of the atomic species were used the same values as above, and the effective volume of the glass is the one that corresponds to the final equilibrated structure, which is the outcome of the melt-and-quench scheme followed to generate the glasses. Consequently, the relative fractional free volume (FFV) is calculated, knowing the glass packing density, based on the expression: $FFV = 1 - C_g$,[284] and the results for the six simulated glass structures, in which the alkaline-earth ions are larger than the alkali ions, are presented in Table 5.5.

It can be seen that in compositions with the same alkali content, the mesh size of the glass network decreases as the size of the alkaline-earth cation increases, and as a result of this, the diffusion activation energy of the alkaline-earth cation increases and, thus, the mobility of the ion is reduced. It is highlighted that the larger the alkaline-earth ion, the more its mobility is reduced by narrowing the network.

Table 5.5: Fractional free volume of the Li- and Na-containing simulated glass structures, where the alkaline-earth ions are larger than the alkali ions, i.e. $\frac{r_M}{r_A} > 1$.

Composition	Alkaline-earth ion (M)	FFV
$Li_2O-2MO-4SiO_2$	Ca^{2+}	0.56
	Sr^{2+}	0.50
	Ba^{2+}	0.46
$Na_2O-2MO-4SiO_2$	Ca^{2+}	0.53
	Sr^{2+}	0.48
	Ba^{2+}	0.44

The second case is for radii ratios $\frac{r_M}{r_A} < 1$, in which the smaller alkaline-earth ions are able to approach negatively charged non-bridging oxygen atoms more closely than the alkali ions and, therefore, occupy low energy configurations in the glass structures.[283] This is the case in the K-containing simulated glasses, where the relevant average interatomic distances of the cations with the oxygen atoms were determined from the first peaks of the corresponding pairwise radial distribution functions, and the results are shown in Table 5.6.

Table 5.6: Alkaline-earth (M)− and potassium−oxygen interatomic distances in the three K-based simulated compositions, where the alkaline-earth ions are smaller than the alkali ion, i.e. $\frac{r_M}{r_A} < 1$.

Composition	M−O (Å)	K−O (Å)
$K_2O-2CaO-4SiO_2$	2.39	2.68
$K_2O-2SrO-4SiO_2$	2.57	2.72
$K_2O-2BaO-4SiO_2$	2.76	2.77

It can be observed that the three alkaline-earth ions are located closer than the potassium ion to the oxygen atoms in these simulated compositions. The larger the size difference is between the alkaline-earth ion and the potassium ion, the larger the energy difference and, consequently, the larger the diffusion activation energy, which leads to a decreased mobility of the alkaline-earth ion in the glass structure.

5.4 Summary & Conclusions

In this chapter classical MD simulations were carried out for $A_2O-2MO-4SiO_2$ glass compositions in order to investigate the dependence of the structural, vibrational and transport properties on the size of the alkaline-earth ion, along the series Ca < Sr < Ba.

Detailed information about the local atomic structure around the alkaline-earth ions was obtained from the calculations, and a systematic change in the character of the first

coordination shell was observed as the alkaline-earth ion gets larger, demonstrating a strong correlation between the size of the alkaline-earth ions and their short-range ordering. The interatomic distances of the cations with the oxygen atoms, as well as the alkaline-earth−alkaline-earth distances become larger, while also the connection of the alkaline-earth ion with the oxygen species is different within the glass network, as the smallest Ca tends to link with two non-bridging oxygen atoms, whereas the larger Ba seems to prefer linkages with two bridging oxygen atoms. In addition, the Ca ions have a strong preference for octahedral geometry, whereas both Sr and Ba cations are more flexible in their geometrical arrangement within the glass structure, indicating that the alkaline-earth ions are able to set tighter constraints on their local environment as their size decreases. On the contrary, the medium-range order of the simulated glasses is almost unaffected by the size of the alkaline-earth ion as the ring size distribution does not change significantly upon the presence of different alkaline-earth cation in the composition.

Modelling of the short-time dynamical behaviour reveals a connection with the size of the alkaline-earth ion in the simulated glass structures, as the larger alkaline-earth cations require more time to reverse their velocities, and hence the direction of their motion within the glass network. The calculation of the vibrational density of states in the modelled systems illustrates that all the alkaline-earth cations contribute to lower frequencies, but as the size of the alkaline-earth ion increases the vibrational frequencies are shifted to lower values and the frequency distribution gets significantly narrower.

The mobility of the alkaline-earth ions in the simulated glasses was quantified by calculation of their self-diffusion, and the results from the modelling of the ionic diffusion of the cations are in a qualitative agreement with the experimental observations. The classical MD simulations were able to demonstrate the distinct correlation between the diffusion activation energy and the cations radii ratio and validate the higher mobility of the alkaline-earth ions in glasses with higher similarity of the cation size between alkali and alkaline-earth ions. In glass compositions in which the alkaline-earth ion is larger than the alkali ion an asymmetric linear increase in the diffusion activation energy was observed. As the size of the alkaline-earth ion increases the packing density of the glass structure increases and, consequently, the glass network gets narrower, which causes an increase to the activation energy for diffusion, and thus the alkaline-earth ion mobility is reduced. In glass compositions in which the alkaline-earth ion is smaller than the alkali ion a linear decrease in the activation energy for diffusion was observed. As the size of the alkaline-earth ion increases the difference in the size of the cations decreases, and the diffusion activation energy decreases, which results in a more mobile alkaline-earth ion in the glass structure.

6 Excited states and luminescence in sodium silicate glass

6.1 Introduction

Sodium silicate glasses of various compositions are an important class of material that form the basis of glasses for many practical applications, and theoretical understanding of their structure and optical properties is important fundamentally, as they are among the most widely used materials in contemporary optics.[41,112,130,285] Photo-luminescence is a particularly useful and sensitive tool for studying the electronic energy states in glasses with short-range order.[114,115] Sodium silicate glasses are known to luminesce under ultraviolet and X-ray irradiation in a wide range of temperatures, and Mackey *et al.* have shown that they exhibit UV luminescence with a maximum at 3.5 eV.[286] Trukhin *et al.*[122] have measured the excitation spectra, the kinetics and the degree of polarisation of luminescence in high-purity sodium silicate glasses under excitation with ultraviolet light with photon energies exceeding 5.5 eV, as shown in figure 6.1. Their study revealed that the luminescence spectrum has a broad asymmetric band with a maximum luminescence energy of 3.4 eV, analogous to the one in Mackey's study, and they concluded that the luminescence is caused by the intrinsic anisotropic structural motif in the glass, labelled L-centre, which is also responsible for the fundamental absorption edge of these glass compositions. This luminescence can be caused also by the decay of unstable colour centres as a result of thermo-stimulated processes,[286] or tunnelling recombination of electron and hole centres.[122,287]

The first model of the energetic structure and electronic processes in sodium silicate glasses was proposed by Mackey *et al.*.[286] The main assumption of this model is that the top of the valence band of the glass is determined by the electron states of non-bridging oxygen atoms, whereas the sodium ion states form the bottom of the conduction band. According to this model, X-ray irradiation produces intrinsic electron and hole colour centres in the defects present in the sample before irradiation, and the subsequent luminescence is caused by the electron recombination with the hole centre. Moreover, this study established that the electron centres can be easily bleached by illuminating the glass with light corresponding to their absorption band (1 - 3 eV), but the hole centres are more stable and cannot be bleached by illuminating in their absorption band. It is

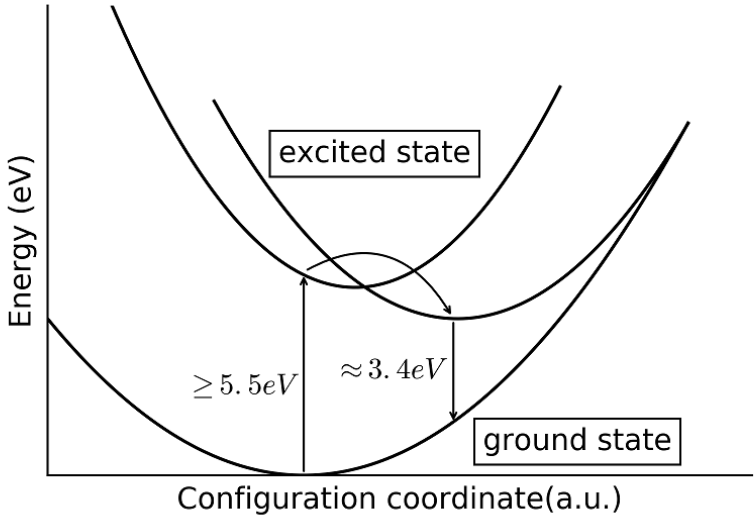

Figure 6.1: A schematic of energy diagram corresponding to the ground and excited state for localised states in sodium silicate glass. The vertical transition from the relaxed ground state to the excited state corresponds to an energy $\geq$ 5.5 eV. After an inter-system crossing and geometry relaxation, the system is in the triplet state, and the luminescence corresponds to the vertical triplet-singlet transition.

also noted that Siegel reported similar results in sodium silicate glass structures.[121]

The simplified structural model of the L-centre, shown in figure 6.2(a), is based on Mackey's proposition[286] that the lowest conduction band of the alkali silicate glasses is due to the alkali s-orbital. The L-centre can be viewed[122,123] as a quasi-molecular complex consisting of an O atom with single coordination to a Si atom and a Na cation located in the close environment, and can be represented as structural fragment $3O{-}Si{-}O^{-}{-}\ Na^{+}$ of the vitreous glass network. In this model, the low energetic transitions are explained in terms of an electron transfer from a non-bridging oxygen atom to a sodium ion. The ground state of the L-centre corresponds to ionic bonding between the NBO and the Na ion and is a singlet state, S_0.[113] The excited L*-centre corresponds to covalent bonding between these atoms and has both singlet S_1 and a lower triplet T_1 state. The light excitation results in the $S_0 \rightarrow S_1$ optical transition, while the photo-luminescence is attributed to the $T_1 \rightarrow S_0$ transition, as highlighted in figure 6.1. These transitions correspond to the electron transport between localised s-orbitals of the Na ion and 2p-states of the NBO atom.

The quasi-molecular nature of the electronic transitions explains the sensitivity of the L-centre properties towards structural disorder, and it can be used to characterise the short-range order of the glass structure.[113] The ionisation of an electron from Na^0 leads to creation of a hole centre, H_1^+ and, hence, the structure of the trapped-hole centre can be represented as $3O{-}Si{-}O^0{-}\ Na^+$, with a strong Na ion displacement with respect to the NBO. The capture of an electron on the L-centre and the Na^0 displacement from the NBO explains the electron centre, E_1^-, creation, and thus, the structure of the

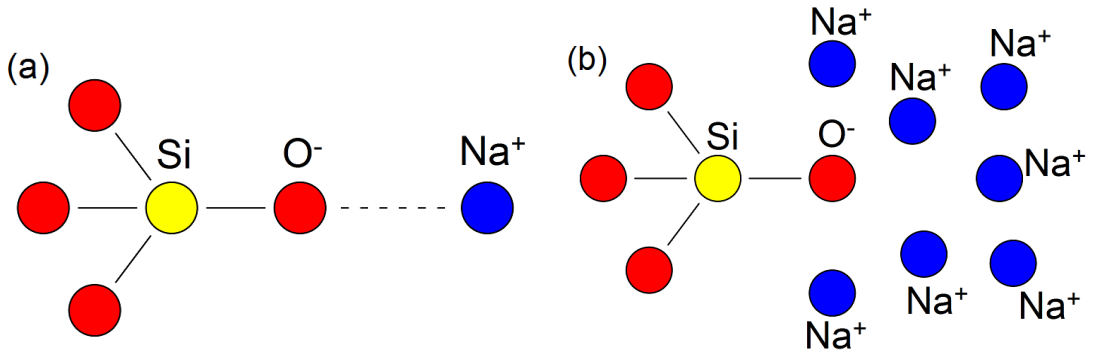

Figure 6.2: (a) The proposed structural model of the L-centre: a quasi-molecular complex which can be represented as a sodium cation in the vicinity of a non-bridging oxygen atom. (b) The extended L-centre model: a cluster of sodium cations located near an ordinary L-centre.

trapped-electron centre can be derived as $3O{-}Si{-}O^{-}{-}\ Na^{0}$. The creation of H_1^+ and E_1^- centres at different distances interprets the rich picture of luminescence kinetics under different pulse durations of excitation light, as well as the formation of colour centres. An electron released thermally or optically from the E_1^- centre recombines with the H_1^+ centre and, hence, the excited state of the centre is restored. In addition, the recombination of E_1^- and H_1^+ centres may occur by the electron tunnelling mechanism.

The L-centre model, in its simplified version, explains qualitatively many effects in sodium silicate glasses, however, it is not able to explain the disappearance of luminescence polarisation at low temperatures.[116,288] This lost-memory effect has been associated to the short-range structure around the L-centre within the glass, and it can be explained in terms of an extended L-centre model, shown in figure 6.2(b) for sodium silicate glass,[113] which assumes that clusters of Na ions are located at positions around the $3O{-}Si{-}O^{-}{-}\ Na^{+}$. Each sodium ion belongs to one or another L-centre. At low temperatures, an electron from an initial Na atom can transfer to a nearest ion and can be stabilised there.

More recent results of the photoluminescence analysis suggest that alkali silicate glasses have at least two types of L-centres, L_1 and L_2, which are strongly dissimilar in their spectral and kinetic characteristics,[113,289,290] and this was explained by the fact that the micro-structure of the glass contains fragments with different degrees of disorder in the environment of the L-centre. In addition, the distribution of the alkali cations in alkali silicate compositions is inhomogeneous within the glass structure, and therefore the observed centres may occupy local regions that are depleted in alkali cations. Stationary exciton-like states appear in optical absorption bands of L-centres during the steady-state optical excitation, and the radiative relaxation of these states is accompanied by the luminescence at 3.0 - 3.5 eV and by electron emission.[113,291]

However, in spite of extensive experimental studies, no atomistic calculations of the L-centres have been performed so far to investigate the proposed qualitative models

and shed light on their atomistic structures. In this thesis, the geometric and electronic structures of localised states in a sodium silicate glass are investigated by means of classical and *ab initio* simulations. The properties of the ground L- and excited L*-centre states, as well as the luminescence energies were calculated, together with the properties of the electron E_1^- and hole H_1^+ centres. The results from the *ab initio* calculations are compared to the experimental data, and they demonstrate the correlation between the local atomic structure of these centres and the short-range order of the simulated glass.

6.2 Computational details

The calculations presented in this chapter make use of both classical force fields and density functional theory. Classical MD simulations were used initially to generate sodium silicate glass models, and DFT calculations were performed afterwards to characterise the electronic structure, model the excited state and calculate the excitation and luminescence energies of these models.

6.2.1 Classical MD simulations

The structures of 20 sodium silicate glasses of the composition $Na_2O{-}3SiO_2$ were generated using classical MD simulations with periodic boundary conditions. The total number of atoms in each periodic cell is 192 with Na=26, Si=51 and O=115. The atoms were placed randomly in a cubic simulation box, with a cell size calculated from the experimental density,[292] with imposed constraints to avoid un-physically close separations. The pairwise potential model developed by Pedone *et al.*[197] (see equation2.62) and described in section 2.7 was employed in the calculations. The DL_POLY classic package[230] was used for the MD simulations and the velocity Verlet algorithm was applied for the integration of the equations of motion with a timestep of 1 fs. The Coulomb interactions were calculated using the Ewald summation method[151] with a precision of 10^{-5}, and the cut off for the short-range interactions was set to 6 Å.

The glass structures were generated using a melt-and-quench approach, and the canonical ensemble was applied to keep the density of the simulated glass close to the experimental value. The Berendsen thermostat with a relaxation constant 0.1 ps, was used to control the temperature. The system was heated up gradually in steps of 100 K with a 60 ps MD run at each temperature. The molten structure was equilibrated at 6000 K using first the NVT and then the NVE ensembles with 400 ps MD run in total, in order to ensure that the structure was well equilibrated at this temperature. The system was subsequently cooled down to 0 K, using a uniform stepwise process, with temperature decrements of -50 K and 60 ps NVT run at each temperature. It is noted that, this quench scheme corresponds to a cooling rate of $\approx$ 0.8 K/ps, while the total simulation time was about 11 ns. The final structure was equilibrated for 200 ps with the NPT ensemble so as to relax internal stresses, and the Berendsen barostat and thermostat were used with relaxation constants 1.0 ps and 0.1 ps respectively. A further

200 ps NVE run was carried out to collect the data and perform the structural analysis. The atomic trajectories were collected every 10 steps during the last 40 ps of the final NVE run, and the structural data were averaged over these 4000 configurations. The accuracy of the model was validated by the comparison of the structure of the simulated glass with the available experimental structural data, while also test simulations were performed in order to investigate the dependence of the structural properties on different periodic cell sizes.

6.2.2 DFT calculations

The output glass structure from the melt-and-quench approach was used as an input configuration, for each glass model, to further optimise the geometry using densty functional theory, as implemented in the CP2K code, and to calculate their electronic structures.[181] In these calculations, all the atomic species were represented using a double$-\zeta$ valence polarised ($DZVP$) Gaussian basis set[231] in conjunction with the GTH pseudopotential,[187] while the plane-wave cut off was set to 1000 Ry. The hybrid functional PBE0_TC_LRC,[178] described in section 2.4.3, was used in all calculations presented in this chapter, and it is noted that the inclusion of the Hartree-Fock exchange provides an accurate calculation of the band gap and also a good description of the localised states of the L-centre in the sodium silicate glass models. The computational cost of the nonlocal functional calculations was reduced by using the auxiliary density matrix method (ADMM),[179] described in section 2.4.3.

The excited state of an L-centre is known to quickly convert into the triplet state.[113] The lowest triplet excited state in the relaxed glass structures was modelled, following the approach described in section 2.8.6, using a ground-state DFT method by placing the system in the triplet state, which promotes an electron from the top of the valence band into the bottom of the conduction band. The geometry of the triplet state was obtained by minimising the total energy of the system with respect to the atomic positions, while the excitation and luminescence energies were calculated using the ΔSCF method, described in section 2.8.6. Hence, the excitation energy corresponds to the difference between the total energies of the glass structure in the ground singlet and the lowest triplet state at the geometry of the ground singlet state, while the luminescence energy is determined from the difference between the total energy of the fully relaxed triplet state and the total energy of the ground singlet state at the triplet state geometry.

The electron E_1^- and hole H_1^+ centres were modelled by injecting an extra electron and hole, respectively, in the relaxed ground state glass structure and minimising the energy with respect to the atomic coordinates. The Broyden-Fletcher-Goldfarb-Shanno (BFGS) optimiser was applied in all the geometry optimisations, performed for the calculations presented in this chapter, to minimise the forces on atoms to within 40 pN (2.5 x 10^{-2}eV Å^{-1}).

6.3 Results of calculations & Discussion

6.3.1 Ground state glass structure

In all 20 simulated glass configurations obtained using classical MD, Si is fully 4-coordinated to oxygen atoms with an average Si−O interatomic distance of 1.62 Å. The typical measurements from the literature for the Si−O bond length are 1.58−1.64 Å for a broad range of silicate glasses.[12,232] A neutron diffraction study[293] in glass compositions with 22 and 31% mol Na_2O concentrations, reported an Si−O interatomic distance of 1.62 Å, in excellent agreement with the calculated value in the, similar, modelled composition in this thesis. The maximum of O−Si−O bond angle distribution is located at 108.5° and it is in good agreement with the value of the perfect tetrahedron (109.5°), which together with the fully 4-coordinated Si atoms indicates the formation of almost perfect SiO_4 tetrahedra in the simulated glass structures. According to the relevant distribution, the Si−O−Si bond angle between the tetrahedron linkages is about 145.5°, while in pure SiO_2 glass this angle is 150°. It is noted that usually the addition of impurities leads to decrease of the Si−O−Si bond angle in the silicate network.

The average Na−O bond length is 2.37 Å, while the average oxygen coordination number around Na ions was found to be 5.8. The Na−Na nearest neighbour distance calculated 3.14 Å and analysis of the local environment around the sodium cations demonstrates that most Na ions have at least 1 or 2 Na ions in nearest neighbours positions, with some having 3 and 4 Na, as shown in figure 6.3. Hence, the Na cations shows a high preference to associate with other Na cations within the glass structure, therefore there is an inhomogeneous distribution of Na ions inside the glass, with Na ion clusters with a range of sizes, characteristic of a micro segregation process. These results are in accordance with the modified continuous random network model, and also agree well with neutron diffraction[293] and EXAFS[3] data as well as with previous modelling studies in sodium silicate glasses,[12,198,232] in which the Na−O and Na−Na bond lengths were calculated 2.30 − 2.38 Å and 3 − 3.3 Å respectively, in compositions similar to the one modelled in this chapter.

Simulations for larger periodic cells, containing up to 12288 atoms, were performed in order to validate the accuracy of the calculated Na−O and Na−Na interatomic distances in the small simulated structure and investigate their dependence on the size of the modelled system. Based on the results shown in Table 6.1, it can be observed that there is a lack of significant size effect on the average interatomic distances, as they seem to be unaffected by increasing the number of atoms in the simulation box.

To study the distribution of L-centre structures and excitation energies 20 periodic glass models of 192 atoms each were used in this chapter. The glass structures obtained using the classical force field, were further optimised using DFT. The results shown in Table 6.2 demonstrate that the changes to the geometric parameters of the glass structure following the geometry relaxation are insignificant, with interatomic distances remaining within 0.02 Å of the original values. This illustrates the quality of interatomic

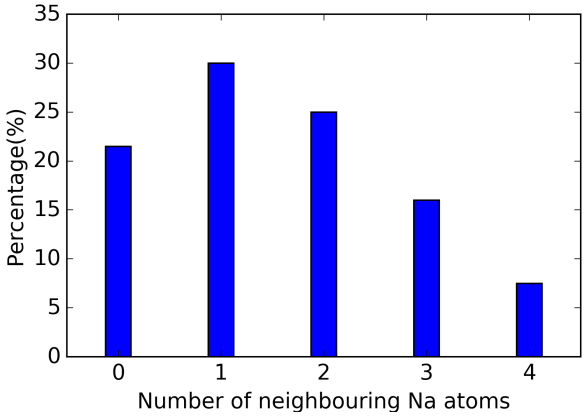

Figure 6.3: Sodium aggregation with other sodium atoms in a glass model of the $Na_2O-3SiO_2$ composition. The sodium coordination number around the sodium atoms was calculated from the integral of the first peak of the Na−Na g(r), and a cutoff 4.7 Å, which corresponds to the local minima of this peak, was used in order to take into account all the Na local environments within their first coordination shell. Hence, a picture of the Na arrangements around other Na atoms within the glass network can be obtained. It can be observed that the Na cations have a heterogeneous distribution within the simulated glass structure.

Table 6.1: Sodium−oxygen and sodium−sodium bond lengths as a function of the size of the glass model. The respective interatomic distances remain almost unaffected across the size ranges, maintaining similar values.

Cell size (number of atoms)	Na−O (Å)	Na−Na (Å)
192	2.37	3.14
648	2.34	3.10
1536	2.32	3.12
4690	2.32	3.02
12288	2.35	3.21

potentials used for the classical MD simulations to generate the amorphous structures. It is noted that the size and number of these glass models were determined by computer resources available for spin-polarised DFT calculations using a nonlocal functional and the obtained statistics should be sufficient for qualitative conclusions.

The electronic structure calculations show an average HOMO-LUMO Kohn-Sham band gap of 5.3 ± 0.4 eV. The total and partial electronic density of states of one of the glass models is shown in figure 6.4. The bottom of the conduction band is due to the sodium ion states, whereas the electron states of non-bridging oxygen atoms determine the top of the valence band. This is in good agreement with Mackey's[286] main assumption that the lowest conduction band of the alkali silicate glasses is due to the alkali s-orbital and the structural model of the L-centre was based on this proposition. The calculated band gap is much lower than that of pure amorphous SiO_2 (9 eV) due to the Na conduction band, and it agrees well with the optical absorption edges of

Table 6.2: Comparative structural analysis between the glass structure obtained from the melt-and-quench approach using the classical force field and the relaxed neutral structure after the DFT optimisation.

Calculated property	Glass from classical MD	DFT relaxed ground state
Cell size (Å)	13.75	13.82
Si−O (Å)	1.62	1.62
CN_{Si-O}	4	4
O−Si−O (°)	108.5	109.5
Si−O−Si (°)	145.5	147.5
Na−O (Å)	2.37	2.36
CN_{Na-O}	5.8	5.5
Na−Na (Å)	3.14	3.12
Si−Na (Å)	3.41	3.36
Si−Si (Å)	3.17	3.15

about 6 eV for sodium silicate glasses reported by Mackey *et al.*[286] and Siegel[121]. In addition, Murray and Ching[294] calculated the band gap at 4.6 eV for $Na_2O{-}2SiO_2$ glass compositions, and it is expected that the band gap of the system would decrease with increasing the Na_2O content.

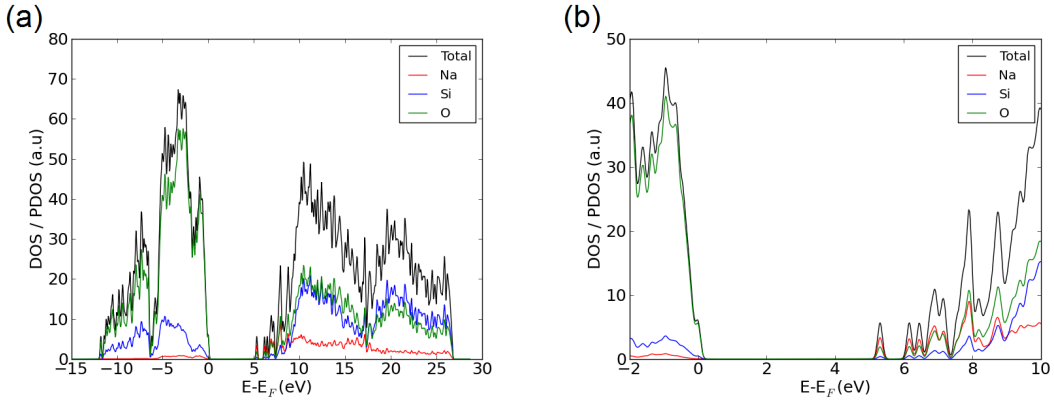

Figure 6.4: (a) Electronic density of states of a $Na_2O{-}3SiO_2$ glass model and contribution of the individual atomic species. (b) The top of the valence band is due to the oxygen 2p states and the bottom of the conduction band is due to the 3s Na ion states.

6.3.2 Excited state & luminescence energy

The excited state of the simulated glass structure was modelled, using ground-state DFT, by calculating the system in a triplet state. An average 5.6 ± 0.3 eV optical excitation energy was obtained from the 20 glass models, which is in very good agreement with the experimental studies,[122,123] where high-purity sodium silicate glasses were excited with ultraviolet light with photon energies exceeding 5.5 eV. The spin density distribution of the triplet excited state of one of the glass models is shown in figure 6.5.

As expected for a disordered system,[112] the excited state is not fully delocalised within the periodic cell but it is rather localised on several (typically 2 or 3) Na ions and 1 to 3 oxygen ions, forming the bottom of the conduction band and the top of the valence band, respectively. It can be observed that, the atomistic structure exposed by this excited state is that of an L-centre. However, in the 20 simulated glass structures studied in this chapter, the L*-centre structure appears to be more complex than the simple $3O{-}Si{-}O^{-}{-}\ Na^{+}$ structure, with several Na^{+} ions and O^{-} ions usually involved.

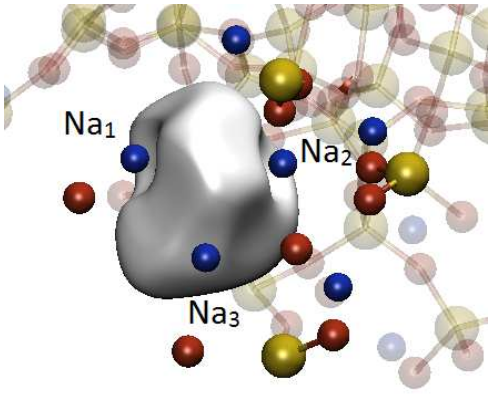

Figure 6.5: Spin density distribution of the triplet excited state before relaxation in one of the $Na_2O{-}3SiO_2$ glass models. The electron shows a preference of localisation between 3 Na cations within the simulated glass structure. The spin density iso-value is 0.002. Yellow ball is Si, blue ball is Na and red ball is O.

Further analysis on the excited states revealed that two types of L-centre structures after vertical excitation, shown in figure 6.6, can be qualitatively distinguished in the modelled systems: type-1 have compact Na ion clusters consisting of 3 ions separated by ≈ 3.6 Å, and type-2, where the separation between Na ions is ≈ 4.8 Å on average. It is noted that due to the relatively small number of Na atoms in the simulated periodic cell, these results may be prone to fluctuations, and thus insufficient for describing all possible structures. Nevertheless, these modelled structures can be treated as representative for the purpose of the study in this chapter.

The relaxed structure of the L*-centre was determined by minimising the total energy of the excited system with respect to the atomic coordinates. The typical spin density distribution of the relaxed triplet excited state is shown in figure 6.7, and it can be seen that it is qualitatively similar to the one after the vertical excitation. However, the character of ionic relaxation differs in different glass structures, as in type-1 structures relatively small (≤ 0.1 Å) displacements of Na and O ions from their original sites were observed, whereas in type-2 structures there are very large displacements, often approaching 1.0 Å. It is noted that these excited states can be considered as relaxed triplet excitons in alkali silicate glasses, as reported by Trukhin.[111]

The luminescence energies were calculated as the energy difference of the ground state (singlet) in the geometry of the relaxed triplet excited state and the relaxed triplet state. Following the two different pictures of the excited state, the calculated lumin-

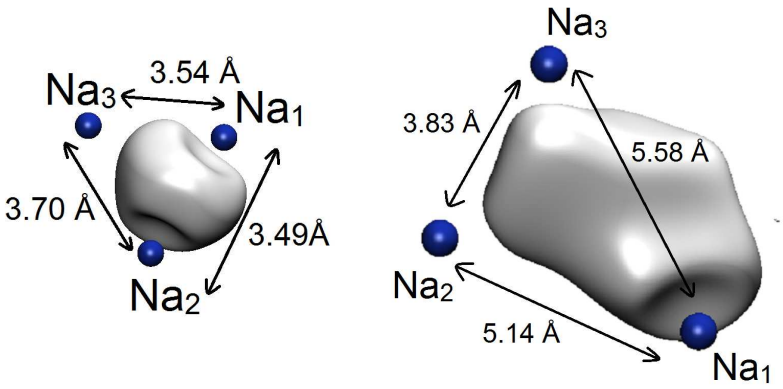

Figure 6.6: Atomistic structure and spin density distribution in the two types of L-centre structures observed in the 20 $Na_2O-3SiO_2$ glass models. Type-1 (left panel) corresponds to a compact cluster of 3 Na ions with average Na−Na interatomic distances of ≈ 3.6 Å, and type-2 (right panel), which corresponds again to a cluster of 3 Na ions but with much larger separations between the cations. The iso-value of spin density is 0.002.

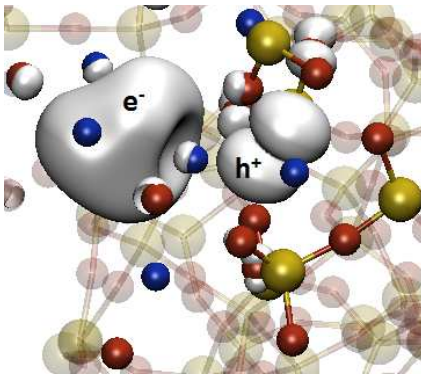

Figure 6.7: Spin density distribution of the relaxed triplet excited state in one of the $Na_2O-3SiO_2$ glass models. The electron and hole components are indicated with e^- and h^+ respectively. The electron is fully localised amongst 3 Na cations and the hole is also well localised in one non-bridging oxygen atom. The iso-value of spin density is equal to 0.002. Yellow ball is Si, blue ball is Na and red ball is O.

escence energies in the 20 sodium silicate glass models show two trends, which are directly related to the two types of the excited state. In the 60% of the glass samples (12 structures), in which L-centres have type-1 structures, the luminescence energy was calculated within the range of 2.7−3.3 eV, whereas in the remaining 8, type-2 L-centres, the calculated luminescence energies were in the range of 1.0−1.7 eV.

The calculated luminescence energies of the first group are in good agreement with the experimental values in sodium silicate glasses, which are known to exhibit a wide luminescence spectrum with the maximum at 3.4 eV.[122,286] In addition, the values of this range agree well with the luminescence spectra of sodium silicate glass with the same molar composition ($Na_2O-3SiO_2$) reported by Zatsepin *et al.*.[290] It is noted that these spectra, as well as those shown in Ref.[111], exhibit red tails extending down to 2.0 eV.

6.3.3 Atomistic relaxation in L*-centres

In order to investigate how the changes in the geometry for the relaxed triplet excited state with respect of the geometry of the relaxed ground state affect the luminescence energies, the atomic displacements for the three component species (Na, O and Si) were calculated in the 20 simulated glass structures. The average calculated displacements of these species, together with the calculated luminescence energies for every glass model, are shown in Table 6.3, and it can be observed that the lower luminescence energies correspond to larger displacements of Na and O atoms for the singlet-triplet transition. For the type-1 L-centre structures, which are associated with the higher values of the luminescence energy, the atomic displacements are on average considerably smaller. The local atomic structure of the type-2 excited state differs, on average, from that of the ground state by ≈ 0.18 Å displacement of the Na cations, whereas the local atomic structure of the type-1 excited state differs from that of the ground state by ≈ 0.06 Å displacement of the Na cations.

Table 6.3: Average displacement, d, between the geometry of the relaxed excited state and the geometry of the relaxed ground state for Na, O and Si atoms in the 20 simulated glass structures and comparison with the calculated luminescence energies, E_L.

Glass	E_L (eV)	d_{Na} (Å)	d_O (Å)	d_{Si} (Å)
1	3.3	0.04	0.04	0.03
2	3.2	0.09	0.05	0.03
3	3.2	0.04	0.04	0.03
4	3.2	0.06	0.04	0.02
5	3.2	0.04	0.03	0.03
6	3.1	0.04	0.05	0.04
7	3.1	0.06	0.08	0.06
8	3.0	0.05	0.03	0.03
9	2.9	0.08	0.04	0.02
10	2.9	0.08	0.06	0.04
11	2.8	0.05	0.06	0.05
12	2.7	0.07	0.07	0.05
13	1.7	0.11	0.06	0.04
14	1.7	0.25	0.12	0.09
15	1.6	0.14	0.08	0.06
16	1.6	0.13	0.07	0.05
17	1.3	0.17	0.06	0.04
18	1.2	0.10	0.07	0.05
19	1.1	0.20	0.13	0.11
20	1.0	0.19	0.10	0.07

Further analysis on the glass sample #14 from Table 6.3, which exhibits the largest average displacement for the Na atoms, was carried out, in order to investigate how the displacements of the atoms within the simulated structure are related to the electron and hole localisation in the excited state. The displacements of all the 192 atoms of

the glass structure between the atomic configurations of the relaxed ground state and the relaxed excited state are illustrated as a function of the distance of each atom from the centre of mass of the L-centre structure in figure 6.8. It can be seen that three Na atoms have displacements of $\approx$ 1.0 Å, which are significantly larger than the average Na displacement (0.25 Å) in this glass structure. The spin density distribution of the triplet excited state is also shown in the inset of the figure 6.8, and the three Na cations that experienced the largest displacements are those that taking part in the localisation of the electron component. The individual displacements of the atomic configuration for the three Na cations are also highlighted in the same figure.

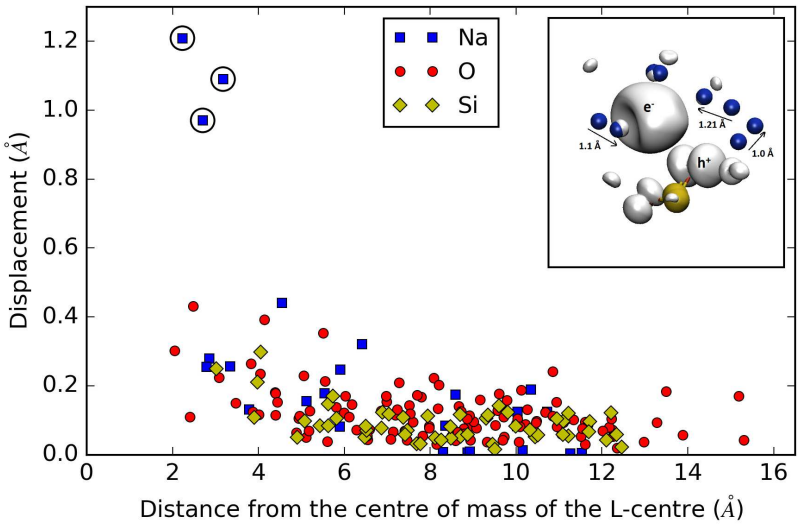

Figure 6.8: Atomic displacements for Na, O and Si atoms between the geometry of the relaxed ground state and the geometry of the relaxed excited state, in a type-2 excited state (glass #14 in Table 6.3), as a function of the distance of each atom from the centre of mass of the L-centre. Encircled are the displacements of the three Na ions most involved in the exciton ($e^- - h^+$) localisation. Inset: Spin density distribution and atomistic structure of the localised excited state. The direction of the arrows corresponds to the direction of the motion from the relaxed ground state to the relaxed excited state. The iso-value of spin density is equal to 0.002. Yellow ball is Si, blue ball is Na and red ball is O.

In order to further examine the topology of the L-centre in this glass model and investigate how the atoms have moved in the relaxed excited state after the transition from the relaxed ground state, the *xy* and *xz* plane of the L-centre structure are illustrated in figure 6.9, combined with the direction of the motion of the atoms. The difference in the interatomic distances between the relaxed ground state and the relaxed excited state for these atoms is noted in Table 6.4.

The distance between Na_1 and Na_2 becomes notably shorter in the relaxed excited state (from 5.46 Å to 3.74 Å) and the electron component gets localised in the close vicinity of these cations. The third sodium ion (Na_3) that is participating in this cluster moves further away from the non-bridging oxygen atom in which the hole component is well localised. It is noted that 3.7 Å is a characteristic interatomic distance between

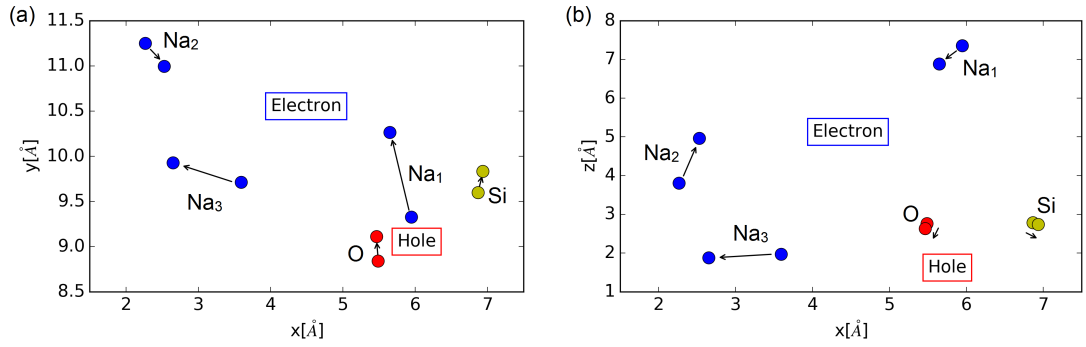

Figure 6.9: Atomic displacements in the type-2 L-centre structure in the glass model #14, and schematic representation of the electron−hole pair localisation in the relaxed excited state. (a) xy and (b) xz plane of the atomic configuration and displacement of all the relevant atoms. The arrows indicate the direction of motion from the relaxed ground state to the relaxed excited state.

Table 6.4: Comparison of the interatomic distances for the atoms forming the triplet exciton in the glass structure #14, in the relaxed ground state and the relaxed excited state.

	Interatomic distance (Å)	
Atom pair	Ground state	Excited state
Na_1−Na_2	5.46	3.74
Na_3−O	2.23	3.02
Si−O	1.57	1.64

the ions, as measured in small Na clusters,[295] which may explain the character of this relaxation. The Na−O bond elongates from 2.23 Å to 3.02 Å, while also the Si−O bond was stretched slightly from 1.57 Å to 1.64 Å.

6.3.4 E_1^- and H_1^+ centres

An extra electron was added to the relaxed ground state and the geometry of each of the modelled systems was then re-optimised. The electronic structure of the 20 glass models exhibits a state located below the conduction band minimum, and the electronic density of states of one of the simulated glasses, in which an electron traps, is shown in figure 6.10. This state corresponds to the highest occupied molecular orbital (HOMO) and it can be seen that it is mostly due to the Na ion states. The average position of this state, from the 20 glass models, is ≈ 1.2 eV below the bottom of the conduction band and ranges from 0.8 to 1.5 eV, indicating a relatively shallow electron trap. These results agree well with Mackey's study,[286] in which they assumed that the electron centres in sodium silicate glass are relatively stable at low temperatures and can be easily bleached by illuminating the glass with 1 - 3 eV light.

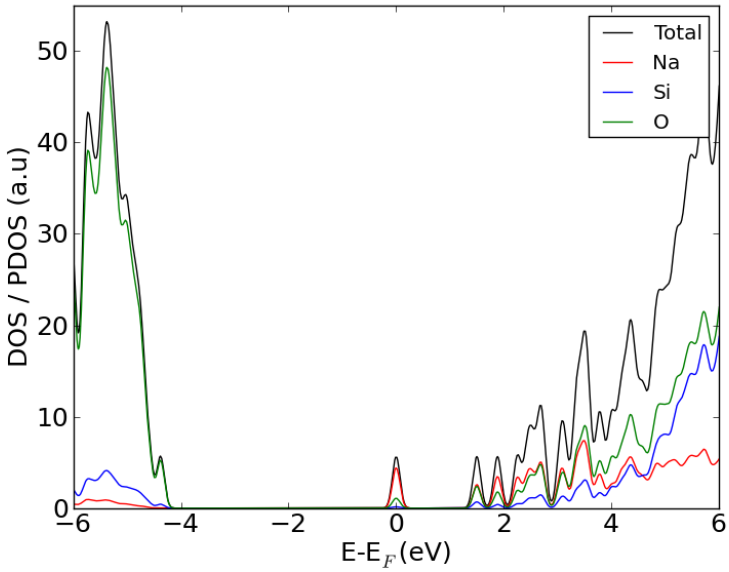

Figure 6.10: Electronic density of states of a $Na_2O{-}3SiO_2$ glass model with a trapped electron. The extra electron occupies, on average, a state at ≈1.2 eV below the bottom of the conduction band. This state is the highest occupied orbital (HOMO) and the Na ions are mainly responsible for this state.

Hence, it is expected the extra electron to be localised on Na cations. The analysis of the spin density distribution, for the 20 simulated glass structures, reveals a concept analogous to the one that was observed above for the localisation of the electron component in an excited L-centre state. The extra electron is localised amongst a cluster of three Na cations within the glass structure, and an example of E_1^- centre formation in one of the glass models is shown in figure 6.11.

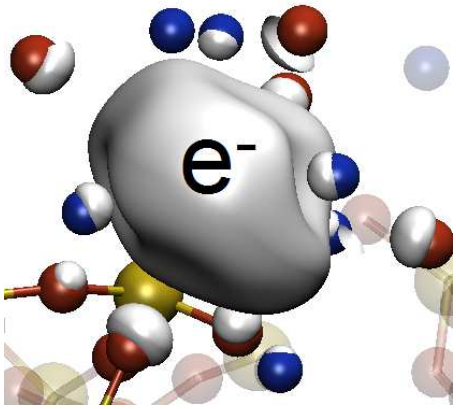

Figure 6.11: Spin density distribution of an electron trap, E_1^-, in one of the $Na_2O{-}3SiO_2$ glass models. The extra electron (e^-) is well localised on a cluster of Na ions within the simulated glass structure. The spin density iso-value is 0.002. Yellow ball is Si, blue ball is Na and red ball is O.

A hole was added to each neutral system and the total energy of the system was minimised with respect to its atomic coordinates. The analysis of the spin density distri-

bution, in the 20 glass models, leads to a similar observation with the hole component localisation in an excited L-centre state. The hole is well localised on a single non-bridging oxygen atom, and an example of H_1^+ centre formation in one of the simulated glass structures is shown in figure 6.12.

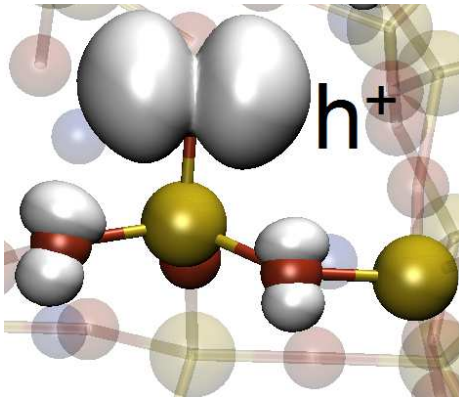

Figure 6.12: Spin density distribution of a hole trap, H_1^+, in one of the $Na_2O{-}3SiO_2$ glass models. The extra hole (h^+) is well localised on a non-bridging oxygen atom. The spin density iso-value is 0.002. Yellow ball is Si and red ball is O.

6.4 Summary & Conclusions

In this chapter 20 models of sodium silicate glasses with composition $Na_2O{-}3SiO_2$ were studied by means of classical and *ab initio* modelling, in order to investigate the atomistic and electronic structures of the localised states in this glass composition and compare them with the existing models from the literature. Detailed information about the local atomic structure around Si and Na was obtained from the calculations, and the results are in very good agreement with previous modelling and experimental studies for the short-range ordering in sodium silicate glasses, providing in that way a good validation for the quality of the simulated glass structures.

The calculated excitation energy is in very good agreement with the experimental values and the excited state can be viewed as a relaxed triplet exciton, in which both electron and hole are well localised on a cluster of Na cations and on a single non-bridging oxygen atom respectively. Two different types of L-centre structures were identified for the excited state after vertical excitation, one consisting of tight clusters of Na ions and another where the Na−Na distances are larger. However, it is noted that due to the small number of Na cations in each glass model, the statistics obtained from the simulated glass structures in this chapter does not allow for a definitive conclusion about whether there is a whole continuum of Na cluster structures in the glass or these are limited to types 1 and 2.

The nature of ionic relaxation differs in the two types of L*-centre states, as relatively small displacements of Na ions were calculated in type-1 structures, whereas very large displacements for the cations were quantified in type-2 structures, strongly

affecting the luminescence energy. The calculated luminescence energies for type-1 L-centre structures are in good agreement with those corresponding to the maximum of the experimental luminescence spectrum, suggesting that such structures prevail in the real glass samples, while other simulated structures give luminescence energies at the red tail of the spectrum, which has been measured experimentally down to around 2 eV.[111,290] It is noted that the calculated results sample only the lowest triplet excitations and the corresponding relaxed exciton states, and that higher excitations could also contribute to the observed luminescence spectrum. Moreover, the transitions with lower energies are likely to be quenched non-radiatively.

The calculations of the individual E_1^- and H_1^+ centres are consistent with the results from the excited states, in terms of the character of the localisation of the electron and hole traps in the glass models, and they are also in agreement with Mackey's model,[286] which suggests that X-ray irradiation creates electron and hole colour centres in the defects present in the glass structure before irradiation. The shallow trapping levels for both electrons and holes lie adjacent to the conduction and valence bands respectively. The electron trapping states are characteristic of the sodium ions, while the hole trapping states are characteristic of the non-bridging oxygen atoms, and it is highlighted that these states are intrinsic to the glass structure.

The calculated results presented in this chapter support the model proposed in previous studies[113,116,122,123,286] that the optical parameters of the L-centre are determined by the interaction of the excited electron with several sodium cations, and shed light on the extended L-centre model, which describes the localised exciton states of electronic excitations in sodium silicate glasses. It was observed that, the electron localisation is mostly restricted to an interstitial cavity and the vicinity of three or four neighbouring sodium ions, and the different kinds of local arrangements of Na cations that can be found in a sodium silicate glass create a spectrum of different localised states. The broad range of the calculated values of luminescence energy reflects the existence of inequivalent local atomic structures for the sodium cations in the glass models, and the calculations presented in this thesis allow the identification of structural motifs responsible for particular luminescence energies.

7 | Synopsis & Outlook

In this thesis, a variety of computational modelling techniques have been used to investigate the structural, dynamical and electronic properties of a number of multicomponent silicate glasses related to several applications, extending from microelectronics to nuclear waste immobilisation.

Mixed alkali borosilicate glasses have long been used for the immobilisation of high level nuclear waste, as they fulfil many criteria required for an effective nuclear waste-form. Atomic scale computer simulations were performed in chapter 3, in order to examine several lithium sodium borosilicate glasses relevant to the experimental compositions from IHI. In the first part of the simulations a suitable computational method to calculate the glass transition temperature in glasses with pre-defined molar compositions was implemented and the results were compared with the experimental values of the IHI structures. The glass transition temperature of the simulated mixed alkali borosilicate glass was calculated at ≈ 600 K. In the second part of the simulations four glass systems were modelled and a detailed structural analysis of the short-range order is presented for each atomic species in the glass structure. In addition, the electronic properties of the glass models were discussed and how these are related to molar composition and the different structural units. A narrowing of the band gap was observed as the concentration of the B_2O_3 is decreased in the glass composition. These investigations of the relationship between the chemical composition and the glass transition temperature and the structural features of the glass will help the industrial collaborator in Japan to interpret their experimental data and proceed with rational design of new glasses.

Experimental studies in nuclear waste glasses show that molybdenum is an element with low solubility in the glass composition and during the vitrification alkali and/or alkaline-earth molybdate crystals are formed, which cause significant disruption to the process of immobilisation of the nuclear waste. Consequently, there is a necessity to design glasses in which formation of these molybdate phases is suppressed in order to maximise the waste disposal efficiency. In chapter 4 the first *ab initio* molecular dynamics simulations in high level nuclear waste glasses were performed. A calcium sodium borosilicate glass and a lithium sodium borosilicate glass were doped with molybdenum, in order to model its local atomic structure within the two different compositions and investigate the effect of ionic and covalent components on the glass structure and the formation of the crystallisation precursors. The coordination environments of

Mo cations and the corresponding bond lengths calculated from the glass models generated in this thesis are in excellent agreement with experimental observations. In the lithium sodium borosilicate glass the Mo cation was found to be in a redox state, and the analysis of the first coordination shell reveals two different types of molybdenum host matrix bonds, demonstrating that the molybdate tetrahedron can be connected with the borosilicate network in a way that inhibits the formation of crystalline molybdates. Such understanding of how the chemical nature and molar composition of the nuclear waste glass affect the local atomic structure of Mo and its solubility within the glass network is invaluable in design of nuclear waste glasses with controlled segregation of the undesirable yellow phases.

This project on the formation of crystalline molybdates in borosilicate glasses could be carried forward in future work by using the two glass structures generated in this work to investigate the migration of Mo cations in the two nuclear glass models. In order to study the dynamical behaviour of the Mo cation, an estimation of the diffusion coefficient in the liquid state, the amorphous state and at the vitrification temperature could be performed, and the three different regimes would give the opportunity to examine how structural differences between the liquid and the corresponding glass obtained upon cooling are related to diffusivity of Mo cations. In addition, simulations of larger systems containing more molybdenum atoms would provide more reliable statistics and a more accurate prediction of the local environments of the Mo cations within the simulated glass structures.

It is worth mentioning that even though these kind of calculations are computationally demanding within the *ab initio* level, the advances in computer architecture and algorithms have meant that atomistic simulations that were challenging twenty years ago are now routine, and there is no reason why this trend should not continue. A development of a reliable classical potential for the B−O and Mo−O interactions, based on the Pedone potential model 2.62, even though it corresponds to a difficult task, could be another route to tackle these kind of computational problems.

Previous experimental studies of the diffusivity of alkaline-earth ions in mixed alkali alkaline-earth silicate glasses of the composition $A_2O{-}2MO{-}4SiO_2$ reveal a distinct correlation between the alkaline-earth cation mobility and the ratio of the alkaline-earth cation radius to that of the alkali cation. It has been observed that the alkaline-earth ions are more mobile when the alkali and alkaline-earth ions in the glass structure are of similar size. In chapter 5 the first atomistic calculations for glasses of this chemical composition were performed, in order to understand the effect of the nature of the cations on the mobility of the alkaline-earth ions within the glass network. The short-range order of the glass structure was found to be influenced by the size of the alkaline-earth cation, whereas the medium-range order was almost unaffected by the type of the cation. In addition, even though all the alkaline-earth cations contribute to lower vibrational frequencies it was observed that there is a shift to smaller frequencies and the vibrational density of states distribution gets narrower as the size of the alkaline-earth cation increases in the glass structure. The experimentally observed

diffusion activation energies of the alkaline-earth ions were qualitatively reproduced in the classical molecular dynamics simulations performed in this thesis. An asymmetrical linear behaviour in the diffusion activation energy with increasing size difference was observed, and the alkaline-earth ions are more mobile in cases that the ratio of the alkaline-earth cation radius to that of the alkali cation is close to unity. Atomistic simulations with empirical methods are able to provide detailed structural information of the simulated glass compositions, and the understanding of how the network modifier cations in complex silicon glasses affect the local atomic structure and mobility of ionic species is critical in design of glasses with controlled atomic transport properties.

This part of the project could be extended in future work by an analysis of the trajectories in the glass models to investigate the mechanism of diffusion of the alkaline-earth ions on the atomic scale, and the identification of the atomic displacements that constitute a step of diffusion. The work presented in this thesis was focused on the type of the cations in the glass structure, therefore, a continuation of this study could possibly be to model the local atomic structure and the mobility of the alkali and alkaline-earth ions in mixed cation silicate glasses with varying the molar composition of the alkali (A_2O) and alkaline-earth (MO) oxide, in order to examine how the structural and transport properties of the glass depend on the relevant concentration of the two oxides in the glass structure.

Previous experimental studies of the ground and electronically excited states of sodium silicate glasses have been interpreted in terms of the so-called L-centre model describing the short-range order in the glass structure. In chapter 6 the first atomistic calculations of the L-centres were performed to investigate the proposed models and shed light on their atomistic structures. *Ab initio* calculations of the electronic and geometric structures of localised states in sodium silicate glass were performed, and the atomistic and electronic structures of the ground L- and excited L*-centre states were calculated, together with the electronic properties of the electron E_1^- and hole H_1^+ centres. The results confirm that the lowest triplet excited states in sodium silicate glass are associated with clusters of sodium ions and non-bridging oxygen atoms. The predicted luminescence energies are correlated with the short-range order of these clusters, and the calculated values are in good agreement with the experimental data. The results obtained in this thesis demonstrate how, combined with the spectroscopic data, theoretical simulations can serve to reveal the local structure of oxide glasses.

The next step on this study could be to investigate the main features of the elementary processes characterising electron and hole trapping sites in lithium, potassium and magnesium silicate glasses, as well as in mixed alkali alkaline-earth silicate glass (for example in sodium calcium silicate glass). The same approach, combining classical molecular dynamics simulations with static density functional theory calculations could be followed to provide an insight into the trapping of the electrons and holes and the mechanism of trapping in such structures. This study would enable the investigation of the behaviour of the different cations, and the examination of the impact of mixing cations in the glass composition.

In a nutshell, atomistic simulations offer the possibility of a complete structural description of a glass and they are able to deepen the interpretative levels obtained from the experiments. In particular, molecular dynamics, which gives an exact description of Boltzmann's statistical mechanics, provides a means to closely mimic the process by which glass is formed in the laboratory, yielding not only the positions and connectivities of every atomic species in the solid state, but also dynamic information, which can be directly compared to experimental measurements. Thus, an understanding of the compositional–glass structure relationships could be used to improve the long-term glass properties in the vast majority of the technological applications.

Bibliography

[1] G. N. Greaves. *J. Non-Cryst. Solids*, 71:203, 1985.

[2] G. S. Henderson. *J. Non-Cryst. Solids*, 183:43, 1995.

[3] C. Mazzara, J. Jupille, A. M. Flank, and P. Lagarde. *J. Phys. B: At., Mol. Opt. Phys.*, 104:3438, 2000.

[4] R. Dupree, D. Holland, and M. G. Mortuza. *J. Non-Cryst. Solids*, 116:148, 1990.

[5] U. Voigt, H. Lammert, H. Eckert, and A. Heuer. *Phys. Rev. B*, 72:64207, 2005.

[6] S. Sen and R. E. Youngman. *J. Non-Cryst. Solids*, 331:100, 2003.

[7] J. Zhao, P. H. Gaskell, M. M. Cluckie, and A. K. Soper. *J. Non-Cryst. Solids*, 232–234:721, 1998.

[8] A. C. Hannon, B. Vessal, and J. M. Parker. *J. Non-Cryst. Solids*, 150:97, 1992.

[9] H. Uhlig, M. J. Hoffmann, H. P. Lamparter, F. Aldiger, R. Bellissent, and S. Steeb. *J. Am. Ceram. Soc.*, 79:2833, 1996.

[10] M. Misawa, D. L. Price, and K. Suzuki. *J. Non-Cryst. Solids*, 37:85, 1980.

[11] W. Smith, G. N. Greaves, and M. J. Gillian. *J. Chem. Phys.*, 103:3091, 1995.

[12] X. Yuan and A. N. Cormack. *J. Non-Cryst. Solids*, 283:69, 2001.

[13] J. Du and A. N. Cormack. *J. Non-Cryst. Solids*, 283:69, 2004.

[14] J. Du and L. R. Corrales. *Phys. Rev. B*, 72:1, 2005.

[15] J. Du and L. R. Corrales. *J. Non-Cryst. Solids*, 352:3255, 2006.

[16] P. Jund and W. R. J. Kob. *Phys. Rev. B*, 64:134303, 2001.

[17] R. D. Banhatti and A. Heuer. *Phys. Chem. Chem. Phys.*, 3:5104, 2001.

[18] A. Heuer, M. Kunow, M. Vogel, and R. D. Banhatti. *Phys. Chem. Chem. Phys.*, 4:3185, 2002.

[19] H. Lammert and A. Heuer. *Phys. Rev. B*, 72:214202, 2005.

[20] W. H. Zachariesen. *J. Am. Chem. Soc.*, 54:3844, 1932.

[21] R. H. Doremus. *Glass Science.* John Wiley & Sons, New York, 1973.

[22] Y. M. Chiang, D. Birnie III, and W. D. Kingery. *Physical Ceramics: Principles for Ceramic Science and Engineering.* John Wiley & Sons, New York, 1997.

[23] H. Rawson. *Properties and Applications of Glass, Glass Science and Technology.* Elsevier, Amsterdam, 1980.

[24] J. C. Boivin and G. Mairesse. *Chem. Mater.*, 10:2870, 1998.

[25] J. C. Boivin. *Int. J. Inorg. Mater.*, 3:1261, 2001.

[26] A. Manthiram and J. Kim. *Chem. Mater.*, 10:2895, 1998.

[27] Wilfried Fischer. *High Energy Batteries With Solid Sodium Ion Conductive Electrolytes*, chapter 20, pages 595–629. World Scientific, 1989.

[28] S. A. Akbar. *Ceram. Eng. Sci. Proc.*, 24:91, 2003.

[29] K. T. Jacob and T. Mathews. *Applications Of Solid Electrolytes In Galvanic Sensors*, chapter 18, pages 513–563. World Scientific, 1989.

[30] S. Chandra. *Superionic Solids, Principles and Applications.* North-Holland, Amsterdam, 1981.

[31] W. Dieterich. *Transport In Ionic Solids: Theoretical Aspects*, chapter 2, pages 17–44. World Scientific, 1989.

[32] C. A. Angell. *Phenomenology Of Fast Ion Conducting Glasses: Facts And Confusions*, chapter 5, pages 89–113. World Scientific, 1989.

[33] A. K. Varshneya. *Fundamentals of Inorganic Glasses.* Academic Press, San Diego, CA, 1994.

[34] M. P. Allen and D. J. Tildesley. *Computer Simulation of Liquids.* Clarendon Press, Oxford, UK, 1989.

[35] S. Balasubramanian and K. J. Rao. *J. Phys. Chem.*, 98:10871, 1994.

[36] J. Habasaki, I. Okada, and Y. Hiwatari. *J. Non-Cryst. Solids*, 183:12, 1995.

[37] A. N.Cormack and Y. Cao. *Molec. Eng.*, 6:183, 1996.

[38] B. Park and A. N. Cormack. *J. Non-Cryst. Solids*, 255:112, 1999.

[39] A. N. Cormack, J. Du, and Z. R. Todd. *Phys. Chem. Chem. Phys.*, 4:3193, 2002.

[40] J. O. Isard. *J. Non-Cryst. Solids*, 1:235, 1969.

[41] D. E. Day. *J. Non-Cryst. Solids*, 21:343, 1976.

[42] M. D. Ingram. *Phys. Chem. Glasses*, 28:215, 1987.

[43] J. C. Lapp and J. E. Shelby. *J. Non-Cryst. Solids*, 95–96:889, 1987.

[44] A. N. Cormack, X. Yuan, and B. Park. *Glass Physics and Chemistry*, 27:28, 2001.

[45] J. E. Shelby and D. E. Day. *J. Am. Ceram. Soc.*, 53:182, 1970.

[46] A. H. Dietzel. *Phys. Chem. Glasses*, 24:172, 1983.

[47] B. Roling and M. D. Ingram. *J. Non-Cryst. Solids*, 265:113, 2000.

[48] M. Solvang, Y. Z. Yue, and S. L. Jensen. *J. Non-Cryst. Solids*, 345–346:782, 2004.

[49] Y. Cao and C. Cramer. *Solid State Ionics*, 176:921, 2005.

[50] M. L. F. Nascimento, E. Nascimento, and S. Watanabe. *Mater. Chem. Phys.*, 96:55, 2006.

[51] R. J. Hand and D. R. Tadjiev. *J. Non-Cryst. Solids*, 356:2417, 2010.

[52] H. W. Guo, X. F. Wang, Y. X. Gong, and D. N. Gao. *J. Non-Cryst. Solids*, 356:2109, 2010.

[53] A. Mohajerani and J. W. Zwanziger. *J. Non-Cryst. Solids*, 358:1474, 2012.

[54] M. L. F. Nascimento and S. Watanabe. *Mat. Chem. Phys.*, 105:308, 2007.

[55] M. D. Ingarm and A. H. J Robertson. *Solid State Ionics*, 94:49, 1997.

[56] M. D. Ingram, C. T. Moynihan, and A. V. Lesikar. *J. Non-Cryst. Solids*, 38–39:371, 1980.

[57] D. Wolf. *J. Phys. Chem. Solids*, 40:757, 1979.

[58] J. N. Mundy. *Solid State Ionics*, 28–30:671, 1988.

[59] D. Ravaine. *J. Non-Cryst. Solids*, 73:287, 1985.

[60] J. A. Bruce, M. D. Ingram, and M. A. MacKenzie. *Solid State Ionics*, 18–19:410, 1986.

[61] S. R. Elliott. *Solid State Ionics*, 27:131, 1988.

[62] S. R. Elliott. *Mat. Sci. Eng. B*, 3:69, 1989.

[63] K. Funke. *Progress in Solid State Chemistry*, 22:111, 1993.

[64] A. Bunde, M. D. Ingram, and P. Maas. *J. Non-Cryst. Solids*, 172–174:1222, 1994.

[65] M. D. Ingram. *Physica A*, 266:390, 1999.

[66] S. Balasubramanian and K. J. Rao. *J. Phys. Chem.*, 97:8835, 1993.

[67] A. Bunde, M. D. Ingram P. Maas, and K. L. Ngai. *J. Non-Cryst. Solids*, 131–133:1109, 1991.

[68] K. J. Rao and S. Kumar. *Current Science*, 86:945, 2003.

[69] P. Maas and R. Peibst. *J. Non-Cryst. Solids*, 352:5178, 2006.

[70] J. Dyre, P. Maas, B. Roling, and D. L. Sidebutton. *Reports on Progress in Physics*, 72:1, 2009.

[71] S. N. Houde-Walter, J. M. Inman, A. J. Dent, and G. N. Greaves. *J. Phys. Chem.*, 97:9330, 1993.

[72] G. N. Greaves and K. L. Ngai. *Phys. Rev. B*, 52:6358, 1995.

[73] B. Gee, M. Janssen, and H. Eckert. *J. Non-Cryst. Solids*, 215:41, 1997.

[74] J. F. Stebbins. *Solid State Ionics*, 112:137, 1998.

[75] E. J. Kamitsos, A. P. Patsis, and G. D. Chryssikos. *J. Non-Cryst. Solids*, 152:246, 1993.

[76] E. J. Kamitsos, Y. D. Yiannopoulos, H. Jain, and W. C. Huang. *Phys. Rev. B*, 54:9775, 1996.

[77] J. Swenson, A. Matic, C. Karlsson, L. Borjesson, C. Meneghini, and W. S. Howell. *Phys. Rev. B*, 63:132202, 2001.

[78] J. F. Ahearne. *Physics Today*, June Issue:24, 1997.

[79] S. M. Rashad and F. H. Hammad. *Appl. Energy*, 65:211, 2000.

[80] C. McCombie. *Physics Today*, page 56, 1997.

[81] D. W. North. *Physics Today*, page 48, 1997.

[82] K. D. Crowley. *Physics Today*, June Issue:32, 1997.

[83] F. L. Toth. *Energy Economics*, 28:1, 2006.

[84] B. G. Parkinson. *Influence of Composition on Structure and Caesium Volatilisation from Glasses for HLW Confinement.* PhD thesis, November 2007.

[85] I. W. Donald, B. L. Metcalfe, and R. N. J. Taylor. *J. Mater. Sci*, 32:5851, 1997.

[86] M. I. Ojovan and W. E. Lee. *An Introduction to Nuclear Waste Immobilisation.* Elsevier, Amsterdam, 2005.

[87] M. I. Ojovan and O. G. Batyukhnova. Glasses for nuclear waste immobilisation. In *WM 07 Conference*, pages 235–283, Tucson AZ, 2007.

[88] J. A. C. Marples. *Glass Technol.*, 29:230, 1988.

[89] B. Luckscheiter and M. Nesovic. *Waste Management*, 16:571, 1996.

[90] D. R. Cousens and S. Myhra. *J. Non-Cryst. Solids*, 54:345, 1983.

[91] Y. Shih. *Mat. Chem. Phys.*, 80:299, 2003.

[92] C. A. Click and T. M. Alam. *J. Non-Cryst. Solids*, 311:294, 2002.

[93] S. Prabakar and K. T. Müeller. *J. Non-Cryst. Solids*, 349:80, 2004.

[94] T. Okura, T. Miyachi, and H. Monma. *J. Eu. Ceram. Soc.*, 2005.

[95] L. L. Hench, D. E. Clark, and J. Campbell. *Nuclear and Chemical Waste Management*, 5:149, 1984.

[96] M. G. Mesko and D. E. Day. *J. Nuc. Mater.*, 273:27, 1999.

[97] J. Sheng, K. Choi, and M. J. Song. *J. Nuc. Mater.*, 297:7, 2001.

[98] M. J. Plodinec. *Glass Technology*, 41:186, 2000.

[99] P. Hrma, J. V. Crum, D. J. Bates, P. R. Bredt, L. R. Greenwood, and H. D. Smith. *J. Nuc. Mater.*, 2005.

[100] S. V. Raman. *J. Mater. Sci.*, 33:1887, 1998.

[101] S. E. Ringwood, S. E. Kesson, N. G. Ware, W. O. Hibberson, and A. Major. *J. Geochem. Exploration*, 141:13, 1979.

[102] S. E. Ringwood, S. E. Kesson, N. G. Ware, W. O. Hibberson, and A. Major. *Nature*, 219:278, 1979.

[103] W. Lutze and R. C. Ewing. *Radioactive Waste Forms for the Future.* North Holland, Amsterdam, 1988.

[104] R. J. Short, R. J. Hand, N. C. Hyatt, and G. J. Möbus. *J. Nucl. Mater.*, 340:179, 2005.

[105] A. Mansour, R. Mesleh, and M. Abaza. *Optics and Lasers in Engineering*, 89:95, 2017. 3DIM-DS 2015: Optical Image Processing in the context of 3D Imaging, Metrology, and Data Security.

[106] A. Akaev. *Soviet Journal of Quantum Electronics*, 12(12):1647, 1982.

[107] M. A. Kitsak and A. I. Kitsak. *Quantum Electronics*, 40(10):914, 2010.

[108] S. T. Murphy, Y. Giret, S. L. Daraszewicz, A. C. Lim, A. L. Shluger, K. Tanimura, and D. M. Duffy. *Phys. Rev. B*, 93:104105, 2016.

[109] E. M. Vogel, S. G. Kosinski, D. M. Krol, J. L. Jackel, S. R. Friberg, M. K. Oliver, and J. D. Powers. *J. Non-Cryst. Solids*, 107(2):244, 1989.

[110] L. B. Glebov. Optical absorption and ionisation of silicate glasses. In G. J. Exarchos, A. H. Guenther, M. R. Kozlowski, K. L. Lewis, and M. J. Soileau, editors, *Laser-Induced Damage in Optical Materials*, pages 343–358. SPIE, 2001.

[111] A. N. Trukhin. Excitons, localized states in silicon dioxide and related crystals and glasses. In D. Griscom, G. Pacchioni, and L. Skuja, editors, *International School of Solid State Physics, 17th course, NATO Science Series. II Mathematics, Physics and Chemistry*, pages 235–283, 2000.

[112] N. F. Mott and E. A. Davis. *Electronic Processes in Non-Crystalline Materials.* Clarendon Press, Oxford, UK, 1971.

[113] A. N. Trukhin. *J. Non-Cryst. Solids*, 189:1, 1995.

[114] L. Skuja. *J. Non-Cryst. Solids*, 239:16, 1998.

[115] D. Ehrt. Photoluminescence in glasses and glass ceramics. In *IOP Conference Series: Materials Science and Engineering 2*, page 012001, 2009.

[116] A. N. Trukhin. *J. Non-Cryst. Solids*, 123:250, 1990.

[117] A. N. Trukhin and P. A. Kullis. *J. Non-Cryst. Solids*, 188:125, 1995.

[118] V. J. Grabovskis, J. J. Dzenis, N. S. Kovaleva, and M. N. Tolstoi. *Fiz. Tverd. Tela*, 32:2953, 1990.

[119] J. R. Zakis. In *15th International Congress On Glass*, page 234, Leningrad, USSR, 1989.

[120] N. F. Mott. *Contemp. Phys.*, 18:225, 1977.

[121] G. H. Siegel. *J. Non-Cryst. Solids*, 13:372, 1973.

[122] A. N. Trukhin, M. N. Tolstoi, L. B. Glebov, and V. L. Savelev. *Phys. Status Solidi (b)*, 99:155, 1980.

[123] A. N. Trukhin, L. E. Intenberg, L. B. Glebov, V. L. Savelev, and U. N. Tolstoi. *Fiz. Tverd. Tela*, 27:3101, 1985.

[124] J. E. Shelby. *Introduction to Glass Science and Technology.* The Royal Society of Chemistry,, Cambridge, UK, 2005.

[125] M. S. F. da Rocha, W. M. Pontuschka, and A. R. Blake. *J. Non-Cryst. Solids*, 321:29, 2003.

[126] G. Brown. *J. Mater. Sci.*, 10:1841, 1975.

[127] B. Boizot, G. Petite, D. Ghaleb, N. Pellerin, F. Fayon, B. Reynard, and G. Calas. *Nucl. Instrum. and Meth. B*, 166–167:500, 2000.

[128] D. L. Griscom. *J. Non-Cryst. Solids*, 6:275, 1971.

[129] I. A. Shkrob, B. M. Tadjikov, and A. D. Trifanac. *J. Non-Cryst. Solids*, 262:6, 2000.

[130] D. L. Griscom. *J. Non-Cryst. Solids*, 31:241, 1978.

[131] J. S. Stroud. *J. Chem. Phys.*, 37:836, 1962.

[132] D. L. Griscom. *J. Non-Cryst. Solids*, 64:229, 1984.

[133] R. Cases and D. L. Griscom. *Bol. Soc. Esp. Ceram. Vid.*, 31C:53, 1992.

[134] D. L. Griscom. *J. Non-Cryst. Solids*, 73:51, 1985.

[135] J. W. H. Schreurs. *J. Chem. Phys.*, 47:818, 1967.

[136] J. H. Mackey, J. W. Boss, and M. Kopp. *Phys. Chem. Glasses*, 11:205, 1970.

[137] G. Kordas, B. Camara, and H. J. Oel. *J. Non-Cryst. Solids*, 50:79, 1982.

[138] G. Kordas and H. J. Oel. *Phys. Chem. Glasses*, 23:179, 1982.

[139] G. Kordas. *Phys. Chem. Glasses*, 37:9, 1996.

[140] L. Astrakas, Y. Deligiannakis, G. Mitrikas, and G. Kordas. *J. Chem. Phys.*, 109:8612, 1998.

[141] I. A. Shkrob, B. M. Tadjikov, and A. D. Trifanac. *J. Non-Cryst. Solids*, 262:35, 2000.

[142] W. G. Hoover. *Computational Statistical Mechanics.* Elsevier, Amsterdam, 1991.

[143] D. Frenkel and B. Smit. *Understanding Molecular Simulation.* Academic Press, Elsevier, 1996.

[144] W. Kob and S. Ispas. First-principles simulations of glass-formers, 2016. arXiv:1604.07959v1 [cond-mat.dis-nn].

[145] A. Rahman. *Phys. Rev.*, 136:405, 1964.

[146] G. Ciccotti and W. G. Hoover. *Molecular dynamics simulations of statistical mechanical systems.* North-Holland, Amsterdam, 1986.

[147] G. C. Maitland, M. Rigby, E. B. Smith, and W. A. Wakeham. *Intermolecular forces.* Clarendon Press, Oxford, 1981.

[148] L. Verlet. *Phys. Rev.*, 159:98, 1967.

[149] L. Verlet. *Phys. Rev.*, 165:201, 1967.

[150] W. C. Swope, H. C. Andersen, P.H. Berens, and K. R. Wilson. *J. Chem. Phys.*, 76:637, 1982.

[151] P. P. Ewald. *Ann. Phys.*, 64:253, 1921.

[152] D. C. Rapaport. *The Art of Molecular Dynamics Simulation.* Cambridge University Press, 2004.

[153] S. D. Bond and B. J. Leimkuhler. *Acta Numerica*, 16:1, 2007.

[154] N. Metropolis, A. W. Rosenbluth, M. N. Rosenbluth, A. H. Teller, and E. Teller. *J. Chem. Phys.*, 21:1087, 1953.

[155] H. C. Andersen. *J. Chem. Phys.*, 72:2384, 1980.

[156] H. J. C. Berendsen, J. P. M. Postma, W. F. van Gunsteren, A. DiNola, and J. R. Haak. *J. Chem. Phys.*, 81:3684, 1984.

[157] S. Nosé. *Molecular Physics*, 52:255, 1984.

[158] S. Nosé. *J. Chem. Phys.*, 81:511, 1984.

[159] W. G. Hoover. *Phys. Rev. A*, 31:1695, 1985.

[160] R. M. Martin. *Electronic Structure. Basic Theory and Practical Methods.* Cambridge University Press, 2004.

[161] D. Marx and J. Hutter. *Ab initio molecular dynamics: Basic theory and advanced methods.* Cambridge University Press, 2009.

[162] D. M. Ceperley and B. J. Alder. *Phys. Rev. Lett.*, 45:566, 1980.

[163] P. Hohenberg and W. Kohn. *Phys. Rev.*, 136:B864, 1964.

[164] W. Kohn and L. J. Sham. *Phys. Rev. Lett.*, 140:A1133, 1965.

[165] W. Kohn. *Rev. Mod. Phys.*, 71:1253, 1999.

[166] R. G. Parr and W. Yang. *Density-Functional Theory of Atoms and Molecules.* Oxford University Press, USA, 1994.

[167] K. Burke. *J. Chem. Phys.*, 136:150901, 2012.

[168] R. O. Jones. *Rev. Mod. Phys.*, 87:897, 2015.

[169] N. W. Ashcroft and N. D. Mermin. *Solid State Physics.* Saunders, 1976.

[170] A. D. Becke. *J. Chem. Phys.*, 140:18A301, 2014.

[171] J. P. Perdew, K. Burke, and M. Ernzerhof. *Phys. Rev. Lett.*, 77:3865, 1996.

[172] A. D. Becke. *Phys. Rev. A*, 38:3098, 1988.

[173] C. Lee, W. Yang, and R. G. Parr. *Phys. Rev. B*, 37:785, 1988.

[174] J. P. Perdew and M. Levy. *Phys. Rev. Lett.*, 51:1884, 1983.

[175] J. L. Gavartin and A. L. Shluger. *Rad. Eff. Defects Solids*, 155:311, 2001.

[176] A. D. Becke. *J. Chem. Phys.*, 98:1372, 1992.

[177] A. D. Becke. *J. Chem. Phys.*, 107:8554, 1997.

[178] M. Guidon, J. Hutter, and J. VandeVondele. *J. Chem. Theory Comput.*, 5:3013, 2009.

[179] M. Guidon, J. Hutter, and J. VandeVondele. *J. Chem. Theory Comput.*, 8:2348, 2010.

[180] G. Lippert, J. Hutter, and M. Parrinello. *Mol. Phys.*, 92:477, 1997.

[181] J. VandeVondele, M. Krack, F. Mohamed, M. Parrinello, T. Chassaing, and J. Hutter. *Comp. Phys. Comm.*, 167:103, 2005.

[182] M. C. Payne, M. P. Teter, D. C. Allan, T. A. Arias, and J. D. Joannopoulos. *Rev. Mod. Phys.*, 64:1045, 1992.

[183] J. C. Phillips. *Phys. Rev.*, 112:685, 1958.

[184] J. C. Phillips and L. Kleinman. *Phys. Rev.*, 116:287, 1959.

[185] N. Troullier and J. L. Martins. *Phys. Rev. B*, 43:1993, 1991.

[186] D. R. Hamann, M. Schlüter, and C. Chiang. *Phys. Rev. Lett.*, 43:1494, 1979.

[187] S. Goedecker, M. Teter, and J. Hutter. *Phys. Rev. B*, 54:1703, 1996.

[188] J. VandeVondele and J. Hutter. *J. Chem. Phys.*, 118:4365, 2003.

[189] J. Kolafa. *J. Comp. Chem.*, 25:335, 2004.

[190] G. Martyna, M. L. Klein, and M. E. Tuckerman. *J. Chem. Phys.*, 97:2635, 1992.

[191] G. Bussi, D. Donadio, and M. Parrinello. *J. Chem. Phys.*, 126:014101, 2007.

[192] K. Vollmayr, W. Kob, and K. Binder. *Phys. Rev. B*, 54:22, 1996.

[193] A. Tilocca. *J. Chem. Phys.*, 139:114501, 2013.

[194] A. Tilocca. *Phys. Chem. Chem. Phys.*, 16:3874, 2014.

[195] J. E. Lennard-Jones. *The Proceedings of the Physical Society*, 43:461, 1931.

[196] M. J. D. Rushton. *Simulations of Glass and Ceramic Systems for Nuclear Waste Applications*. PhD thesis, Department of Materials, Imperial College of Science, Technology and Medicine, 2006.

[197] A. Pedone, G. Malavasi, M. C. Menziani, A. N. Cormack, and U. Serge. *J. Phys. Chem. B*, 110:11780, 2006.

[198] A. Pedone, G. Malavasi, A. N. Cormack, U. Serge, and M. C. Menziani. *Theor. Chem. Acc.*, 120:557, 2008.

[199] A. Pedone, G. Malavasi, M. C. Menziani, U. Serge, and A. N. Cormack. *J. Phys. Chem. C*, 112:11034, 2008.

[200] Y. Xiang, J. Du, L. B. Skinner, C. J. Benmore, A. W. Wren, D. J. Boyd, and M. R. Towler. *RSC Advances*, 3:5966, 2013.

[201] Y. Xiang, J. Du, M. M. Smedskjaer, and J. C. Mauro. *J. Chem. Phys.*, 139:044507, 2013.

[202] K. Konstantinou, P. V. Sushko, and D. M. Duffy. *J. Non-Cryst. Solids*, 422:57, 2015.

[203] A. Pedone. *J. Phys. Chem. C*, 113:20773, 2009.

[204] S. Le Roux and P. Jund. *Comp. Mat. Sci.*, 49:70, 2010.

[205] L. Guttman. *J. Non-Cryst. Solids*, 116:145, 1990.

[206] P. H. Poole, P. F. McMillan, and G. H. Wolf. *Rev. Mineral.*, page 563, 1995.

[207] J. Du and Y. Xiang. *J. Non-Cryst. Solids*, 358:1059, 2012.

[208] W. Li and S. H. Garofalini. *Solid State Ionics*, 166:365, 2004.

[209] W. P. Hess, A. G. Joly, K. M. Beck, P. V. Sushko, and A. L. Shluger. *Surf. Sci.*, 564:62, 2004.

[210] W. P. Hess, A. G. Joly, K. M. Beck, M. Henyk, P. V. Sushko, P. E. Trevisanutto, and A. L. Shluger. *J. Phys. Chem. B*, 109:19563, 2005.

[211] D. Munoz-Ramo, P. V. Sushko, and A. L. Shluger. *Phys. Rev. B*, 85:024120, 2012.

[212] R. O. Jones and O. Gunnarsson. *Rev. Mod. Phys.*, 61:689, 1989.

[213] A. Hellman, B. Razaznejad, and B. I. Lundqvist. *J. Chem. Phys.*, 120:4593, 2004.

[214] O. Gunnarsson and B. I. Lundqvist. *Phys. Rev. B*, 13:4274, 1976.

[215] A. Gorling. *Phys. Rev. A*, 59:3359, 1999.

[216] I. L. Pegg and I. Joseph. *Hazardous and Radioactive Waste Treatment Technologies Handbook*. CRC Press, Boca Raton, FL, 2001.

[217] S. Sen, Z. Xu, and J. F. Stebbins. *J. Non-Cryst. Solids*, 226:29, 1998.

[218] L. S. Du, J. R. Allwardt, B. C. Schmidt, and J. F. Stebbins. *J. Non-Cryst. Solids*, 337:196, 2004.

[219] T. J. Kiczenski, L. S. Du, and J. Stebbins. *J. Non-Cryst. Solids*, 351:3571, 2005.

[220] Y. H. Yun and P. J. Bray. *J. Non-Cryst. Solids*, 27:363, 1978.

[221] Y. H. Yun, S. A. Feller, and P. J. Bray. *J. Non-Cryst. Solids*, 33:273, 1979.

[222] S. Z. Xiao. *J. Non-Cryst. Solids*, 45:29, 1981.

[223] W. J. Dell, P. J. Bray, and S. Z. Xiao. *J. Non-Cryst. Solids*, 58:1, 1983.

[224] D. Manara, A. Grandjean, and D. R. Neuville. *J. Non-Cryst. Solids*, 355:2528, 2009.

[225] D. Manara, A. Grandjean, and D. R. Neuville. *Amer. Mineral.*, 94:777, 2009.

[226] J. M. Roderick, D. Holland, A. P. Howes, and C. R. Scales. *J. Non-Cryst. Solids*, 293–295:746, 2001.

[227] T. F. Soules and A. K. Varshneya. *J. Am. Ceram. Soc.*, 64:145, 1981.

[228] J. M. Delaye and D. Ghaleb. *Mater. Sci. Eng. B*, 37:232, 1996.

[229] F. Gou, G. N. Greaves, W. Smith, and R. Winter. *J. Non-Cryst. Solids*, 539:539, 2001.

[230] W. Smith and T. R. Forester. *J. Mol. Graph.*, 14:136, 1996.

[231] J. VandeVondele and J. Hutter. *J. Chem. Phys.*, 127:114105, 2007.

[232] A. N. Cormack and J. Du. *J. Non-Cryst. Solids*, 293-295:283, 2001.

[233] L. Cormier, D. Ghaleb, J. M. Delaye, and G. Calas. *Phys. Rev. B*, 61:14495, 2000.

[234] A. J. Connelly, K. P. Travis, R. J. Hand, N. C. Hyatt, and E. Maddrell. *J. Am. Ceram. Soc.*, 94:151, 2011.

[235] O. Majérus, L. Cormier, G. Calas, and B. Beuneu. *Phy. Rev. B*, 67:024210, 2003.

[236] J. Sarnthein, A. Pasquarello, and R. Car. *Phys. Rev. B*, 52:12690, 1995.

[237] M. Benoit, S. Ispas, P. Jund, and R. Jullien. *Eur. Phys. J. B*, 13:631, 2000.

[238] A. Tilocca and N. H. de Leeuw. *J. Mater. Chem.*, 16:1950, 2006.

[239] J. Du and L. R. Corrales. *J. Phys. Chem.*, 110:22346, 2006.

[240] L. Pedesseau, S. Ispas, and W. Kob. *Phys. Rev. B*, 91:134202, 2015.

[241] G. H. Siegel. *J. Non-Cryst. Solids*, 13:363, 1974.

[242] T. Uchino, M. Iwasaki, T. Sakka, and Y. Ogata. *J. Phys. Chem.*, 95:5455, 1991.

[243] S. Ispas, M. Benoit, P. Jund, and R. Jullien. *Phys. Rev. B*, 64:214206, 2001.

[244] S. Ohmura and F. Shimojo. *Phys. Rev. B*, 78:224206, 2008.

[245] G. Calas, M. Le Grand, L. Galoisy, and D. Ghaleb. *J. Nucl. Mater.*, 322:15, 2003.

[246] F. Farges, R. Siewert, G. E. Brown, A. Guesdon, and G. Morin. *Can. Mineral.*, 44:731, 2006.

[247] D. Caurant, O. Majérus, E. Fadel, A. Quintas, C. Cervais, T. Charpentier, and D. Neuville. *J. Nucl. Mater.*, 396:94, 2010.

[248] A. Paul. *J. Non-Cryst. Solids*, 123:354, 1990.

[249] D. Caurant, O. Majérus, E. Fadel, M. Lenoir, C. Cervais, and O. Pinet. *J. Am. Ceram. Soc.*, 90:774, 2007.

[250] J. Sarnthein, A. Pasquarello, and R. Car. *Phys. Rev. Lett.*, 74:4682, 1995.

[251] R. M. Van Ginhoven, H. Jonsson, and L. R. Corrales. *Phys. Rev. B*, 71:024208, 2005.

[252] S. Ispas, M. Benoit, P. Jund, and R. Jullien. *J. Non-Cryst. Solids*, 307:946, 2002.

[253] D. Donadio, M. Bernasconi, and F. Tassone. *Phys. Rev. B*, 70.

[254] A. Tilocca and N. H. de Leeuw. *J. Phys. Chem. B*, 110:25810, 2006.

[255] A. Tilocca. *Phy. Rev. B*, 76:224202, 2007.

[256] A. Tilocca. *J. Chem. Phys.*, 133:014701, 2010.

[257] J. K. Christie, R. I. Ainsworth, and N. H. de Leeuw. *Biomaterials*, 35:6164, 2014.

[258] K. Trachenko, V. V. Brazhkin, G. Ferlat, M. T. Dove, and E. Artacho. *Phys. Rev. B*, 78:172102, 2008.

[259] F. Michel, L. Cormier, P. Lombard, B. Beuneu, L. Galoisy, and G. Calas. *J. Non-Cryst. Solids*, 379:169, 2013.

[260] J. K. Christie and A. Tilocca. *Adv. Eng. Mater.*, 12:326, 2010.

[261] J. K. Christie, A. Pedone, M. C. Menziani, and A. Tilocca. *J. Phys. Chem. B*, 115:2038, 2011.

[262] Y. Xiang and J. Du. *Chem. Mater.*, 23:2703, 2011.

[263] I. D. Brown and R. D. Shannon. *Acta Crystallogr. A*, A29:266, 1973.

[264] I. D. Brown and D. Altermatt. *Acta Crystallogr. B*, 41:240, 1985.

[265] I. D. Brown and D. Altermatt. *Acta Crystallogr. B*, 41:244, 1985.

[266] L. Galoisy, L. Cormier, S. Rossano, A. Ramos, G. Calas, P. Gaskell, and M. Le Grand. *Mineral. Mag.*, 64:207, 2000.

[267] L. Pauling. *J. Am. Chem. Soc.*, 51:1010, 1929.

[268] B. Camara, W. Lutze, and J. Lux. *Sci. Basis for Nucl. Waste Man.*, 2:93, 1980.

[269] A. Horneber, B. Camara, and W. Lutze. *Sci. Basis for Nucl. Waste Man.*, 5:279, 1982.

[270] R. J. Landry. *J. Chem. Phys.*, 48:1422, 1968.

[271] V. Aubin-Chevaldonnet, D. Gourier, D. Caurant, S. Esnouf, T. Charpentier, and J. M. Costantini. *J. Phys. Condens. Matter*, 18:4007, 2006.

[272] K. Konstantinou, P. V. Sushko, and D. M. Duffy. *Phys. Chem. Chem. Phys.*, 18:26125, 2016.

[273] X. Yuan and A. N. Cormack. *Ceram. Trans*, 82:281, 1998.

[274] C. Karlsson, E. Zanghellini, J. Swenson, B. Roling, D. T. Bowron, and L. Borjesson. *Phys. Rev. B*, 72:064206, 2005.

[275] B. Roling and M. D Ingram. *Solid State Ionics*, 105:47, 1998.

[276] F. Natrup, H. Bracht, C. Nartiny, S. Murugavel, and B. Roling. *Phys. Chem. Chem. Phys.*, 4:3225, 2002.

[277] F. Natrup, H. Bracht, S. Murugavel, and B. Roling. *Phys. Chem. Chem. Phys.*, 7:2279, 2005.

[278] M. Grofmeier, F. V. Natrup, and H. Bracht. *Phys. Chem. Chem. Phys.*, 9:5822, 2007.

[279] F. Natrup, M. Grofmeier, and H. Bracht. *Solid State Ionics*, 180:109, 2009.

[280] C. Leonelli, G. Lusvardi, M. Montorsi, M. C. Menziani, L. Menabue, and P. Mustarelli. *J. Phys. Chem. B*, 105:919, 2001.

[281] G. Exarchos and W. M. Jr. Risen. *Solid State Commun.*, 11:755, 1972.

[282] R. D. Shannon. *Acta Crystallogr.*, A32:751, 1976.

[283] R. Kirchheim. *J. Non-Cryst. Solids*, 328:157, 2003.

[284] T. Rouxel. *J. Am. Ceram. Soc.*, 90:3019, 2007.

[285] B. Mysen and P. Richet. *Silicate Glasses and Melts. Properties and Structure.* Elsevier, Amsterdam, 2005.

[286] J. H. Mackey, H. L. Smith, and A. Halperin. *J. Phys. Chem. Solids*, 27:1759, 1966.

[287] A. R. Kangro, M. N. Tolstoi, I. K. Vitol, V. J. Grabovski, and J. E. Kariss. *Fiz. Khim. Stekla*, 4:717, 1978.

[288] A. N. Trukhin, L. B. Glebov, and M. N. Tolstoi. *Sov. Phys. Chem. Glasses*, 14:547, 1988.

[289] A. F. Zatsepin, V. B. Guseva, and D. A. Zatsepin. *Glass Physics and Chemistry*, 34:709, 2008.

[290] D. A. Zatsepin and A. F. Zatsepin. *J. Surf. Investigation, X-ray, Synchrotron and Neutron Techniques*, 8:726, 2014.

[291] V. I Arbuzov, A. F. Zatsepin, V. S. Kortov, M. N. Tolstoi, and V. V. Tyukov. *J. Non-Cryst. Solids*, 134:208, 1991.

[292] J. Du and A. N. Cormack. *J. Non-Cryst. Solids*, 349:66, 2004.

[293] A. C. Wright, A. G. Clare, B. Bachra, R. N. Sinclair, A. C. Hannon, and B. Vessal. *Tans. Am. Crystallog. Asso.*, 27:239, 1991.

[294] R. A. Murray and W. Y. Ching. *J. Non-Cryst. Solids*, 94:144, 1987.

[295] G. Pal, G. Lefkidis, H. C. Schneider, and W. Hubner. *J. Chem. Phys.*, 133:154309, 2010.